

University of Alabama in Huntsville

**LOUIS**

---

Dissertations

UAH Electronic Theses and Dissertations

---

2024

## A computational investigation of firebrand dispersion and deposition in areas with cubic structures

Aditya Prakash Mankame

Follow this and additional works at: <https://louis.uah.edu/uah-dissertations>

---

### Recommended Citation

Mankame, Aditya Prakash, "A computational investigation of firebrand dispersion and deposition in areas with cubic structures" (2024). *Dissertations*. 409.  
<https://louis.uah.edu/uah-dissertations/409>

This Dissertation is brought to you for free and open access by the UAH Electronic Theses and Dissertations at LOUIS. It has been accepted for inclusion in Dissertations by an authorized administrator of LOUIS.

**A COMPUTATIONAL INVESTIGATION OF  
FIREBRAND DISPERSION AND  
DEPOSITION IN AREAS WITH CUBIC  
STRUCTURES**

**Aditya Prakash Mankame**

**A DISSERTATION**

**Submitted in partial fulfillment of the requirements  
for the degree of Doctor of Philosophy**

**in**

**Mechanical Engineering**

**to**

**The Graduate School**

**of**

**The University of Alabama in Huntsville**

**August 2024**

**Approved by:**

Dr. Babak Shotorban, Committee Chair  
Dr. Jason Cassibry, Committee Member  
Dr. Chang-kwon Kang, Committee Member  
Dr. Udaysankar Nair, Committee Member  
Dr. Sarma Rani, Committee Member  
Dr. George Nelson, Department Chair  
Dr. Shankar Mahalingam, College Dean  
Dr. Jon Hakkila, Graduate Dean

## **Abstract**

# **A COMPUTATIONAL INVESTIGATION OF FIREBRAND DISPERSION AND DEPOSITION IN AREAS WITH CUBIC STRUCTURES**

**Aditya Prakash Mankame**

**A dissertation submitted in partial fulfillment of the requirements  
for the degree of Doctor of Philosophy**

**Mechanical Engineering**

**The University of Alabama in Huntsville**

**August 2024**

The spread of wildland and wildland urban interface (WUI) fires can be caused by spotting, where embers from a primary fire ignite spot fires. This study investigates the dispersion and deposition of firebrands over cubic structures in WUI regions under wind condition. Large eddy simulation was used for turbulence while tracing firebrands in Lagrangian framework, employing the open source software Fire Dynamics Simulator (FDS). The software program was revised to include a firebrand model where the rotational motion and thermal degradation of firebrands were taken into account in addition to the translation motion. This was used for simulation of cylindrical. The simulation included a firebrand depositing over single isolated block and multiple neighboring blocks in different configurations with varying wind speeds and separation distances. Both scenarios showed a safe zone on the leeward side of the blocks where no firebrands were deposited. The safe zone had a rectangular shape, with width matching the block and length proportional to the block's height and wind speed. For tandem blocks, the safe zone extended onto the windward face of the trailing block with smaller separation distances and higher wind speeds. No

firebrands were observed to deposit on the leeward face of the blocks in either scenario. The normalized number density (NND) of deposited firebrands was analyzed based on landing positions. At lower wind speeds, fewer firebrands were deposited on the top face of the block compared to the ground. Additionally, for blocks with longer length, the concentration of firebrands increased towards the trailing edge. Another firebrand model was developed and integrated in FDS to investigate the deposition and accumulation of cuboidal firebrands released from a firebrand-generating apparatus (Dragon) onto two adjacent blocks, as observed in previous experiments by Suzuki and Manzello [75]. In this model, firebrands were assumed to be influenced by drag and gravity during flight, and by drag and friction while sliding on the ground. These simulation revealed various flow features such as, the re-circulating region in the dragon's wake, crossflow region upwind of the blocks and twin re-circulation region on the leeward side of the blocks affecting firebrand motion. At lower wind speeds, firebrands tended to accumulate between the dragon and the blocks. Conversely, at higher wind speeds, the firebrands tended to cluster momentarily before the crossflow region and then move swiftly through the space between the blocks, with some exiting the domain and others accumulating on the leeward edge of the blocks. The dispersion of firebrands was found to be significantly greater in the streamwise direction compared to the spanwise direction due to the higher rms velocity in the former direction.



## Acknowledgements

I extend my deepest gratitude to my advisor, Dr. Babak Shotorban, for entrusting me with the opportunity to engage in research alongside him. His unwavering guidance and mentorship have not only contributed significantly to my academic and professional growth but have also been invaluable pillars of support during personal challenges. I am also indebted to my esteemed committee members, Dr. Jason Casibry, Dr. Chang-kwen Kang, Dr. Udyasankar Nair, and Dr. Sarma Rani, for having imparted invaluable knowledge through your courses, enriching my understanding and shaping my research endeavors.

Special appreciation goes to my former lab-mate Dr. Chandand Anand for her invaluable assistance in navigating the intricacies of computational models during the initial phase of my research. I am also grateful to Dr. David Young (ASC) for his prompt and insightful responses regarding the several questions I had about super-computer facilities Alabama Supercomputer Authority that I used for my simulations. Furthermore, I am deeply thankful to Dr. Samuel Manzello and Dr. Sayaka Suzuki for graciously sharing their insights regarding their experiments, which have greatly enhanced the depth of my dissertation. To my former lab-mate Dr. Peyman Rahim Borujerdi and current lab-mate Patrick Damiani, I extend my sincere appreciation for their invaluable contributions to my academic journey at UAH. Lastly, my heartfelt thanks go to my family in India, especially my parents; and my family in Huntsville for their unwavering support.

I would like to acknowledge U.S. Department of Commerce, National Institute of Standards and Technology (award 70NANB17H281) for providing financial assistance.

# Table of Contents

<b>Abstract</b> . . . . .	<b>ii</b>
<b>Acknowledgements</b> . . . . .	<b>v</b>
<b>Table of Contents</b> . . . . .	<b>viii</b>
<b>List of Figures</b> . . . . .	<b>ix</b>
<b>List of Tables</b> . . . . .	<b>xii</b>
<b>Chapter 1. Introduction</b> . . . . .	<b>1</b>
1.1 Wildland and Wildland Urban Interface Fires . . . . .	1
1.2 Spotting . . . . .	3
1.3 Flow Over Ground Mounted Blocks . . . . .	8
1.4 Motivation and Objective . . . . .	10
1.5 Outline . . . . .	11
<b>Chapter 2. Mathematical Methodology and Computational Approach</b> . . . . .	<b>13</b>
2.1 Introduction . . . . .	13
2.2 Cylindrical Firebrands . . . . .	14

2.3	Cuboidal Firebrands . . . . .	19
2.4	Mass and Temperature Loss . . . . .	22
2.5	Computational Approach . . . . .	24
<b>Chapter 3. Cylindrical Firebrand Deposition on a Single Block</b>		<b>26</b>
3.1	Introduction . . . . .	26
3.2	Computational Setups . . . . .	26
3.2.1	Firebrand Release in No-wind Condition . . . . .	26
3.2.2	Flow Validation Over a Single Block . . . . .	27
3.2.3	Firebrand Deposition in the Flow Over a Single Block .	29
3.3	Results and Discussion . . . . .	31
3.3.1	Firebrand Release in No-wind Condition . . . . .	31
3.3.2	Flow Validation Over a Single Block . . . . .	34
3.3.3	Firebrand Deposition in the Flow Over a Single Block .	38
3.4	Chapter Summary . . . . .	45
<b>Chapter 4. Cylindrical Firebrands Deposition on Three Neighboring Blocks</b>		<b>48</b>
4.1	Introduction . . . . .	48
4.2	Computational Setups . . . . .	48
4.2.1	Wind Tunnel Scale Flow . . . . .	48

4.2.2	Field-Scale Flows with Firebrands . . . . .	50
4.3	Results and Discussion . . . . .	52
4.3.1	Wind Tunnel Scale Flow . . . . .	52
4.3.2	Field-Scale Flow with Firebrands . . . . .	58
4.4	Chapter Summary . . . . .	79
 <b>Chapter 5. Cuboidal Firebrand Deposition Between Two Ad-</b>		
<b>  jacent Blocks . . . . .</b>		<b>82</b>
5.1	Introduction . . . . .	82
5.2	Computational Setup . . . . .	82
5.3	Results and Discussion . . . . .	85
5.4	Chapter Summary . . . . .	105
 <b>Chapter 6. Summary and Conclusions . . . . .</b>		<b>107</b>
 <b>References . . . . .</b>		<b>111</b>

## List of Figures

1.1	Schematic diagram for spotting mechanism in WUI areas. . . . .	4
1.2	Stages of Spotting mechanism. . . . .	4
2.1	Schematic representation of the forces exerted on a cylindrical firebrand being transported by the fluid flow [5, 4]. . . . .	15
3.1	Computational domain for the block used in the model validation against the experimental data of Lim <i>et al.</i> [34]. . . . .	28
3.2	Computational configuration in the firebrand deposition study with a block $3 \times 3 \times 3$ m. . . . .	30
3.3	Trajectory of a cylindrical particle released in still air condition in present simulations; and previous numerical and experimental data. . . . .	33
3.4	Mean velocity streamlines for flow over a $8 \times 8 \times 8$ cm block in a validation study. . . . .	35
3.5	Pressure coefficient on the surface of the block in present simulation; and previous simulation and experiments. . . . .	36
3.6	The mean velocity components over the top face of the block in present simulation; and previous simulation and experiments. . . . .	37
3.7	The rms of velocity components over the top face of the block in present simulation; and previous simulation and experiments. . . . .	38
3.8	Mean velocity streamlines superimposed on the contour plots of mean velocity magnitude at slice $y = 0$ for various cases. . . . .	39
3.9	Contour plots of normalized number density of the deposited firebrand on the ground and top face block for various cases. . . . .	41
3.10	Length of the safe zone versus the height of the block $H$ where $L = W = 3$ m. . . . .	42
3.11	Normalized number density of deposited firebrands vs $x/h$ and $y/h$ for various cases. . . . .	43

3.12	Location and temperature of the firebrands deposited on the faces of the block with $L = W = 3$ m and $H = 6$ m. . . . .	46
4.1	Computational domain for flow over blocks in (a) tandem arrangement; and (b) parallel arrangements. . . . .	49
4.2	Computational configurations in the field scale simulations of firebrand deposition tandem (T) and parallel (A) arrangements. . . . .	51
4.3	Pressure coefficient and velocity over a single block seen in present simulations; and previous simulations and experiments. . . . .	53
4.4	Pressure coefficient and velocity over blocks in tandem in present simulations and previous simulations. . . . .	55
4.5	Pressure coefficient and velocity over blocks in parallel in present simulations; and previous simulations and experiments. . . . .	57
4.6	GCI index on the profile for the pressure coefficient and velocity over the field scale block. . . . .	59
4.7	Contour plot for mean streamlines, velocity and TKE for the flow over blocks in tandem arrangement. . . . .	61
4.8	Normalized number density ( $NND_o$ ) vs $x/h$ at $y/h = 0$ for firebrands deposited on the ground in simulations with no blocks. . . . .	63
4.9	Contour plots for Normalized number density in the presence and absence of the blocks. . . . .	64
4.10	Contour plots of relative normalized number density ( $NND_{rel}$ ) for blocks in tandem arrangements. . . . .	65
4.11	Relative normalized number density ( $NND_{rel}$ ) vs $x/h$ for blocks in tandem arrangements at $y/h = 0$ for varying $S/h$ . . . . .	67
4.12	Scatter plot of the firebrands deposited on the leeward side of block T3 in tandem arrangement with $S/h = 1$ at $U_h = 12$ m/s. . . . .	69
4.13	Mean safe zone length $l_r$ and standard deviation of safe zone length $\sigma$ for blocks in tandem arrangement. . . . .	70
4.14	Scatter plots of the centers of mass of the firebrands deposited on the faces of blocks T1-3 the tandem arrangement. . . . .	72

4.15	Contour plot for mean streamlines, velocity and turbulent kinetic energy for the flow over blocks in parallel arrangement. . . . .	74
4.16	Contour plots for relative normalized number density ( $NND_{rel}$ ) for blocks in parallel arrangement. . . . .	76
4.17	Relative normalized number density ( $NND_{rel}$ ) vs $x/h$ for blocks in parallel arrangements at $y/h = 0$ for varying $S/h$ . . . . .	77
4.18	Mean safe zone length $l_r$ and standard deviation of safe zone length $\sigma$ for blocks in parallel arrangement. . . . .	78
5.1	The computational configuration resembling previous experimental setup [75]. . . . .	83
5.2	Mean streamline superimposed on the contour plots of mean flow velocity at (a) $y = 0$ m; and (b) $z = 0$ m for wind speed of 10 m/s. . . . .	86
5.3	Normalized mean flow velocity magnitude and rms of the flow velocity components at $z = 0$ m and $y = 0$ m. . . . .	88
5.4	The integral time scale in the streamwise and vertical directions at varying wind speeds. . . . .	90
5.5	Scatter plot of firebrands overlaid on contour plot of instantaneous flow velocity magnitude on the ground at $U_w = 6$ m/s. . . . .	92
5.6	Scatter plot of firebrands overlaid on contour plot of instantaneous flow velocity magnitude on the ground at $U_w = 10$ m/s. . . . .	94
5.7	The mean streamwise position of firebrand in accumulation zone in present simulation compared with the previous experiments [75]. . . . .	95
5.8	Mean streamwise firebrand velocity and mean streamwise firebrand position vs time for varying wind speeds for $\mu = 0.5$ . . . . .	97
5.9	The mean of the absolute value of the spanwise firebrand position $ \langle y_p \rangle $ vs the mean streamwise firebrand position $\langle x_p \rangle$ . . . . .	99
5.10	The variance of the firebrand position in the streamwise direction $\langle x'_p x'_p \rangle$ vs the mean firebrand streamwise position $\langle x_p \rangle$ . . . . .	101
5.11	The variance of the firebrand position in the spanwise direction $\langle y'_p y'_p \rangle$ vs the mean firebrand streamwise position $\langle x_p \rangle$ . . . . .	104

## List of Tables

3.1	Different formulation of $x_{cp}/l$ used in previous [57] and present simulations. . . . .	27
3.2	Landing time of a cylindrical firebrand released in a still air in the previous experiment and simulation [57], and present simulations.	32
3.3	The locations of the center of the horseshoe vortex, stagnation point, flow and reattachment points around the block. . . . .	34
3.4	Number and average temperature (K) of firebrands deposited on the top, windward and lateral faces of the block. . . . .	45
4.1	Parameters varied in the field scale simulations with firebrand deposition. . . . .	51

# Chapter 1. Introduction

## 1.1 Wildland and Wildland Urban Interface Fires

Controlled wildfires that occur in wildland areas (*i.e.*, forestland, grasslands, shrublands) have advantageous effects [13] as they help in minimizing excessive growth and underbrush in forests thus being constructive. This, in turn, enables established trees to flourish with reduced competition for essential nutrients and space. However, it is important to note that uncontrolled and rapidly spreading wildfires in wildland and the interface between wildland and human settlements are destructive. These type of wildfires seen in the interface between the wildlands and human settlements more commonly know as Wildland Urban Interface (WUI) areas are of particular interest for this study.

According to National Inter-agency Fire Center, in the United States of America over the last 5 years over 300,000 thousands wildland fires occurred with an area of over 29 million acres of land that was burnt [14]. Among the 10 wildland firefighting geographic areas as classified by National Inter-agency Fire Center, Alaska has seen the the highest yearly average in acres burned of about 1.6 million acres per year from 2002-2022. On the other hand, the area of Northern California saw a massive 780% increase in average annual acres burned between the years 2002-2006 and 2018-2022. This has lead to an increase in fire suppression cost by

nearly 200% since 2002. These fires also destroyed somewhere in the vicinity of 50,000 residential and commercial structures in between the years of 2017-2022, as per the Congressional Research Service [23, 64]. Over \$ 22 billion of damages have been caused by wildfire during those 5 years, with \$ 18 billion just in the state of California.

Wildland and WUI fires are increasing in frequency, severity and impact each year worldwide [64, 14]. For example, the 2009 Victorian bushfires in Australia also known as the Black Saturday bushfires claimed the lives of 173 individuals and caused damage worth \$4 billion [77]. Also the bushfires of 2019-2020 were particularly devastating, burning millions of acres of land and causing significant loss of life and property [1]. More recently, in 2023 record breaking wildfires occurred in Canada burning 18 million hectares of forested land and some residential and non-residential structures [56]. These fires were severe enough to cause air quality, visibility issues across the north eastern part of the United States of America [44].

These wildland fires can be triggered by a combination of natural and human factors. Natural causes such as lightning strikes, earthquakes, volcanic eruptions, and other phenomena are known to ignite wildland fires. For instance, data from Wildfire Services [69] in B.C., Canada, revealed that 60% of wildland fires in the region were due to sustained lightning strikes. However, human activities are often the primary culprits behind wildland fires. Between 2018 and 2022, approximately 89% [14, 64] of wildland fires were determined to be human-caused. The encroachment of Wildland-Urban Interface (WUI) communities into

wildland areas further escalates the risk of human-caused wildland fires. These fires are frequently the result of negligent actions like improperly extinguished campfires, discarded cigarette butts, or burning debris.

Adverse climatic conditions, such as elevated temperatures, decreased humidity levels, and powerful winds, are instrumental in the formation of ideal circumstances for wildfires to emerge. The impact of climate change intensifies these conditions by leading to increased worldwide temperatures, diminished rainfall in certain areas, and consequently, a greater abundance of dry vegetation serving as fuel for fires. These unfavorable weather conditions further aid in the propagation of fires through a variety of mechanisms, encompassing short-range (convective, radiative, and conductive) as well as long-range (spotting) methods.

## 1.2 Spotting

In wildland and wildland-urban interface fires, the phenomenon of spotting stands out as a critical mechanism for the spread of fires [17, 29]. Spotting generally occurs in three stages, 1) firebrand generation, 2) transport and 3) ignition of recipient fuel [4]. Firebrands are burning or glowing particles of vegetation such as twigs, barks, leaves etc. or building materials such as wood shakes, fences, furnishing materials etc. [29, 83].

The generation of firebrands is attributed to a (*i.e.*, primary fire, which could be burning shrubbery, trees or other burning WUI structures. Flames and plumes of the primary fires in combination with the turbulent winds result in fragments from the source to break off. The ambient winds present during

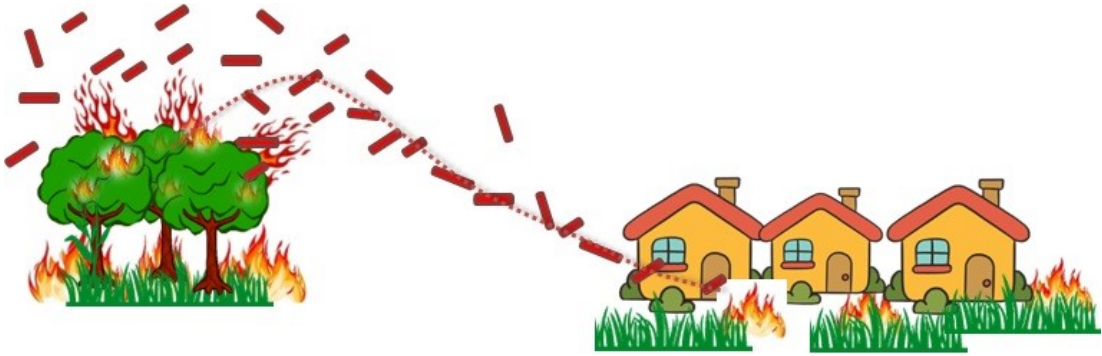


**Figure 1.1:** Schematic diagram for spotting mechanism in WUI areas.

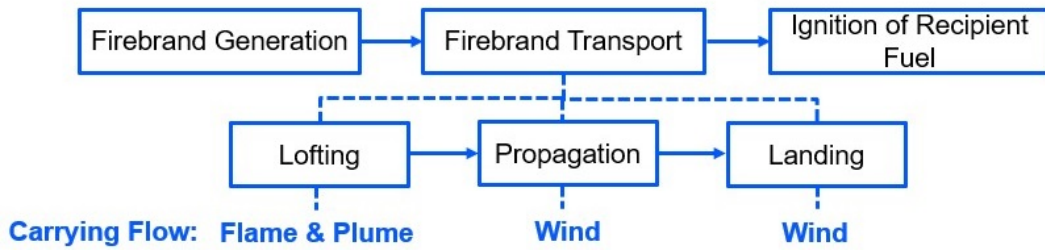


**Figure 1.2:** Stages of Spotting mechanism.

this process are responsible for the transport of firebrands from its source. The transport phase in spotting involves lofting of the firebrands from the source due to the convective plumes present in the primary fires, the firebrand propagation in the ambient turbulent winds and deposition or landing. These firebrands can travel short or long distances [76, 67], depending on firebrand properties such as mass, density, shape, etc. as well as the ambient wind and plume conditions. In a WUI area, firebrands of varying shapes and sizes can land on the ground near or possibly land on structures [53, 54] or enter them through openings such as

windows, doors, etc. This could potentially ignite the spot fires where they land and thus threaten the structures.

There have been several studies on the role of firebrands in the spread of wildland and WUI fires. Manzello *et al.* [38] performed experiments by burning two Douglas-fir trees with 2.6 and 5.2 m heights. They found that the generated firebrands were predominately cylindrical in shape with an average diameter of 3 mm and length of 40 mm for the shorter tree and 4 and 53 mm for the taller tree. Manzello *et al.* [39] constructed an apparatus capable of generating glowing firebrands and used it to release firebrand in a wind tunnel. The firebrands released in the wind-tunnel at 9 m/s experienced a mass loss of 20–40% when compared to firebrands released in no wind condition. More recently, Bouvet and Kim [8] developed a firebrands shape classification model from using information available in existing literature and a synthetic particle datasets. This model is capable of categorizing firebrands by complex shapes such as, rod-bent, rod-straight, blade-bent, etc., from available three-dimensional dataset. They achieved this categorization by considering multiple particle shape metrics, viz. flatness, sphericity, convexity, etc. Bouvet *et al.* [9] used a device to artificially generate and 3D track smoldering and flaming firebrands. They further used this data along with a pretrained neural network to characterize the combustion state (smoldering / flaming) of the firebrand in motion.

Tohidi and Kaye [79], Tohidi and Kaye [78] experimentally and computationally studied the lofting of firebrands in a wind tunnel where in addition to wind, a convective plume was included. They observed that for higher wind

speeds, the change in the initial vertical velocity of the convective column did not affect the mean or standard deviation of the heights where the firebrands lofted or the distances they traveled to land. Yin *et al.* [86], Oliveira *et al.* [57] developed numerical models for the firebrand transport accounting for the drag, lift and gravitational forces and their effect on the rotation of firebrands to model both translational and rotational motions of cylindrical firebrands. To validate their model, Oliveira *et al.* [57] performed computations and experiments for a cylindrical firebrand (balsa wood) falling from an elevated point under a no ambient flow condition. The influence of different formulations for the distance between center of pressure and center of mass of a cylindrical object in motion was explored in the modeling by Rayleigh [61], Marchildon *et al.* [41], Rosendahl [66], Yin *et al.* [86].

Suzuki and Manzello [75] conducted experiments in a wind tunnel with two parallel blocks mounted on the bottom wall. One of the blocks was also attached to one of the lateral walls of the wind tunnel and the other block was attached to the opposite lateral wall. They used the Dragon [40], an apparatus capable of generating glowing firebrands, to release rectangular cubic firebrands upwind of the spacing between the blocks. They observed the accumulation of deposited firebrands in a zone between the dragon and structures at lower wind speeds. At higher wind speeds, no accumulation was observed, as firebrands continued to slide on the bottom surface of the wind tunnel and eventually exit the wind tunnel.

Nguyen and Kaye [54] quantified the mass of non-burning firebrands accumulated on the roof of scaled down building models in isolation within a wind tunnel. They observed that most firebrands that landed on the roof blew away and those that did not, accumulated on the internal corners of the roof. The mass of the accumulated firebrands decreased with an increase in wind speeds. They later also performed similar experiments where they placed multiple buildings surrounding the target building [53]. They concluded that introducing buildings upwind and having a smaller separation distance increased the mass of firebrands accumulated on the roof of the target building which they attributed to flow characteristics.

Anand *et al.* [4] performed simulations to investigate the deposition of cylindrical firebrands carried by a turbulent flow in an open area. They released firebrands from a fixed elevated point and assumed for firebrands to retain their mass from release to landing. They reported a bivariate Gaussian function like distribution for the landed firebrand position with a larger variance in the stream-wise direction, compared to the spanwise direction. Anand [5] performed similar simulations while allowing firebrands to experience mass loss due to thermal degradation, taking into account the effect of burning. They observed that, firebrands with a higher mass density ( $570 \text{ kg/m}^3$ ) experienced a higher mass loss, as compared to lower density ( $230 \text{ kg/m}^3$ ) firebrands. The lower density firebrands cooled rapidly and reached ambient temperature before landing. On the other hand, the higher density firebrands retained more thermal energy while flying, thus had higher temperatures at landing. Song *et al.* [74] performed wind tunnel

experiments with disc-shape firebrands and showed the deposited firebrands had uni-modal distribution except for certain wind speed and firebrand conditions where they displayed a bimodal distribution.

From a broader perspective, the spread of Wildland and WUI fires can also be influenced by the prevailing weather conditions. In this context, there are some numerical works that account for two-way coupling between these fires and the atmosphere. This is achieved by a numerical weather modeler, the Weather Research and Forecasting (WRF) model, which incorporates a fire module specifically designed to simulate the spread of fire in various terrains while actively considering its interaction with the surrounding weather conditions. Simpson *et al.* [71] utilized the WRF-Fire model to study the spread of a wildland fire across a steep leeward slope, perpendicular to the prevailing winds. Trucchia *et al.* [80] developed a probabilistic model using WRF-Fire to predict the spread of large-scale wildfires through spotting mechanisms. Ongoing research by Frediani *et al.* [19, 18] focuses on understanding the newly developed firebrand spotting parameterization in WRF-Fire. They apply this parameterization to analyze the recent Marshall Fire in Colorado, studying the transport of spherical firebrands in their investigation.

### **1.3 Flow Over Ground Mounted Blocks**

The flow patterns induced by structures on the wind flow is speculated to have an impact on the firebrands depositing on or near structures. The properties of the flows induced by structures have been the subject of several studies. In

many of these studies, the structures are represented by ground-mounted blocks. Some of these investigations, spearheaded by researchers such as Murakami *et al.* [52], Werner and Wengle [84], and Rodi [65], used large eddy simulation (LES) to understand the flow patterns seen over single cubic block. One of the earliest works by Murakami *et al.* [52], who simulated a block submerged in a boundary layer using large-eddy simulation (LES). Werner and Wengle [84], Rodi [65] computationally studied a block mounted on a surface in a channel flow with a Reynolds number of  $O(10^4)$  based on the velocity at the height of the block. Werner and Wengle [84], Rodi [65] showed the existence of a horse-shoe vortex on the windward side of the block and flow separation and reattachment on the top face of the block. Rodi [65], using different turbulence models, reported two counter rotating re-circulation region on the leeward side of the block. Vortex shedding was observed originating from the lateral faces with a pair of re-circulation region closer to these faces.

More recently, Richards *et al.* [63] claimed the pressure coefficient on the surface of the block is independent of the Reynolds number via a field test. Later in wind-tunnel experiments (Richards *et al.* [62]), they observed a drop in the pressure coefficient on the windward and leeward faces of the block as the wind direction changed from  $90^\circ$  to  $45^\circ$  with respect to the windward face of the block. Lim *et al.* [34, 32] performed experiments and simulations for a flow around a block submerged in a turbulent atmospheric surface layer (ASL) and showed that the mean profiles of pressure coefficient and velocity components are independent of the Reynolds number.

Several studies were also performed for multiple cubic blocks submerged in the flow. Martinuzzi and Havel [42]; and Farhadi and Sedighi [16] ventured into wind tunnel experiments and LES to study the behavior of two blocks positioned in tandem arrangements. Martinuzzi and Havel [42] observed that horseshoe vortex, flow separation and reattachment form over both of the blocks when their separation distance was large enough. Farhadi and Sedighi [16] found that the turbulence intensities in the intermediate region between the blocks increased with the separation distance. Lim and Ohba [33] performed detached eddy simulations (DES) using the commercial software Ansys FLUENT for the flows over three blocks arranged in tandem and parallel arrangements for varying separation distances. They observed that the pressure coefficient over the center block in the parallel arrangement was consistently lower than the pressure coefficient over the same block in a single block arrangement. On the other hand, they found little difference between the pressure coefficients of the first block in the tandem arrangement and the same block in the single block arrangement.

#### **1.4 Motivation and Objective**

As seen from above, there has been a considerable amount of experimental and numerical work done in the areas of firebrands transport, including studies by Manzello et al [39], Tohidi and Kaye [79, 78], Anand *et al.* [5], and numerous others. Some recent experimental works in regards to firebrands deposition and accumulation around structures such as those by Suzuki and Manzello [75] and Nguyen and Kaye [53, 54]. However, there is a lack of numerical work that

looks into the firebrands depression and deposition under the influence of the flow around a structure. Thus, this work aims to improve the understanding of this phenomenon in WUI areas with the help of numerical tools which in turn can help come up with better strategies to manage spot fires and mitigate resulting losses. As such, the main objective of this work is to study the firebrand deposition over and near structures. To achieve this, the current work uses a computational approach where the flow is simulated by LES combined with the Lagrangian particle tracking technique to represent moving firebrands. Through this approach, we specifically aim at simulating and understand deposition of firebrands in three scenarios:

- Firebrand deposition on and around single WUI structures.
- Firebrand deposition on and around multiple WUI structures in tandem and parallel arrangements.
- Firebrand deposition and accumulation around two adjacent blocks in parallel.

## 1.5 Outline

Following the introduction in the present sections 1.1-1.4, a computational model to track cylindrical cuboidal firebrand is detailed in Chapter 2. Later on, the cylindrical firebrand tracking model described in the earlier chapter is used to study the deposition characteristics of burning firebrands on and around a single rectangular WUI structure of varying dimensions in Chapter 3. Chapter 4 makes

use of the same cylindrical firebrand tracking model to understand the deposition characteristics on and around multiple cubic WUI structures arranged in tandem and parallel with varying separation distance and wind speeds. In Chapter 5 a cuboidal firebrand tracking model is developed and implemented in FDS and used to compare numerical results with previous experimental work which focused on firebrands released from a dragon into a wind tunnel and onto two blocks study rectangular. This work is summarized with some important conclusion given in Chapter 6 and some recommendations for future works is also mentioned in this chapter.

## Chapter 2. Mathematical Methodology and Computational Approach

### 2.1 Introduction

In this chapter, the equations representing the motion and the mass and thermal energy losses of firebrands are shown. These equations are implemented in the open source software Fire Dynamics Simulator (FDS), which simulates the flow through Large-Eddy Simulation (LES) [45, 46]. The features of FDS relevant to this project are reviewed in the §2.5. The firebrands are tracked in the Lagrangian framework. Dealing with particles in such a manner with equations coupled with the flow equations described via Direct Numerical Simulation (DNS) or LES, remains a prevalent modeling approach for systems involving dispersed particles in various applications [30, 36, 4, 24, 58, 48, 60, 6].

In the Lagrangian framework, the position and velocity of the firebrand are described by:

$$\frac{d\vec{x}_p}{dt} = \vec{V}_p, \quad (2.1)$$

$$m_p \frac{d\vec{V}_p}{dt} = \sum \vec{F}, \quad (2.2)$$

where,  $\vec{x}_p$  (m) and  $\vec{V}_p$  (m/s) denote the position and velocity of the center of mass of the firebrand, respectively. The time derivative in the Lagrangian framework is expressed as  $d/dt$ . Eq. (2.2) is an expression of Newton's second law where  $m_p$  (kg) is the mass of the firebrand and the forces acting on the firebrands while in translation are expressed as a summation of forces indicated by  $\sum \vec{F}$  (N).

Two different models are used in this work for calculation of  $\sum \vec{F}$  in eq. (2.2), one for cylindrical firebrands and the other for cuboidal firebrands.

## 2.2 Cylindrical Firebrands

This shape of firebrands is fairly common and is wild seen in wildland and WUI fire [38, 5, 4]. Fig. 2.1, shows the schematic of the forces exerted on a cylindrical firebrand carried by a flow.

In the model used for tracking the flying cylindrical firebrands, the right hand side of eq. (2.2) is  $\sum \vec{F} = \vec{F}_D + \vec{F}_L + \vec{F}_G$  where  $\vec{F}_D$ ,  $\vec{F}_L$  and  $\vec{F}_G$  represent the forces of drag, lift and gravity combined with buoyancy force, respectively, which are calculated by

$$\vec{F}_G = (\rho_p - \rho_{\text{air}}) \mathcal{V} \vec{g}, \quad (2.3)$$

$$\vec{F}_D = \frac{1}{2} C_D \rho_{\text{air}} D_p l \left| \vec{V}_{\text{rel}} \right| |\sin \alpha|^3 \vec{V}_{\text{rel}}, \quad (2.4)$$

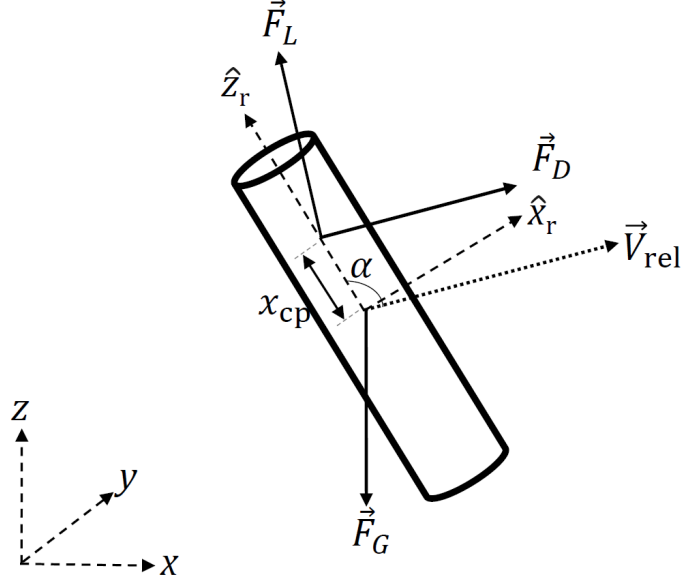


**Figure 2.1:** Schematic representation of the forces exerted on a cylindrical firebrand being transported by the fluid flow [5, 4].

$$\vec{F}_L = \frac{1}{2} C_D \rho_{\text{air}} D_p l \left( \left| \vec{V}_{\text{rel}} \right| \sin \alpha \right)^2 \cos \alpha \frac{\hat{z}_r \times \vec{V}_{\text{rel}} \times \vec{V}_{\text{rel}}}{\left| \hat{z}_r \times \vec{V}_{\text{rel}} \times \vec{V}_{\text{rel}} \right|}, \quad (2.5)$$

$$C_D = \begin{cases} \frac{10}{\text{Re}_\alpha^{0.778}}, & \text{for } \text{Re}_\alpha \leq 0.1, \\ \frac{10}{\text{Re}_\alpha^{0.778}} (1 + 0.1076 \text{Re}_\alpha^{0.778}), & \text{for } 0.1 < \text{Re}_\alpha \leq 6 \times 10^3, \\ 1.1, & \text{for } 6 \times 10^3 < \text{Re}_\alpha \leq 2 \times 10^5. \end{cases} \quad (2.6)$$

Here,  $\rho_p$ ,  $D_p$ ,  $l$ ,  $\mathcal{V}$  and  $\vec{V}_{\text{rel}}$  are the firebrand density ( $\text{kg}/\text{m}^3$ ), diameter (m), length (m), volume ( $\text{m}^3$ ) and velocity (m/s) relative to the flow at the center of mass of the particle, respectively. It is calculated by  $\vec{V}_{\text{rel}}(t) = \vec{U}(\vec{x}_p(t), t) - \vec{V}_p(t)$  where the

first term indicates the flow velocity at the position of the center of mass of the firebrand. The drag coefficient  $C_D$  is calculated, using the particle Reynolds number  $Re_\alpha = D_p \rho_{\text{air}} |\vec{V}_{\text{rel}}| \sin \alpha / \mu_{\text{air}}$  [28], where  $\rho_{\text{air}}$  and  $\mu_{\text{air}}$  are the density ( $\text{kg}/\text{m}^3$ ) and dynamic viscosity ( $\text{kg}/\text{ms}$ ) of air respectively; and  $\alpha$  is the incidence angle ( $^\circ$ ) between the relative velocity and the major axis of the cylindrical firebrand  $\hat{z}_T$ .

These cylindrical firebrands also to undergo rotational motion while in transit through air as a result of the hydrodynamic and resistive torques acting along the length of the firebrand. The Euler equation for the rotational motion in this section are only given as follows:

$$I_{x'} \frac{d\omega_{x'}}{dt} - \omega_{y'} \omega_{z'} (I_{y'} - I_{z'}) = T_{x'}, \quad (2.7)$$

$$I_{y'} \frac{d\omega_{y'}}{dt} - \omega_{z'} \omega_{x'} (I_{z'} - I_{x'}) = T_{y'}, \quad (2.8)$$

$$I_{z'} \frac{d\omega_{z'}}{dt} - \omega_{x'} \omega_{y'} (I_{x'} - I_{y'}) = T_{z'}, \quad (2.9)$$

where  $\vec{\omega} = \{\omega_{x'}, \omega_{y'}, \omega_{z'}\}$ ,  $\vec{T} = \{T_{x'}, T_{y'}, T_{z'}\}$  and  $I_{x'}, I_{y'}, I_{z'}$  are the rotational velocity ( $\text{s}^{-1}$ ), total torque ( $\text{N} \cdot \text{m}$ ) vector and moment of inertia ( $\text{kg} \cdot \text{m}^2$ ). Here, the  $x', y', z'$  system is the principal axes attached to the cylinder with the origin at its center of mass and  $z'$  aligned with the major axis of the cylinder. The total torque is the addition of the torque  $\vec{T}_{\text{hydro}}$  due to the hydrodynamic forces ( $\text{N} \cdot \text{m}$ )

and the torque  $\vec{T}_{\text{resist}}$  due to the frictional ( $\text{N} \cdot \text{m}$ ) air resistance experienced by the firebrand [57]:

$$\vec{T} = \vec{T}_{\text{hydro}} + \vec{T}_{\text{resist}}, \quad (2.10)$$

$$\vec{T}_{\text{resist}} = \sqrt{(T_{\text{resist}}^{x'})^2 + (T_{\text{resist}}^{y'})^2}, \quad (2.11)$$

$$T_{\text{resist}}^{x'} = -\rho_{\text{air}} |\omega_{x'}| \omega_{x'} a b^4 \left( 0.538 + 3.62 \left( \frac{\rho_{\text{air}} a |\omega_{x'}| b}{\mu_{\text{air}}} \right)^{-0.778} \right), \quad (2.12)$$

$$T_{\text{resist}}^{y'} = -\rho_{\text{air}} |\omega_{y'}| \omega_{y'} a b^4 \left( 0.538 + 3.62 \left( \frac{\rho_{\text{air}} a |\omega_{y'}| b}{\mu_{\text{air}}} \right)^{-0.778} \right), \quad (2.13)$$

$$\vec{T}_{\text{hydro}} = x_{\text{cp}} \mathbf{A} \cdot \left[ \hat{z}_r \times \left( \vec{F}_D + \vec{F}_L \right) \right], \quad (2.14)$$

$$x_{\text{cp}} = l(90 - \alpha) / 480, \quad (2.15)$$

where  $a = D_p/2$  is the radius (m) of the firebrand,  $b = l/2$  is the half length (m) and  $x_{\text{cp}}$  is the distance (m) between the centre of pressure and the centre of mass [41], and  $\mathbf{A}$  is the transformation matrix expressed in terms of quaternions  $\epsilon_1, \epsilon_2, \epsilon_3$  and  $\eta$  [86]:

$$\mathbf{A} = \begin{bmatrix} 1 - 2(\epsilon_2^2 + \epsilon_3^2) & 2(\epsilon_1\epsilon_2 + \epsilon_3\eta) & 2(\epsilon_1\epsilon_3 - \epsilon_2\eta) \\ 2(\epsilon_2\epsilon_1 - \epsilon_3\eta) & 1 - 2(\epsilon_3^2 + \epsilon_1^2) & 2(\epsilon_2\epsilon_3 + \epsilon_1\eta) \\ 2(\epsilon_1\epsilon_3 + \epsilon_2\eta) & 2(\epsilon_3\epsilon_2 - \epsilon_1\eta) & 1 - 2(\epsilon_1^2 + \epsilon_2^2) \end{bmatrix}. \quad (2.16)$$

Quaternions are governed by

$$\frac{d}{dt} \begin{bmatrix} \epsilon_1 \\ \epsilon_2 \\ \epsilon_3 \\ \eta \end{bmatrix} = \frac{1}{2} \begin{bmatrix} \eta\omega_x - \epsilon_3\omega_y + \epsilon_2\omega_z \\ \epsilon_3\omega_x + \eta\omega_y - \epsilon_1\omega_z \\ -\epsilon_2\omega_x + \epsilon_1\omega_y + \eta\omega_z \\ -\epsilon_1\omega_x - \epsilon_2\omega_y - \epsilon_3\omega_z \end{bmatrix}. \quad (2.17)$$

The quaternions are correlated with Euler angles  $\phi, \psi, \theta$  ( $^\circ$ ) through the following equations, which are used here to find initial values of the quaternions:

$$\epsilon_1 = \cos\left(\frac{\phi - \psi}{2}\right) \sin\left(\frac{\theta}{2}\right), \quad (2.18)$$

$$\epsilon_2 = \sin\left(\frac{\phi - \psi}{2}\right) \sin\left(\frac{\theta}{2}\right), \quad (2.19)$$

$$\epsilon_3 = \sin\left(\frac{\phi + \psi}{2}\right) \cos\left(\frac{\theta}{2}\right), \quad (2.20)$$

$$\eta = \cos\left(\frac{\phi + \psi}{2}\right) \cos\left(\frac{\theta}{2}\right). \quad (2.21)$$

In the model presented in this section, it was assumed that the firebrands stays at the point where it lands and does not experience any other motion, such as sliding.

### 2.3 Cuboidal Firebrands

The second type of firebrands considered in this work are cuboidal firebrands used in previous experimental work by Suzuki and Manzello [75]. The motion of these cuboidal firebrands can be given by eqs. (2.1) and (2.2). In this model the flying motion of the cuboidal firebrands the right hand side of eq. (2.2) is  $\sum \vec{F} = \vec{F}_D + \vec{F}_G$  where  $\vec{F}_D$  and  $\vec{F}_G$  are the forces of drag and gravity combined with the buoyancy force  $\vec{F}_G$ , respectively. The expression for  $\vec{F}_G$  is identical to eq. (2.3) and the drag force  $\vec{F}_D$  which is expressed as follows:

$$\vec{F}_D = \frac{1}{2} C_D \rho_{\text{air}} h_p l \left| \vec{V}_{\text{rel}} \right| \vec{V}_{\text{rel}}, \quad (2.22)$$

$$C_D = \frac{8}{\text{Re}_p \sqrt{\Phi_\perp}} + \frac{16}{\text{Re}_p \sqrt{\Phi}} + \frac{3}{\sqrt{\text{Re}_p \Phi^{3/4}}} + 0.421^{0.4(-\log(\Phi))^{0.2}} \frac{1}{\Phi_\perp}, \quad (2.23)$$

where  $h_p$  height (m) and in eq. (2.23),  $\text{Re}_p = d_v \rho_{\text{air}} |\vec{V}_{\text{rel}}| / \mu_{\text{air}}$  is the particle Reynolds number. Here,  $d_v$  is the diameter (m) of the volume equivalent sphere calculated by

$$d_v = 2 \left( \frac{3lh_p^2}{4\pi} \right)^{1/3}, \quad (2.24)$$

where  $lh_p^2$  is the volume of the firebrand, assuming two of the dimensions of the cuboid are identical to  $h_p$ , which is consistent with the shape of the firebrands used in the measurements of Suzuki and Manzello [75]. The expression for the drag force in eq. (2.22) is attributed to Hölzer and Sommerfeld [22]; Bagheri and Bonadonna [7] with  $C_D$  given in eq. (2.23) indicating the drag coefficient, and  $\Phi$  and  $\Phi_{\perp}$  representing sphericity and crosswise sphericity, respectively [22]. Here,  $\Phi$  is defined as the ratio between the surface area of the volume equivalent sphere and the surface area of the particle, and the crosswise sphericity  $\Phi_{\perp}$  is defined as the ratio between the cross-sectional area of the volume equivalent sphere and the projected cross-sectional area of the considered particle perpendicular to the flow. The equations of  $\Phi$  and  $\Phi_{\perp}$  are given as follows:

$$\Phi = \frac{\pi d_v^2}{2(2h_p l + h_p^2)}, \quad (2.25)$$

$$\Phi_{\perp} = \frac{\pi d_v^2 / 4}{lh_p}. \quad (2.26)$$

The cuboidal firebrands are also assumed to undergo sliding motion without any displacement in the vertical direction. The position and velocity of the sliding

cuboidal firebrand follow eqs. (2.1) and (2.2) in two dimensions tangent to the ground where and the right hand side of eq. (2.2) is expressed as  $\sum \vec{F}_D = \vec{F}_r + \vec{F}_D$  if  $|\vec{F}_D| > |\vec{F}_r|$ ; otherwise it is set to zero [73]. where  $\vec{F}_r$  is the friction force and is given by

$$\vec{F}_r = -\mu m_p |\vec{g}| \frac{\vec{F}_D}{|\vec{F}_D|}, \quad (2.27)$$

where  $\mu$  denotes the friction coefficient between the firebrand and the ground. The friction force act in the direction opposite to the drag forces. The drag force  $\vec{F}_D$  here is calculated by eqs. (2.22) and (2.23) with a vanishing component of the relative particle velocity in the direction normal to the ground surface. It is important to note that the formulation for the drag coefficient in eq. (2.23) is meant for particles in motion away from walls but has previously been used for particle motion on the surface [35, 50] Since, there is not enough work done for drag coefficient of non-spherical particles moving on the surface we used the formulation mention in the eq. (2.23).

The cuboidal firebrands near the ground are subject to the sub-layer and buffer layer effects that are formed on the walls in turbulent flows. However, when a wall model is used in the flow simulation, the details of the flow in these regions, such as the sharp wall-normal gradient in the viscous sub-layer, are not resolved. In the present study, to account for these effects on the firebrands deposited on the ground, the modified interpolation scheme suggested by Johnson *et al.* [26] was implemented in FDS by modifying its program source. This scheme is specifically designed for particles near the wall, where the flow is simulated by

LES in conjunction with the wall model. More specifically, the flow velocity at the location of the firebrand is calculated from the flow velocity at the first grid point off the wall using:

$$\vec{U}(y_p, t) = f(y^+) \vec{U}(y_{1/2}, t), \quad (2.28)$$

$$u_{\parallel}(y_p, t) = f(y^+) u_{\parallel}(y_{1/2}, t), \quad (2.29)$$

$$f(y^+) = \frac{u^*(y_p^+)}{u^*(y_{1/2}^+)}, \quad (2.30)$$

where  $u_{\parallel}$  is the flow velocity component parallel to the wall, and  $y_p$  and  $y_{1/2}$  are the wall-normal coordinates (*i.e.*,  $y$  coordinates here) of the center of mass of the firebrand and the first grid off the wall, respectively. Also,  $y_p^+$  and  $y_{1/2}^+$  are the wall coordinates of the firebrand center of mass and the first grid off the well. Here,  $u^*$  is the flow velocity non-dimensionalized by the wall-friction velocity given by Liakopoulos [31]:

$$u^*(y^+) = \ln [(y^+ + 4.67)^{2.24} (y^{+2} - 6.82y^+ + 48.05)^{0.101}] + 4.22 \tan^{-1}(0.166y^+ - 0.565) - 1.67. \quad (2.31)$$

## 2.4 Mass and Temperature Loss

The cylindrical firebrand are considered to be burning. Which mean they undergoes thermal degradation by losing mass as a result of pyrolysis and char ox-

idation. To take this effect into account, the firebrand is assumed to be thermally thin particle with a mass governed by:

$$\frac{dm_p}{dt} = -\dot{m}_{\text{pyr}} - \dot{m}_{\text{char}}, \quad (2.32)$$

where  $\dot{m}_{\text{pyr}}$  (kg/s) and  $\dot{m}_{\text{char}}$  (kg/s) are the mass loss rates due to pyrolysis and char oxidation, respectively. These are modeled by:

$$\dot{m}_{\text{pyro}} = -m_p A_{\text{pyro}} \exp\left(-\frac{T_{\text{pyro}}}{T_p}\right), \quad (2.33)$$

$$\dot{m}_{\text{char}} = -\frac{\mathcal{V}}{s} A_{\text{char}} \alpha_p \sigma_p \rho_{\text{air}} \exp\left(-\frac{T_{\text{char}}}{T_p}\right) \left(1 + \beta_{\text{char}} \sqrt{\text{Re}_\alpha}\right), \quad (2.34)$$

where eqs. (2.33) and (2.34) are Arrhenius-type equations as given by [59]. Here,  $A_{\text{pyro}} = 725 \text{ s}^{-1}$  and  $T_{\text{pyr}} = 6899 \text{ K}$  are the pre-exponential factor and the activation temperature for pyrolysis and  $A_{\text{char}} = 430 \text{ m/s}$  and  $T_{\text{char}} = 9000 \text{ K}$  are the pre-exponential factor and the activation temperature for char oxidation, respectively [51, 68, 21]. The volume fraction of firebrand undergoing char oxidation is indicated by  $\alpha_p$  and the surface area-to-volume ratio for the firebrand is indicated by  $\sigma_p$ . In eq. (2.34),  $(1 + \beta_{\text{char}} \sqrt{\text{Re}_\alpha})$  is a correction factor with  $\beta_{\text{char}} = 0.2$  and stoichiometric coefficient for char oxidation  $s = 1.65$  as given in [59]. The firebrand temperature is governed by

$$m_p c_p \frac{dT_p}{dt} = -\Delta h_{\text{pyr}} \dot{m}_{\text{pyr}} - \Delta h_{\text{char}} \dot{m}_{\text{char}} - \dot{q}_c - \dot{q}_r, \quad (2.35)$$

where  $c_p$  is the heat capacity set to 1466 J/kgK and  $T_p$  is the firebrand temperature (K). In equation above,  $\Delta h_{\text{pyr}} = 418$  kJ/kg and  $\Delta h_{\text{char}} = 12 \times 10^3$  kJ/kg indicate the enthalpy of pyrolysis and char oxidation, respectively [68, 47, 4]. Also,  $\dot{q}_c$  and  $\dot{q}_r$  (W) denote the rates of the convective and radiative heat transfer, respectively, which are calculated by:

$$\dot{q}_c = h_c A (T_p - T_\infty), \quad (2.36)$$

$$\dot{q}_r = \sigma \epsilon A (T_p^4 - T_\infty^4), \quad (2.37)$$

where  $A$  is the surface area ( $\text{m}^2$ ) of the firebrand,  $T_\infty$  is the ambient temperature (K),  $h_c$  is the heat transfer coefficient ( $\text{W}/\text{m}^2\text{K}$ ),  $\sigma$  is the Stefan–Boltzmann constant ( $\text{W}/\text{m}^2\text{K}^4$ ) and  $\epsilon$  is the emmissivity of the firebrand set to 0.9. The firebrands are assumed to be thermally thin particle.

## 2.5 Computational Approach

A model capable of handling cylindrical firebrands' motion based on eqs. (2.3-2.21), mass and temperature loss based on eqs. (2.32-2.37) due to burning; and another model capable of handling cuboidal firebrands' translation and sliding motion based on eqs. (2.22-2.31) were developed and integrated within the Fire Dynamic Simulator (FDS, version 6.7.0) [45, 46].

FDS is an open source code based on computational fluid dynamics (CFD) that can simulate fire scenarios including thermal, chemical, and physical pro-

cesses such as combustion, turbulence, and radiation. In the present study, only the fluid dynamical aspects of FDS are utilized. The low-Mach number flow equations are solved using a second order predictor-corrector scheme in both space and time on a staggered grid. Turbulence is handled through large eddy simulations (LES) with the Deardoff sub-grid model [15] and the Wall-Adapting Local Eddy-viscosity model (WALE) [55] as the near-wall model.

The equations governing the motion of firebrands are solved using a second-order Adams-Bashforth [81] time integration method in both the flying and sliding modes, as described by Anand *et al.* [5, 4]. During the computations, the velocity  $\vec{U}(\vec{x}_p(t), t)$ , as defined in §2.2, is calculated by performing a tri-linear interpolation of the flow velocities at the cell faces to the location of the firebrand’s center of mass. The flow solver is coupled with firebrand equations in one-way coupling, viz. the influence of firebrands on the flow is negligible. Moreover, it is assumed that firebrands do not exert any influence on each other.

## **Chapter 3. Cylindrical Firebrand Deposition on a Single Block**

### **3.1 Introduction**

In this chapter first, validation studies were performed to evaluate the cylindrical firebrand model discussed in Chapter 2. This was performed for firebrands released from an elevated point under no wind condition. Details on this are given in §3.2.1 and §3.3.1. Then the validation exercise to evaluate the flow simulation by FDS over a single cubic block with the details on the associated computational setup and results given are in §3.2.2 and §3.3.2, respectively. Finally, a numerical study was performed to simulate firebrand deposition over a single cubic block representing an isolated simplified structure in a WUI fire situation. The computational setup and results for these simulations are given in §3.2.3 and §3.3.3, respectively.

### **3.2 Computational Setups**

#### **3.2.1 Firebrand Release in No-wind Condition**

To validate the firebrand model, first, a firebrand drop test previously investigated both experimentally and computationally [57] was considered. The

exercise involved a non-burning cylindrical firebrand made from balsa wood with diameter 10 mm and length 80 mm, which was released from the height 8.7 m in a no-wind condition. At the release point, the firebrand had zero velocities and made an angle of  $60^\circ$  with the vertical axis. The firebrand mass density was reported  $\rho_p = 215.5 \text{ kg/m}^3$ . Using the firebrand model illustrated in §2.2,

**Table 3.1:** Different formulation of  $x_{cp}/l$  used in previous [57] and present simulations.

	Formula of $x_{cp}/l$	Reference
(a)	$0.75 \sin \alpha / (4 + \pi \cos \alpha)$	Rayleigh [61]
(b)	$(90 - \alpha) / 480$	Marchildon <i>et al.</i> [41]
(c)	$0.25(1 - \sin^3 \alpha)$	Rosendahl [66]
(d)	$0.125 \cos^3 \alpha$	Yin <i>et al.</i> [86]
(e)	$(90 - \alpha) / 480$	Oliveira <i>et al.</i> [57] (simulation)

the drop test was simulated here in a computational domain  $1.5 \times 1.5 \times 9 \text{ m}$  (length $\times$ width $\times$ height). In lieu of eq. (2.15) [41], other formulas (Table 3.1) have been also reported in the literature [61, 66, 86] for calculation of  $x_{cp}$ . As such a sensitivity study of the model to these formulas were also carried out here.

### 3.2.2 Flow Validation Over a Single Block

The flow generated by FDS was validated against the previous numerical simulation and experimental data obtained in a wind tunnel for a flow over a cubic block [34]. The test section of the wind tunnel had dimensions of  $4.5 \times 0.9 \times 0.6$

m (length×width×height) with a block of height of 0.08 m situated 2.36 m from the inlet of the tunnel. Fig. 3.1 displays the computational domain  $0.8 \times 0.4 \times 0.4$

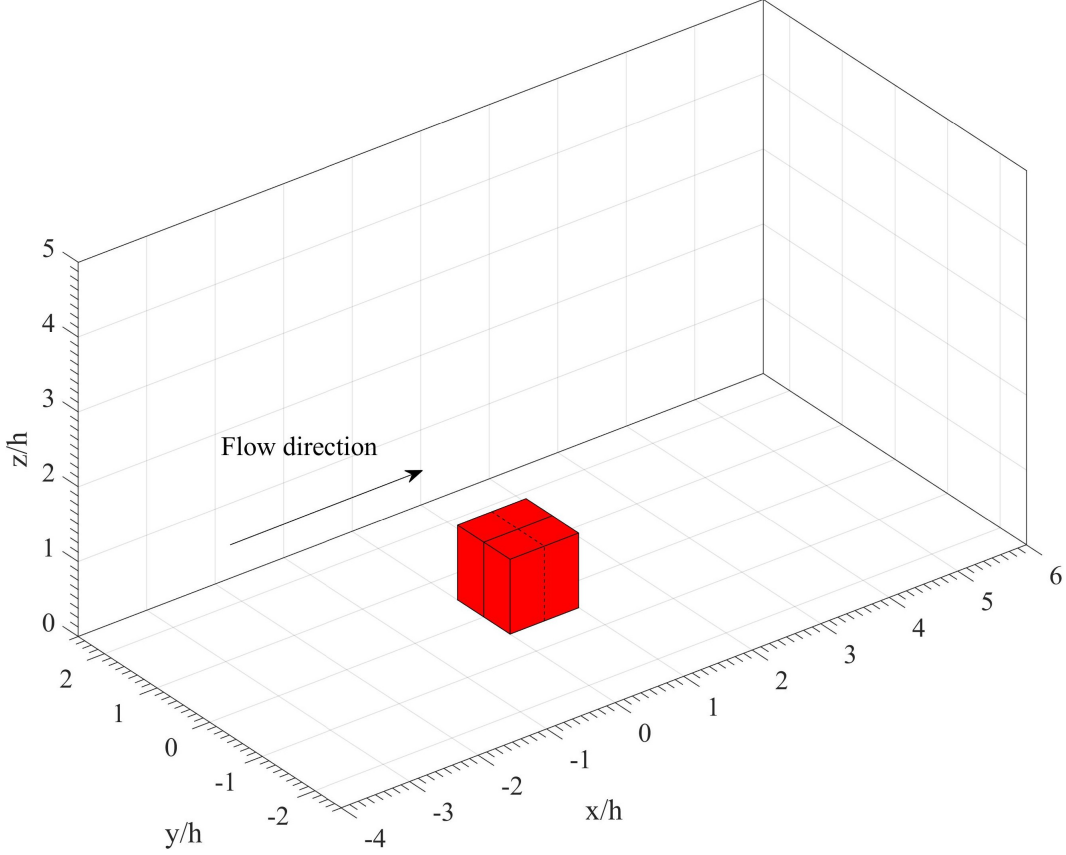


**Figure 3.1:** Computational domain  $10h \times 5h \times 5h$  for the block height,  $h = 0.08\text{m}$  with a grid resolution of  $320 \times 160 \times 160$  used in the model validation against the experimental data of Lim *et al.* [34]. The axial centerline (solid line) at  $y/h = 0$  and the transverse centerline (dashed line) at  $x/h = 0.5$  are shown.

m with a grid resolution of  $320 \times 160 \times 160$  and the block with height 0.08 m. The computational configuration and resolution here are consistent with the simulation by Lim *et al.* [34]. A power law profile was set as the inlet boundary condition with a power law exponent of 0.18. Consistent with the simulation of

Lim *et al.* [34], a Reynolds number of  $Re_h = U_h h / \nu = 20,000$ , where  $h$  is a reference length identical to the block height and  $U_h = 4.5$  m/s is the reference velocity at the inlet at the vertical location  $z = h$ . It is noted that Lim *et al.* [32] reported that they conducted their experiments for Reynolds numbers in the range between 18,600 and 73,100 but did not find the mean and variance of measured velocities to significantly change at this range of Reynolds numbers. The lateral and top boundaries were set to be free slip and the outflow boundary condition was set to be open. At the inlet, turbulence with the intensity of 5% was introduced. Flow turbulence was dealt with by LES with the Deardoff SGS [15] and near-wall models, as discussed in §2.5. However, the simulations were repeated with other SGS models including constant Smagorinsky [72], dynamic Smagorinsky [20, 49], Vreman [82] and RNG [85] available in FDS. It was determined that the results were negligibly sensitive to the SGS models. Hence, only the results of the Deardoff model are presented here.

### 3.2.3 Firebrand Deposition in the Flow Over a Single Block

Figure 3.2 shows the computational configuration used in the simulation of firebrand deposition in a flow over a single cubic block. The length, width and height of the block are indicated by  $L$ ,  $W$  and  $H$ , which are its dimensions in the  $x$ ,  $y$  and  $z$  directions, respectively. Simulations were carried out for blocks with various lengths, widths and heights. The domain size is  $75 \times 36 \times 36$  m in the  $x$ ,  $y$  and  $z$  directions, respectively. The domain is divided into two sub-domains with a finer grid size of  $0.15 \times 0.15 \times 0.15$  m between heights 0 to 12 m and a coarse grid ( $0.3 \times 0.3 \times 0.3$  m) between heights 12 m to 36 m. The inlet flow

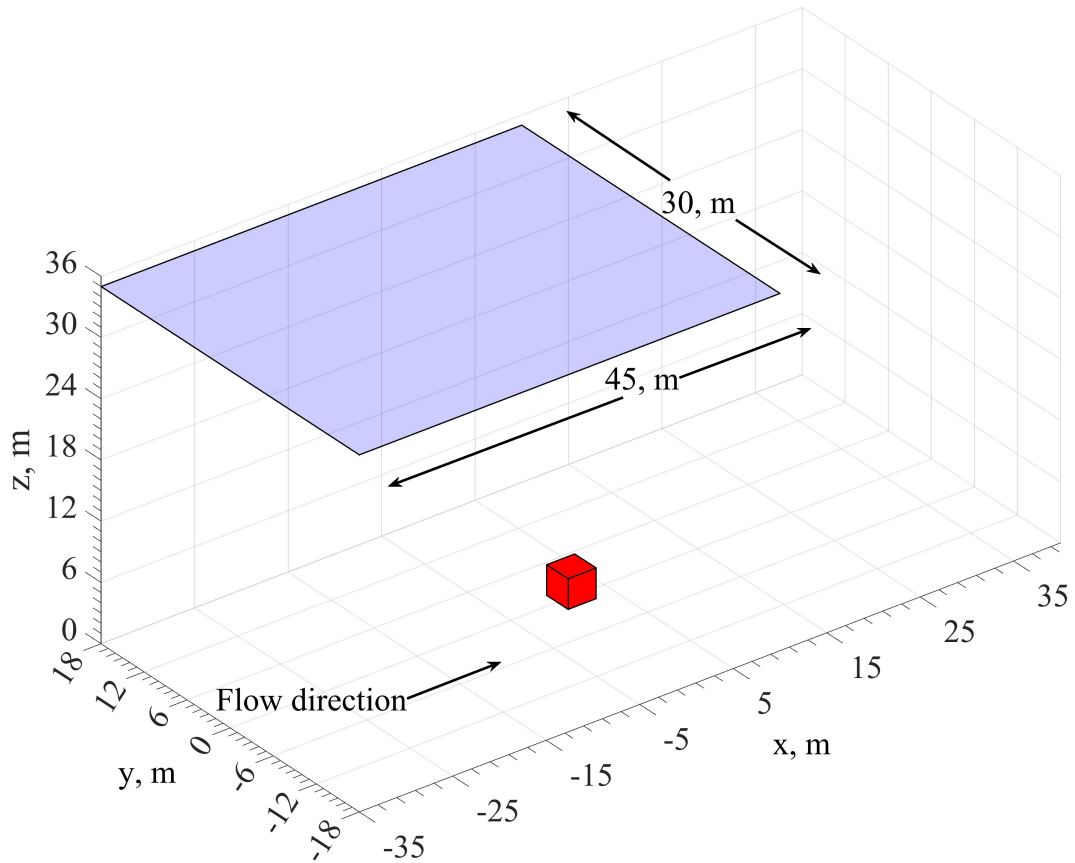


**Figure 3.2:** Computational configuration in the firebrand deposition study with a block  $3 \times 3 \times 3$  m. The horizontal plane located at  $z = 35$  m is where the firebrands are released from.

velocity was specified by a power law with an exponent of 0.18 with a velocity of 6 m/s at a reference height  $h = 3$  m which resulted in  $Re_h = 1 \times 10^6$ . The choice of the wind speed values was guided by moderate speeds of winds reported for WUI fires [67, 37]. The turbulent intensity at the inlet was set to 20%. This inlet boundary condition is an approximate representation of a neutrally stable ASL. The modeling approaches such as SGS turbulent closure model and the near-wall

models are the same described in §3.2.2. The dimension and velocity scales are selected here to be relevant to WUI.

The firebrands were released every second from positions with coordinates randomly selected from a uniform distribution on a horizontal plane passing  $z = 35$  m, as shown in fig. 3.2, after the flow reached a statistically stationary state. This approach of releasing firebrands might be considered as a simplified representation of ember/firebrand showers. At the release points, firebrands had a zero velocity with the orientation of  $60^\circ$  with respect to the vertical axis and the initial firebrand temperature  $T_p = 773$  K. The initial firebrand mass density was  $570 \text{ kg/m}^3$ , and the firebrand diameter and length of 3 mm and 40 mm [38], respectively. Considering the flow and firebrand release conditions here, the simulations here will be relevant to long range spotting. Random initial distribution of firebrands is to account for the uncertainty of the firebrand release point.

### 3.3 Results and Discussion

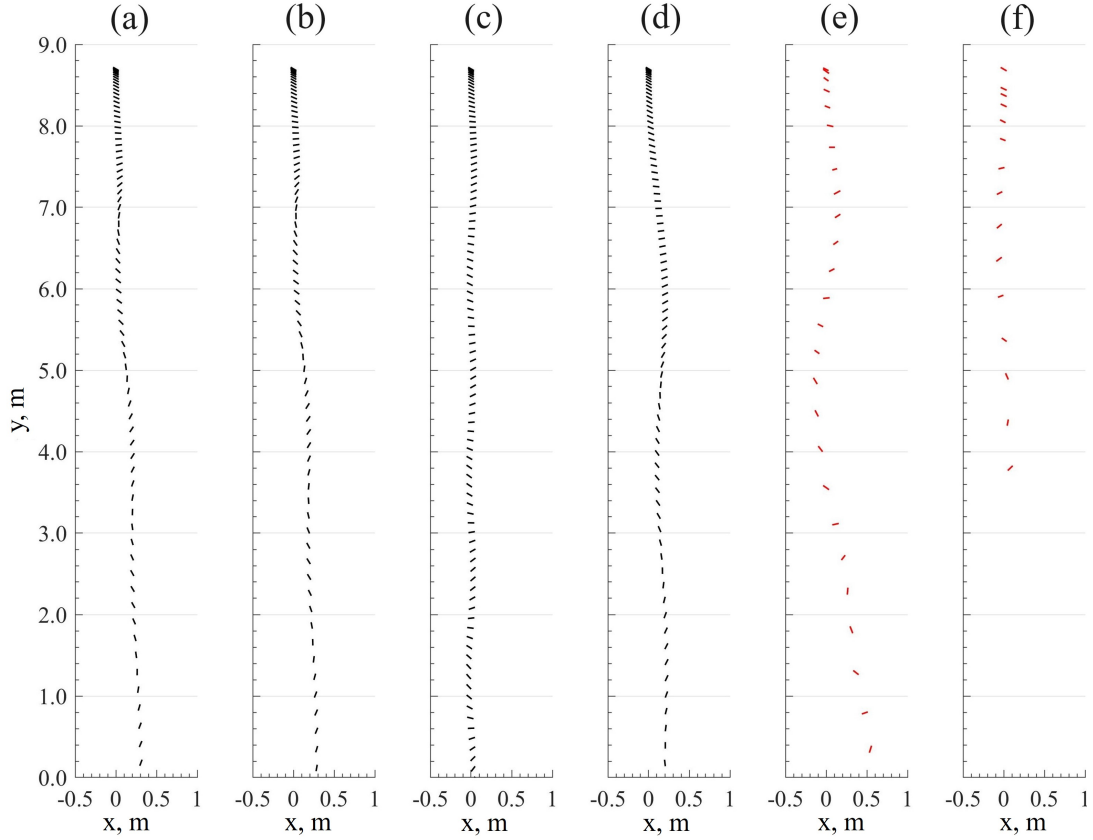
#### 3.3.1 Firebrand Release in No-wind Condition

Table 3.2 tabulates the landing times calculated in the current study using various  $x_{cp}$  formulas (seen in table 3.1) and compares them against those obtained by previous simulations and experiments [57]. Corresponding trajectories of the firebrand from release to landing are shown in figure 3.3. Both table and figure suggest the significance of the  $x_{cp}$  formula in the firebrand landing time and trajectory. A notable difference was seen in the landing times between the previous experiments (panel f) and numerical simulation (panel e) by Oliveira

**Table 3.2:** Landing time of a cylindrical firebrand released in a still air in the previous experiment and simulation [57], and present simulations using different formulas for  $x_{cp}/l$  [61, 41, 66, 86].

	Landing time, s	Reference
(a)	1.5312 (present study)	Rayleigh [61]
(b)	1.5246 (present study)	Marchildon <i>et al.</i> [41]
(c)	1.9397 (present study)	Rosendahl [66]
(d)	1.6564 (present study)	Yin <i>et al.</i> [86]
(e)	2.06 (previous experiment)	Oliveira <i>et al.</i> [57]
(f)	$1.70 \pm 0.05$ (previous simulation)	Oliveira <i>et al.</i> [57]

*et al.* [57]. They attributed this difference to the numerical simulations under predicting the amplitudes of the trajectory oscillation (as seen in fig. 3.3 panels e and f). On the other hand as seen from fig. 3.3 the amplitude of the trajectory oscillation obtained in the current simulations, regardless of the  $x_{cp}$  formulation used, was significantly more consistent with the experimental data of Oliveira *et al.* [57]. Consequently, the landing times obtained from the current simulation were roughly less than 14% closer to the previous experiments [57] rather than 20% seen in the previous numerical simulations. Using  $x_{cp}$  calculated from the formulation provided by Rosendahl [66] (panel c) the amplitude of oscillation is lower causing the landing time being the largest amongst the current simulation. Whereas, using  $x_{cp}$  formulation provided by Yin *et al.* [86] (panel d) the amplitude of oscillation is greater than panel c but closer to the previous experiment



**Figure 3.3:** Trajectory of a cylindrical particle released in still air condition in the present simulations using different formulation of  $x_{cp}$  [61, 41, 66, 86] and previous numerical and experimental data [57].

(panel f), resulting in the landing time being closer to the experiments. However, the firebrand's initial movement in the  $x$  direction in panel d is greater than seen in the previous experiments. Using formulation for  $x_{cp}$  by Rayleigh [61] (panel a) and Marchildon *et al.* [41] (panel b) yields a slightly great amplitude of oscillation compared to experiments but better captures the firebrand's initial movement in

$x$  direction. Resulting in the trajectory resembling closest to the experiments with near identical landing times for both formulation within 10% of the experiments.

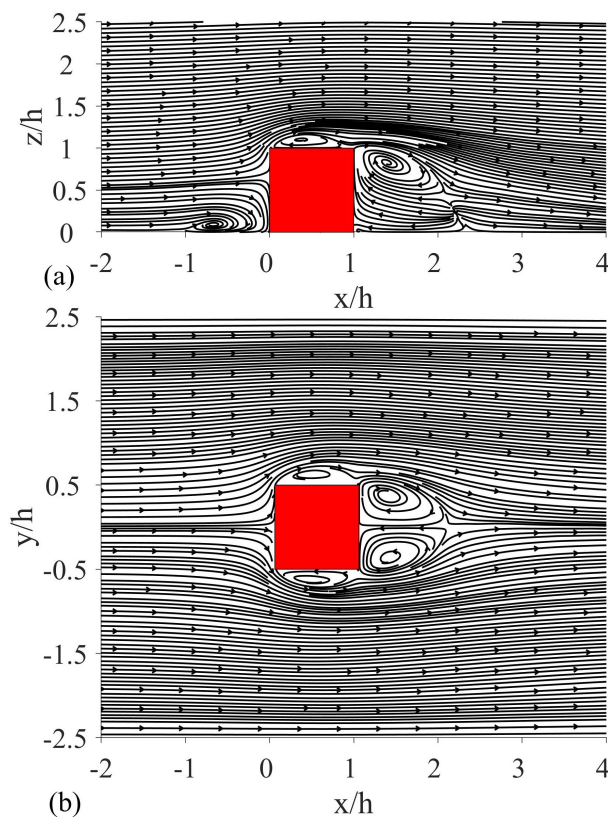
### 3.3.2 Flow Validation Over a Single Block

Figure 3.4 shows the mean velocity streamlines at a slice  $y = 0$  and  $z = 0.5h$  obtained from present simulations. This figure shows the key flow structures around the block, viz. the center of the horseshoe vortex, the flow separation and reattachment on the top and lateral faces, flow reattachment on the leeward side of the block, the two counter rotating re-circulation region and the stagnation point of the front face of the block. Table 3.3 compares the locations of these points of

**Table 3.3:** The locations of the center of the horseshoe vortex (HVC) ( $x_{\text{HVC}}, y_{\text{HVC}}$ ); the stagnation point on the windward face  $y_{\text{stag}}$ ; the flow reattachment point on the top face  $x_{\text{top}}$  and the flow reattachment point on the leeward side of the block  $x_{\text{lee}}$  in previous [34] and present simulations.

	$(x_{\text{HVC}}, y_{\text{HVC}})$	$y_{\text{stag}}$	$x_{\text{top}}$	$x_{\text{lee}}$
Previous simulation [34]	$(-0.50h, 0.10h)$	$0.73h$	$0.75h$	$1.56h$
Present simulation	$(-0.74h, 0.08h)$	$0.66h$	$0.83h$	$1.51h$

interest obtained in the current study with those obtained in the simulation of Lim *et al.* [34]. The center of the horseshoe vortex [70] obtained here is further away from the windward face of the block when compared to the previous simulation [34]. On the other hand, the locations of the stagnation point on the windward face of the block, the reattachment length on the top face of the block and the



**Figure 3.4:** Mean velocity streamlines at planes (a)  $y = 0$ ; and (b)  $z = 0.5h$  of the flow over  $8 \times 8 \times 8$  cm block at  $Re_h = 2 \times 10^4$  in the flow model validation study.

reattachment length on the leeward side of the block obtained here closely match those in the simulation of Lim *et al.* [34], as seen in table 3.3.

Figure 3.5 shows the pressure coefficient  $C_p$  on the axial (*i.e.*,  $y/h = 0$ ) and transverse (*i.e.*,  $x/h = 0.5$ ) center-lines on the faces of the block as indicated in fig. 3.1. As seen in fig. 3.5, the pressure coefficient calculated here for the top face of the block compares well against the experimental and simulation data of Lim *et al.* [34]. The agreement between the current simulation and the previous works for this coefficient is reasonable for the rest of the faces. The experimental

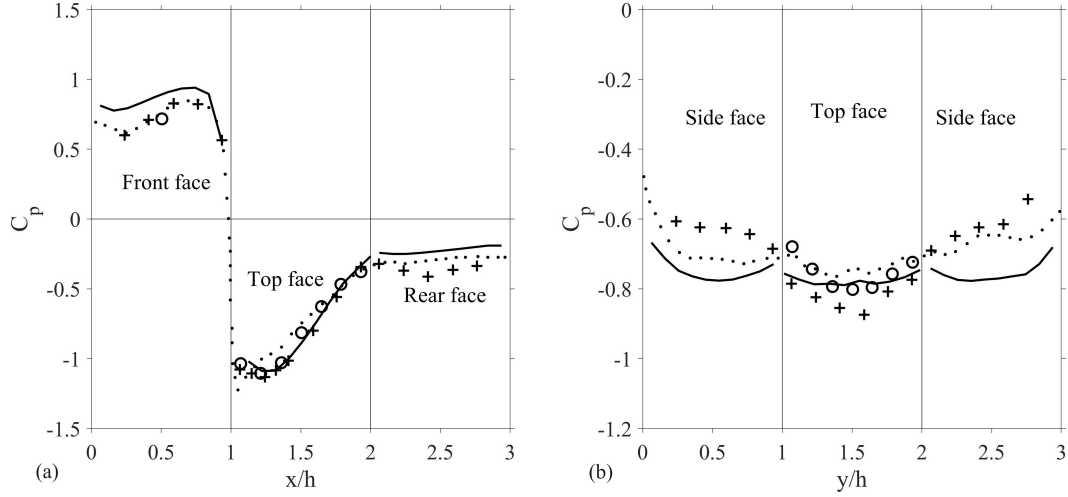


**Figure 3.5:** Pressure coefficient on the surface of the block on (a) the axial centerline where  $y/h = 0$ ; and (b) the transverse centerline where  $x/h = 0.5$  in previous experiments [34], ( $\circ$ ) and Richards *et al.* [63] ( $+$ ), previous simulation [34] (dotted line) and the present simulation (solid line).

data of Richards *et al.* [63] is also shown here for a comparison albeit they were obtained for a different Reynolds number of  $4.1 \times 10^6$ . From fig. 3.5 it can be seen that,  $C_p$  is positive only on the front face with a max value corresponding to the location of stagnation point. On the contrary, the rest of the faces have a negative value of  $C_p$ . This is a result of the flow separation and the counter rotating re-circulation regions seen on the top, lateral and rear faces in fig. 3.4. The largest negative  $C_p$  occurs on the top face right after the leading edge which is associated with the flow separation at this location. This is followed by pressure recovery which corresponds to the flow reattachment.

In figure 3.6, the mean components of velocity in the streamwise and vertical directions are plotted versus  $z$  on the axial centerline of the top face of the

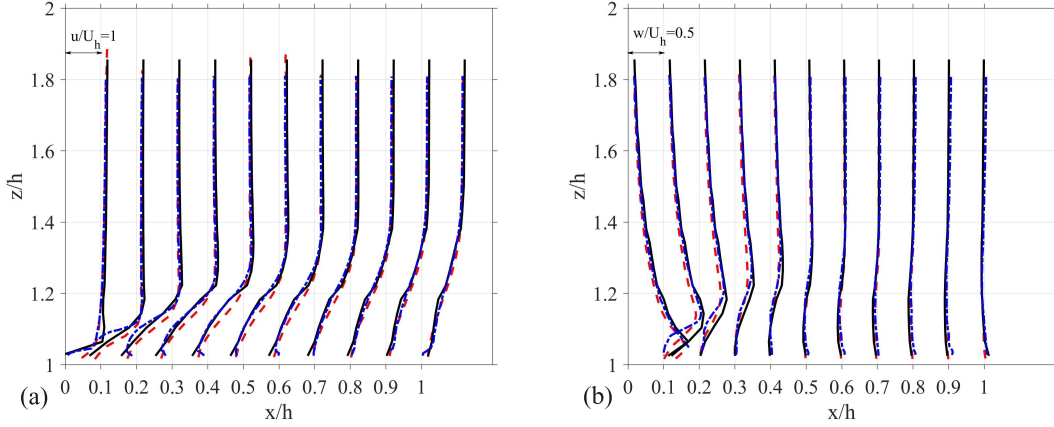


**Figure 3.6:** The mean velocity components in the (a) streamwise; and (b) vertical directions over the top face of the block in previous experiment (blue dashed-dotted line), and simulation (red dashed line) of Lim *et al.* [34] and the present simulation (solid line).

block at various  $x$ 's. The agreement between the current simulation and the previous experiment and simulation [34] is good. The change of the velocity profile in the  $x$  direction is attributed to the flow separation and reattachment seen on the top face. Fig. 3.7 shows the profiles of the root mean square (rms) of the streamwise and vertical component of velocity as well as the Reynolds shear stress at various  $x$ 's on the axial center-line of the top face of the block. As seen in fig. 3.7(a,b), the simulation substantially over-predicts the rms values obtained in the previous experiments and the simulation [34]. On the other hand, the Reynolds shear stress in the simulation is in reasonably good agreement with the previous experimental and simulation data.

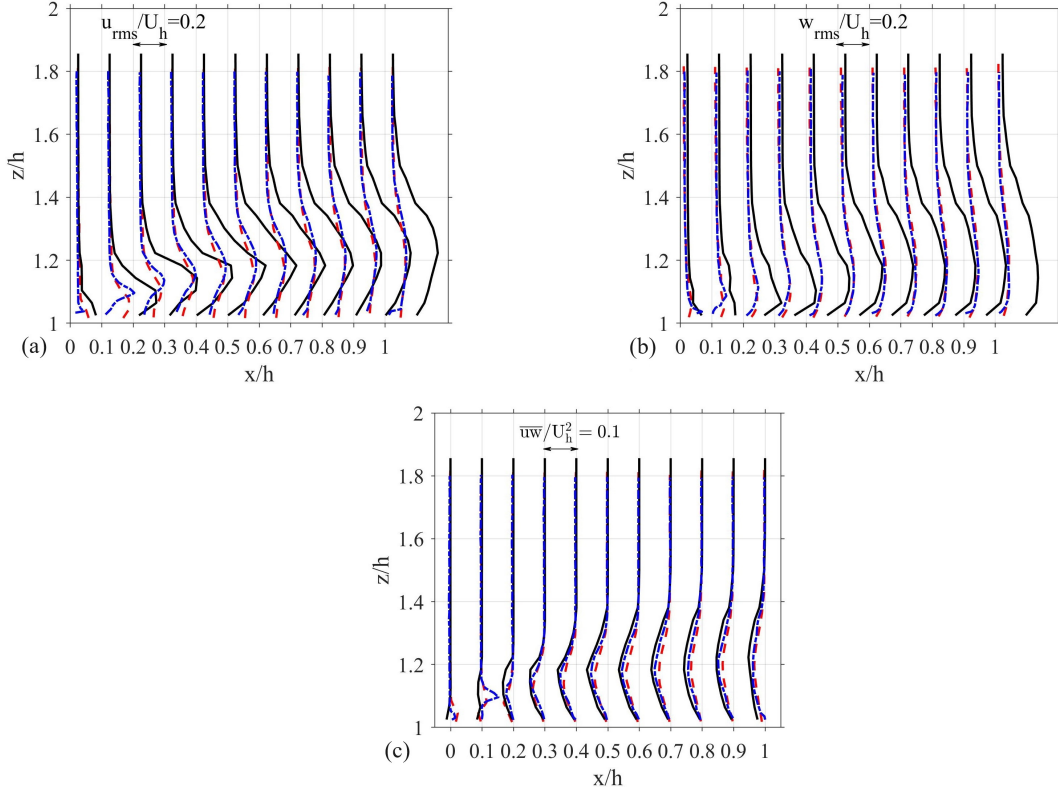


**Figure 3.7:** The rms of velocity components in the (a) streamwise and (b) vertical directions; and (c) Reynolds shear stress  $\overline{uw}$  over the top face of the blocks in previous experiment (blue dashed-dotted line) and simulation (red dashed line) of Lim *et al.* [34], and the present simulation (solid line).

### 3.3.3 Firebrand Deposition in the Flow Over a Single Block

Figure 3.8 shows the mean velocity streamlines superimposed on the contour plots of mean velocity magnitude on the plane  $y = 0$  for varying block dimension (panels b-h) and no block (panel a). The streamline features in presence of a block, overall resemble the ones seen in fig. 3.4(a), which is for a low Reynolds number. However, the details of these features are different for various

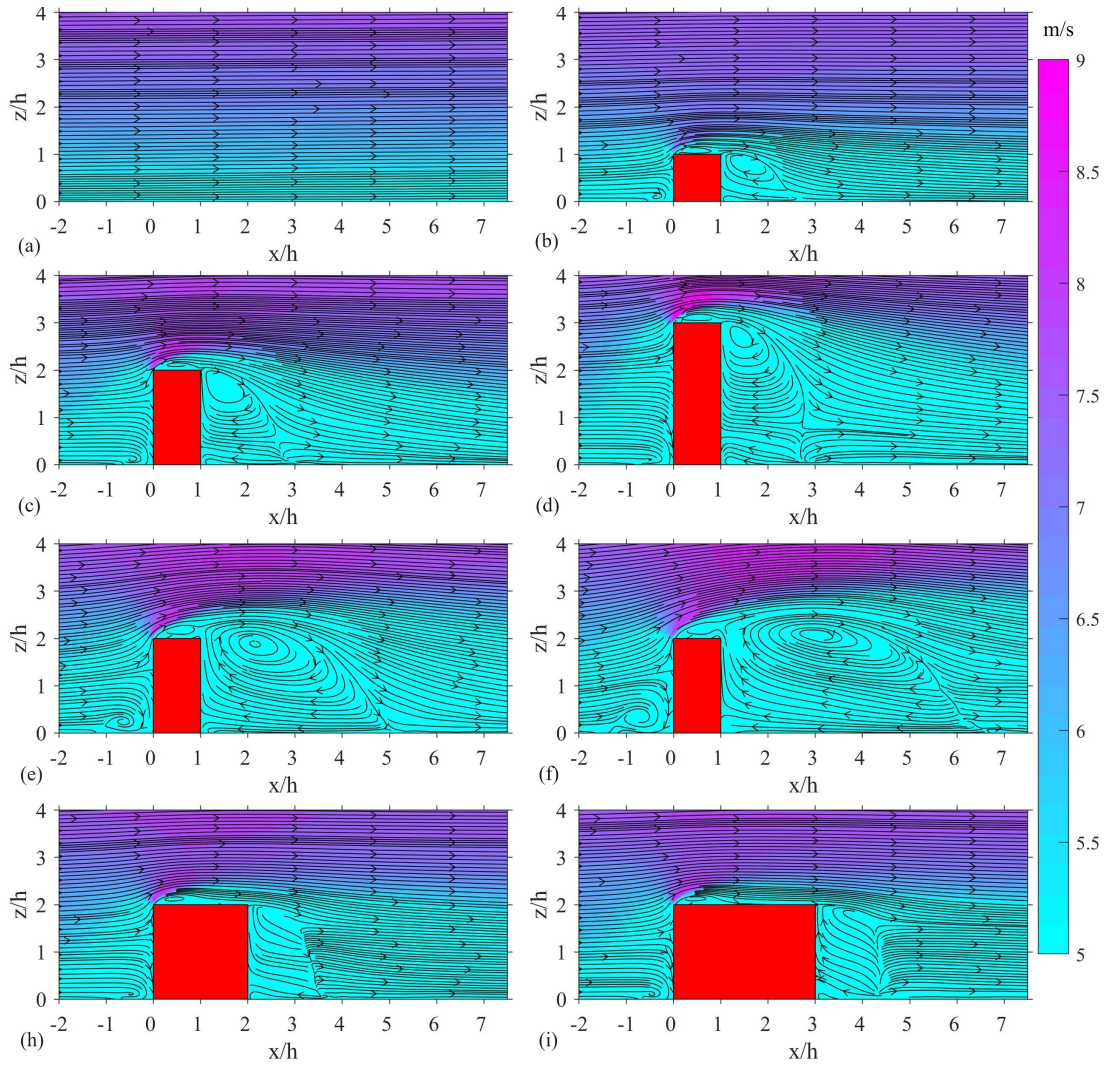


**Figure 3.8:** Mean velocity streamlines superimposed on the contour plots of mean velocity magnitude at slice  $y = 0$  (a) with no block; and with block having dimensions of (b)  $L = W = H = 3$  m; (c)  $L = W = 3$  m,  $H = 6$  m; (d)  $L = W = 3$  m,  $H = 9$  m; (e)  $L = 3$  m,  $W = H = 6$  m; (f)  $L = 3$  m,  $W = 9$  m,  $H = 6$  m; (g)  $L = H = 6$  m,  $W = 3$  m; (h)  $L = 9$  m,  $W = 3$  m,  $H = 6$  m.

displayed cases. Fig. 3.8 (panels c,e,f) the blocks with fixed lengths and heights but varying widths, the horseshoe vortex and the length of the wake on the leeward side of the block increases in size with the increase of the block's width. The

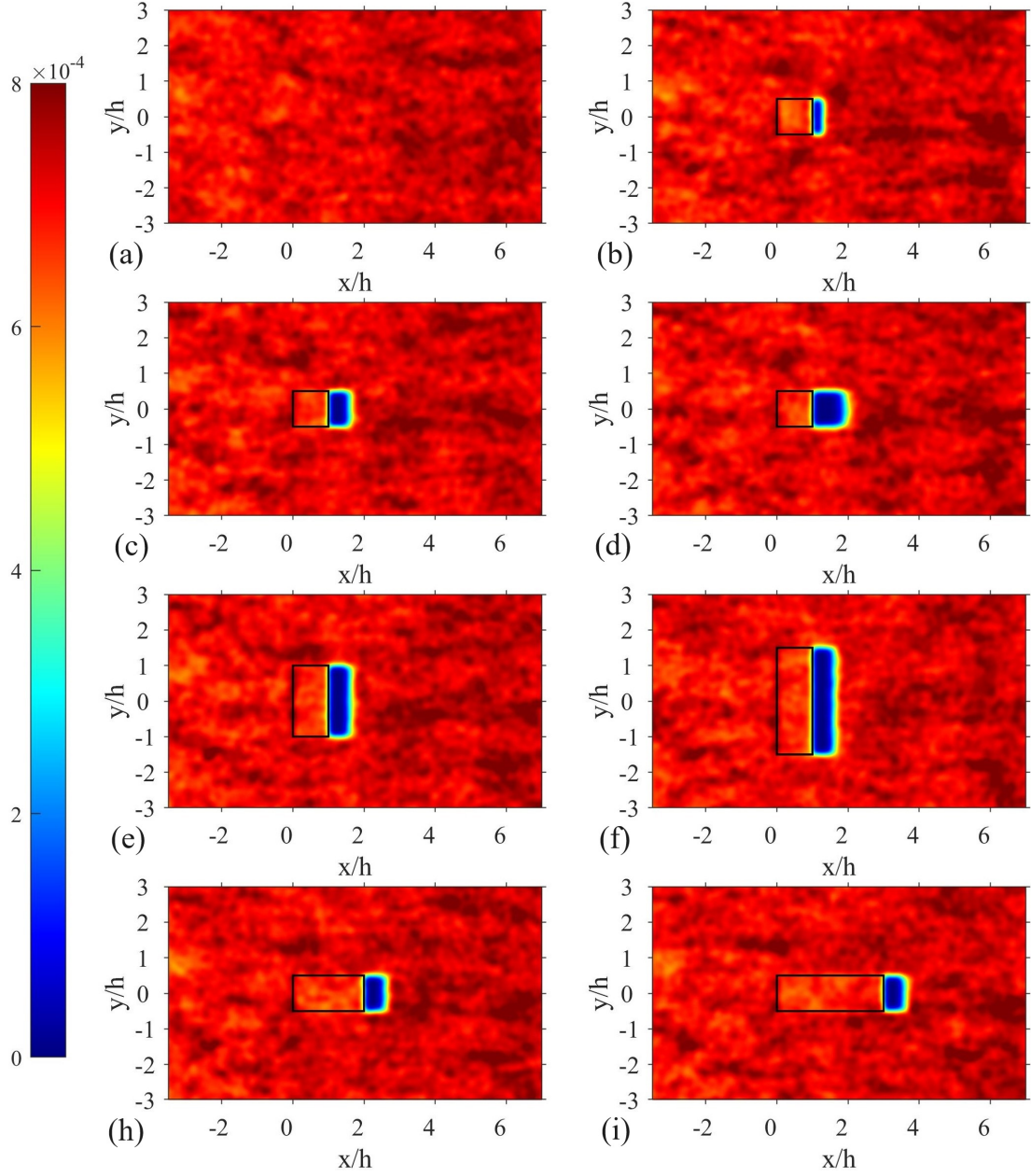
flow seems to accelerate moving over the leading edge of the block resulting in a higher velocity magnitude at this location compared to the immediate surrounding. The velocity magnitude of the flow near the leading edge is higher for taller blocks, as seen in fig. 3.8 (panels b,c,d). Fig. 3.8 (panels c,g,h) the increase in the length of the block slightly decreases the length of the wake behind the block.

To quantify the spatial distribution of the deposited firebrands, a criterion proposed by Anand *et al.* [5] based on normalized number density (NND) defined by:

$$\hat{f}(x, y) = \frac{1}{nB^2} \sum_{i=1}^n \kappa \left( \frac{x - x_i}{B}, \frac{y - y_i}{B} \right), \quad (3.1)$$

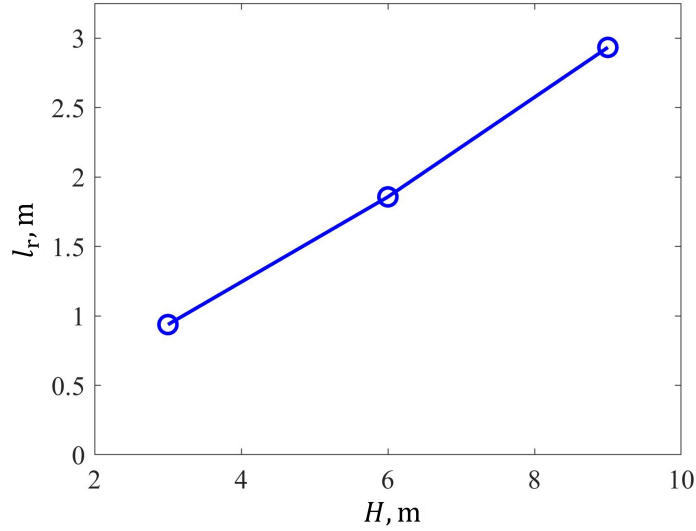
was used. Here,  $\hat{f}$  ( $1/m^2$ ) is the probability density function normalized by the total number of particles  $n$  deposited over an area of  $B^2$  where  $B$  is the bandwidth set to 0.25 m. Thus, the number density is equivalent to the number of firebrands deposited per unit area. In the current simulations the number of firebrands deposited  $n \sim 3.8 \times 10^6$ .  $x_i$  and  $y_i$  are the landing coordinates of the  $i^{th}$  firebrand. A Gaussian function was selected as the kernel function [43] here. Once a firebrand was deposited on a surface, its position and temperature were saved and it was eliminated from the simulation.

Figure 3.9 shows a top view of the contour plots of NND of the deposited firebrands for cases displayed in fig. 3.8. As seen from this figure, the NND on the ground around the blocks is largely similar to the NND seen in the case without the blocks. Apart from this there appears to be a region of very low NND on the leeward side in panels with blocks. Examining the scattered deposited particle data revealed that no firebrands were deposited on this region. This region is



**Figure 3.9:** Contour plots of normalized number density of the deposited firebrands on the ground (a) with no block; top face and the ground around single blocks with (b)  $L = W = H = 3$  m; (c)  $L = W = 3$  m,  $H = 6$  m; (d)  $L = W = 3$  m,  $H = 9$  m; (e)  $L = 3$  m,  $W = H = 6$  m; (f)  $L = 3$  m,  $W = 9$  m,  $H = 6$  m; (g)  $L = H = 6$  m,  $W = 3$  m; (h)  $L = 9$  m,  $W = 3$  m,  $H = 6$  m.

hereby referred to as the safe zone. The safe zone is approximately shaped like a rectangle with a length  $l_r$  and a width  $w_r$  (in the spanwise direction), which is almost identical to the width of the block  $W$ . The length  $l_r$  is calculated as the perpendicular distance from the leeward face of the block to where the NND is  $3.85 \times 10^{-4}$ . Fig. 3.10 displays  $l_r$  versus  $H$  and indicates that for every three



**Figure 3.10:** Length of the safe zone versus the height of the block  $H$  where  $L = W = 3$  m.

meter increase of the block height, the safe zone length increases roughly by a meter. The change in width  $W$  or length  $L$  of the block barely affected the length of the safe zone. The direct proportionality of the safe zone length and width to the height and width of the block implies that the block has a shielding effect on the leeward side. To ensure the grid size had no impact on the NND and the safe zone length  $l_r$ , a simulation with twice the fidelity in each direction was run

with a block with  $L = W = H = 3$  m. The higher fidelity simulations show no noticeable change in NND and found that  $l_r$  decreased less than 6%.

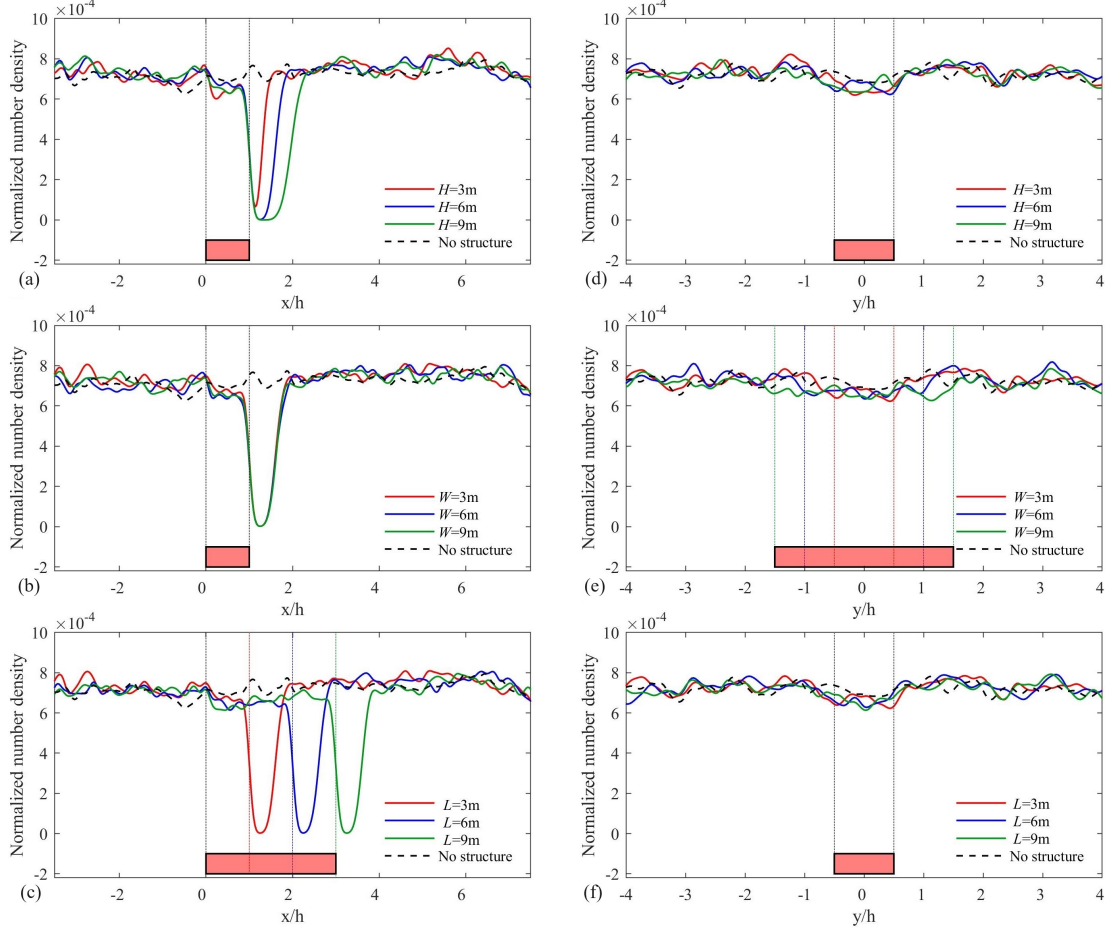


**Figure 3.11:** Normalized number density of deposited firebrands vs  $x/h$  at  $y = 0$  on the left panels and vs  $y/h$  at  $x = 0.5h$  on the right panels for (a,d)  $L = W = 3$  m; (b,e)  $H = 6$  m and  $L = 3$  m; and (c,f)  $H = 6$  m and  $W = 3$  m.

Figure 3.11 (a,b,c) shows the NND of deposited firebrands vs  $x$  at  $y = 0$  and fig. 3.11(d,e,f) plots it against  $y$  at  $x = 0$  for various blocks sizes and the case with no block. Seen in fig. 3.11 (a,b,c), are distinct troughs in cases with a block, which correspond to the safe zones. These panels also show that NND

overall decreases from the leading to the trailing edge on top of the blocks. This is speculated to be associated with the flow separation that occurs on top faces of the block, which is visible in fig. 3.8. For the blocks with longer lengths, the flow separated by the leading edge reattaches, as seen in fig. 3.8 (g,h). This reattachment gives rise to the local peaks of NND on the top face of the block as seen in fig. 3.11(c). It is speculated that some firebrands gain momentum from the accelerated flow above the leading edge of the blocks (seen in figure 3.8) and deposit closer to it's trailing edge. The curves of the cases with blocks in fig. 3.11(b,d,f) shows that the NND on top faces overall has relatively lower values compared to the neighboring areas on the ground. Fig. 3.11(a,b) shows that an increase in the height of the block results in a slightly higher NND on the top face of the block.

Table 3.4 shows the number of firebrands deposited and their temperatures on the top, front and lateral faces of the block. In none of the cases, a firebrand was deposited on the back face of the block. This table shows that in the cases with varying height but the same width and length, the number of firebrands deposited on the top face and their average temperature increase with an increasing height. The higher temperature is a result of the firebrands travelling a shorter path to reach the top face of the taller blocks. The shorter path traveled by the firebrands mean the less time to loss heat to the environment thus leading to hotter temperatures. Fig. 3.12 shows the exact location and temperature of each deposited firebrand on all faces of the block ( $L = 3$  m,  $H = 6$  m and  $W = 3$  m) except for the leeward face. As noted earlier, the leeward face did not receive any

**Table 3.4:** Number and average temperature (K) of firebrands deposited on the top, windward and lateral faces of the block.

Cases	Top Face		Windward Face		Lateral Faces	
	No.	Avg. Temp.	No.	Avg. Temp.	No.	Avg. Temp.
$3 \times 3 \times 3$ m	22949	424.92	6820	418.77	244	419.17
$3 \times 3 \times 6$ m	23428	436.24	14112	424.06	428	424.22
$3 \times 3 \times 9$ m	23670	448.82	21959	430.33	494	435.97
$3 \times 6 \times 6$ m	46927	435.49	28425	423.69	351	426.71
$3 \times 9 \times 6$ m	70412	435.06	43367	423.34	443	424.94
$6 \times 3 \times 6$ m	46737	436.19	14154	424.15	1006	425.17
$9 \times 3 \times 6$ m	71267	436.17	14192	424.09	1516	424.73

firebrands in any of the cases. As evident in this figure, the higher the firebrands deposit on the block the higher their temperature at the time of deposition. Also, evident from this figure is a roughly triangular region with no firebrands on either lateral face of the block is noticeable.

### 3.4 Chapter Summary

A firebrand model was developed and used to simulate cylindrical firebrand motion and burning through the FDS framework. This model was validated against the previous experimental and computational data [57] for a firebrand

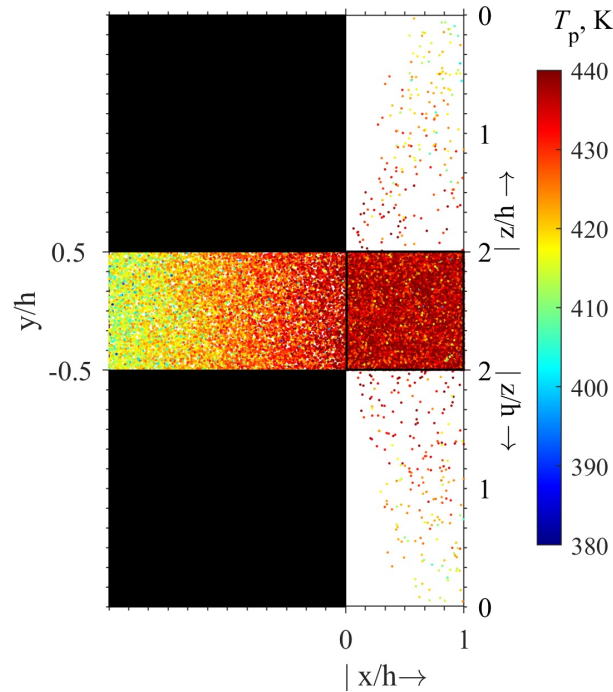


**Figure 3.12:** Location and temperature of the firebrands deposited on the faces of the block with  $L = W = 3$  m and  $H = 6$  m. The individual dots indicate the position and the color indicates of the firebrand at the time of deposition on the block faces. The top face is highlighted by a black square, whereas, the front face is between the two solid black squares. The lateral faces are indicated by the two remaining rectangles.

falling in a no-wind condition. The current model showed better agreement with the experimental data than the previous computational model [34].

In addition, the previous experimental and CFD data [34] for a flow over a mounted  $h = 0.08$  m height block in a wind tunnel was used to validate FDS for simulation of flows over obstacles. The pressure coefficients in the simulation was in relatively good agreement with the experimental data. The mean velocity components in the streamwise and vertical directions as well as the Reynolds shear stress in the simulation closely matched the experimental data. On the

other hand, the simulation substantially over-predicted the measured rms of the velocity components in the streamwise and vertical directions.

The developed firebrand model then used with FDS to simulate the deposition of firebrands carried by a flow over a rectangular cubic block, as a representative of a single simplified WUI structure in an open domain. A parametric study was conducted where heights, widths and lengths were varied from 3 to 9 m. It revealed an area on the leeward side of the block on the ground where no firebrands were deposited. This area was referred to as the safe zone. The width of the zone was the same as the width of the block (the dimension of the block in the spanwise direction). The length of this zone in the streamwise direction was proportional to the height of the block. Also a triangular region with no firebrands being deposited was identified on the lateral faces of the block towards the leading edge. No firebrand was deposited on the leeward face of the block regardless of its size. The NND on the top face of the block increases slightly with its height. For blocks with longer lengths, the NND dropped near the leading edge and rose back again towards its trailing edge. This effect was attributed to the flow accelerating above the leading edge of the block thus imparting extra momentum onto the firebrands and carrying them farther away.

## Chapter 4. Cylindrical Firebrands Deposition on Three Neighboring Blocks

### 4.1 Introduction

First, modeling of the flow over three blocks arranged in tandem and parallel was validated against previous experimental and numerical data. This exercise also included further validation of single block flow modeling as relevant to this study. The computational setup and results for these validation studies are discussed in §4.2.1 and §4.3.1, respectively. Then, firebrand deposition over three cubic blocks, three meters tall, in tandem and parallel arrangements was simulated. Details on the computational configuration and the results pertaining this study are discussed in §4.2.2 and §4.3.2, respectively.

### 4.2 Computational Setups

#### 4.2.1 Wind Tunnel Scale Flow

To validate FDS in representing flows over ground mounted block simulations were conducted in computational setups resembling previous work by Lim and Ohba [33]. This included single and multiple wall mounted cubic blocks in tandem and parallel arrangements with height  $h = 0.15$  m. The Reynolds number

was  $Re_h = U_h h / \nu = 46,000$ , where  $U_h$  represents the mean inlet velocity at  $z = h$ . It is noted that here  $h = H$ , where  $H$  indicates the block height as introduced in the previous chapter. Consistent with Lim and Ohba [33]’s computations,

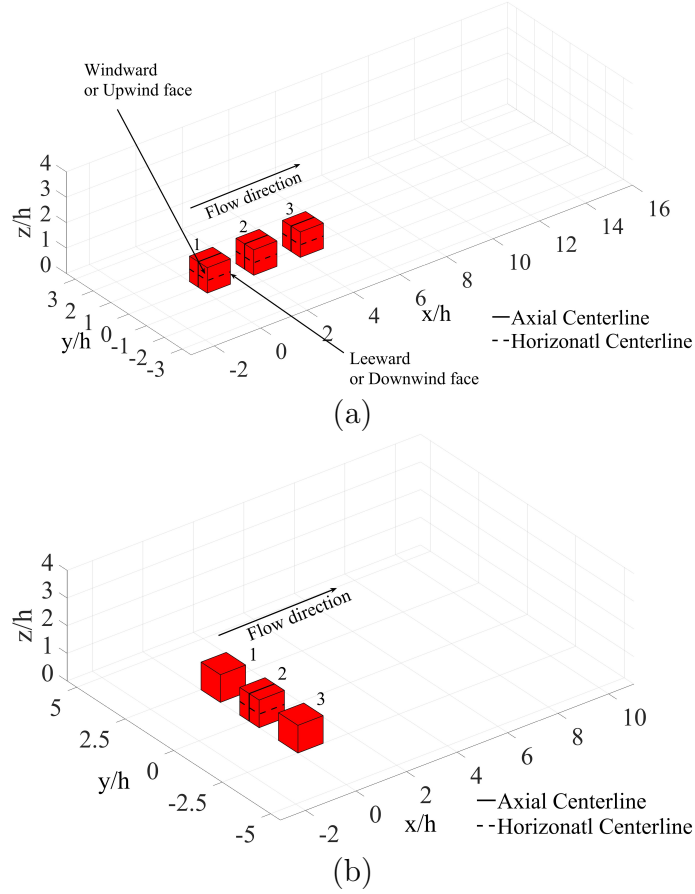


**Figure 4.1:** Computational domain for the wind tunnel flow over blocks in (a) tandem arrangement; and (b) parallel arrangements. Single block simulations were conducted in the tandem arrangement configuration including only the leading block.

the dimensions of the computational domains in the single block, tandem and parallel arrangements were set to be  $2.1 \times 1.05 \times 0.6$  m (length  $\times$  width  $\times$  height),  $2.85 \times 1.05 \times 0.6$  m and  $2.1 \times 1.65 \times 0.6$  m, respectively, as shown in figure 4.1.

The locations of the blocks are also shown in this figure. Lim and Obha [33] used a grid stretched in the direction normal to all the walls (including the cube faces) with a grid size of 0.00375 m ( $0.025h$ ), as the finest grid size, next to the wall and a total number of grid points of  $\sim 1.5 \times 10^6$ . Because the use of a stretched grid in multiple direction is not possible with FDS, a uniform grid was used in the current simulation with a grid size of  $5 \times 5 \times 5$  mm and a total grid points of  $\sim 20 \times 10^6$ . A power law profile was set for the mean velocity as the inlet boundary condition with a power law exponent of 0.14 that produced  $U_h = 4.2$  m/s equivalent to  $Re_h = 46,000$ . Periodic boundary conditions were set on the lateral boundaries, a symmetric boundary condition was set on the top boundary and an open condition was applied on the outflow boundary. The boundary conditions were consistent with Lim and Ohba [33]’s boundary conditions. Turbulence intensity of 20% was introduced at the inlet using a synthetic eddy method (SEM) [25, 37].

#### 4.2.2 Field-Scale Flows with Firebrands

The computational domain used in the firebrand deposition study included multiple cubic blocks of height  $h = 3$  m in tandem and parallel arrangements as shown in fig. 4.2. As shown in this figure, the three blocks were numbered by T1, T2 and T3 the tandem arrangement and A1, A2 and A3 the parallel arrangement. To investigate the sensitively of the results to the wind speed and the separation distance, nine simulations were conducted with three values for  $S/h = 0.3, 0.5$  and 1 and three values for  $U_h = 6, 9$  and 12 m/s for each of the parallel and tandem arrangements of the blocks as tabulated on Table 4.1. These were corresponding

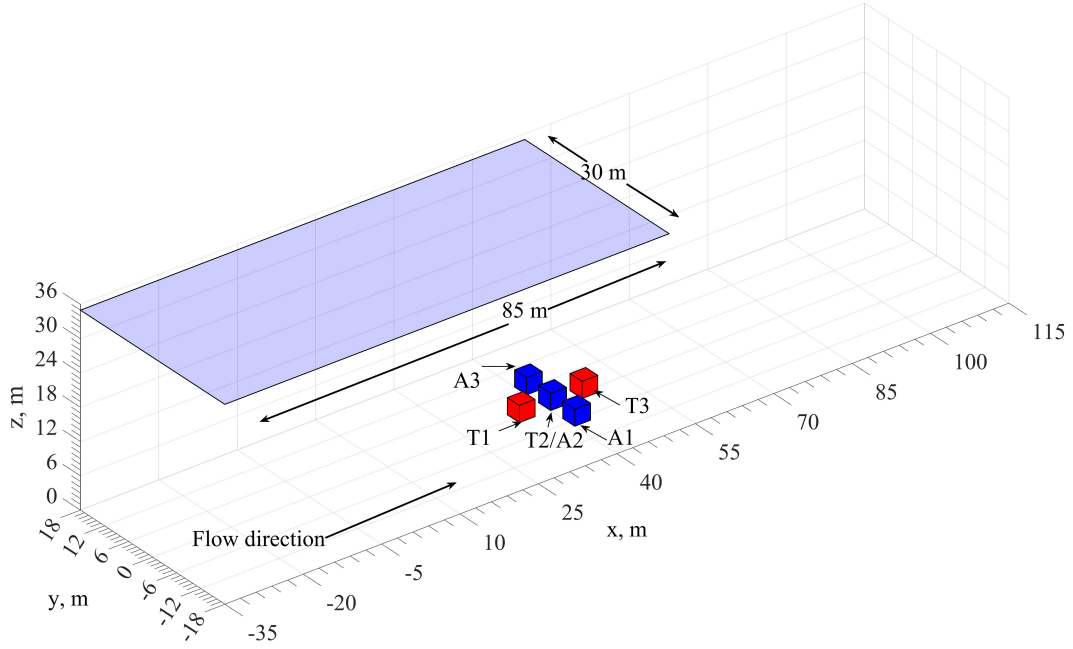


**Figure 4.2:** Computational configurations in the field scale simulations of firebrand deposition tandem (T) and parallel (A) arrangements for  $S = h$ .

to  $Re_h = 1.2 \times 10^6, 1.8 \times 10^6$  and  $2.4 \times 10^6$ , respectively. The choice of the wind speed values was guided by moderate speeds of winds reported for WUI fires to be in the range of 6 to 18 m/s [67, 37]. The computational domain size was set to  $150 \times 36 \times 36$  m in the  $x, y$  and  $z$  directions, respectively. A uniform grid with a resolution of  $500 \times 180 \times 180$  was used in the  $x, y$  and  $z$  directions, respectively. This corresponds to a dimensionless grid size of  $\Delta = h/10$ .

**Table 4.1:** Parameters varied in the field scale simulations with firebrand deposition.

$S/h$	0.3	0.5	1
$U_h$ (m/s)	6	9	12

The inlet flow mean velocity was set to follow a power law with an exponent of 0.18 and produce the reference velocity  $U_h$  at  $z = h$ . This inlet boundary condition is an approximate representation of a neutrally stable atmospheric surface layer (ASL). To model the fluctuations of the inlet velocity, the synthetic eddy method (SEM) [25, 45, 46] was used with the turbulence intensity of 20%. The lateral and top boundaries were set to be free slip and the outlet boundary was open.

The firebrands were released every second from different points with the release coordinates randomly sampled with a uniform distribution from a horizontal plane passing  $z = 35$  m, as shown in fig. 4.2, after the flow had reached a statistically stationary state. Firebrands were released with a zero velocity, an orientation angle of  $90^\circ$  with respect to the vertical axis and a firebrand temperature  $T_p = 773$  K. The firebrand mass density was  $570 \text{ kg/m}^3$  with firebrand diameter and length of 3 mm and 40 mm, respectively [38].

## 4.3 Results and Discussion

### 4.3.1 Wind Tunnel Scale Flow

Figure 4.3(a,b) show the pressure coefficient  $C_p$  on the axial and horizontal centerlines. These are the intersections of the axial plane  $y/h = 0$  and the horizontal plane  $z/h = 0.5$  with the block faces as shown in fig. 4.1 by solid and dashed lines, respectively. The mean velocity in the streamwise direction at  $y/h = 0$  on the top face of the block and the contour plot of the same quantity at  $y/h = 0$  is also displayed in panels c and d in fig. 4.3, respectively. The

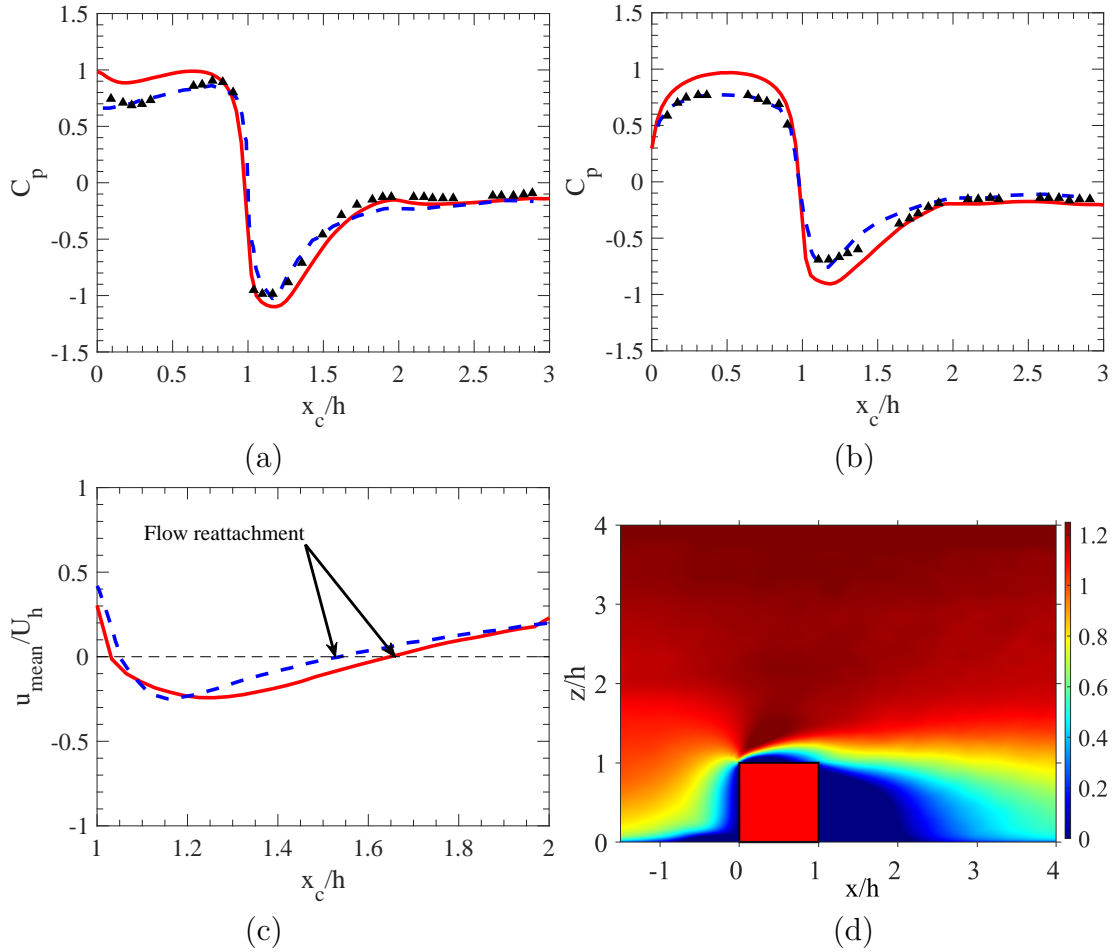


**Figure 4.3:** Single block results in the wind tunnel scale flow; (a) pressure coefficient at the axial centerline  $y/h = 0$  on the windward face ( $0 \leq x_c/h \leq 1$ ), the top face ( $1 \leq x_c/h \leq 2$ ) and the leeward face ( $2 \leq x_c/h \leq 3$ ), and (b) pressure coefficient at the horizontal centerline on the windward face ( $0 \leq x_c/h \leq 1$ ), the lateral face ( $1 \leq x_c/h \leq 2$ ) and the leeward face ( $2 \leq x_c/h \leq 3$ ); and (c) mean velocity in the stream-wise direction on the top face at the axial centerline for previous experiments ( $\blacktriangle$ ) and simulations (---) by Lim and Ohba [33], and the current simulations (—); along with (d) contour plot of the mean streamwise velocity non-dimensionalized by  $U_h$  on  $y/h = 0$ .

trend in pressure coefficient seen in fig. 4.3(a) is similar to §3.3.2. The maximum pressure coefficient occurs on the windward face of the block with a sharp drop over the leading edges of the block, as seen in fig. 4.3(a,b). This is followed by a negative mean velocity in the streamwise direction over the top face of the block closer to the leading edge, as could be seen in fig. 4.3(c,d). The rapid pressure drop and the negative velocity are due to the sharp leading edge of the block diverting the flow away and causing a low pressure region and resulting in flow separation and re-circulation at the leading edge. A substantial pressure recovery and a positive mean velocity in the streamwise direction are seen over the top face closer to the trailing edge, which is associated with the flow reattachment on the top face. Compared to the previous experimental and modeling data, the pressure coefficient on the windward face of the block is  $\sim 15\%$  higher in the present simulation thus, the associated pressure recovery over the top and lateral faces is slower. More specifically, the flow reattachment occurs at  $x_c \sim 1.65h$  compared to  $x_c \sim 1.53h$  in the previous work [33].

Figure 4.4 shows  $C_p$  on the axial and horizontal centerlines in the tandem arrangement with the separation distance  $S = h$ . The mean velocity component in the streamwise direction along the axial plane at  $y/h = 0$  on top faces of the blocks and the contour plot for the same quantity at  $y/h = 0$  is also shown here. The blocks in the tandem arrangement, as displayed in fig. 4.1. Lim and Ohba [33] did not report any experimental data for the tandem arrangement. Therefore, their modeling data are used for comparison here for this arrangement. Since these data are not DNS results, this comparison should not be interpreted

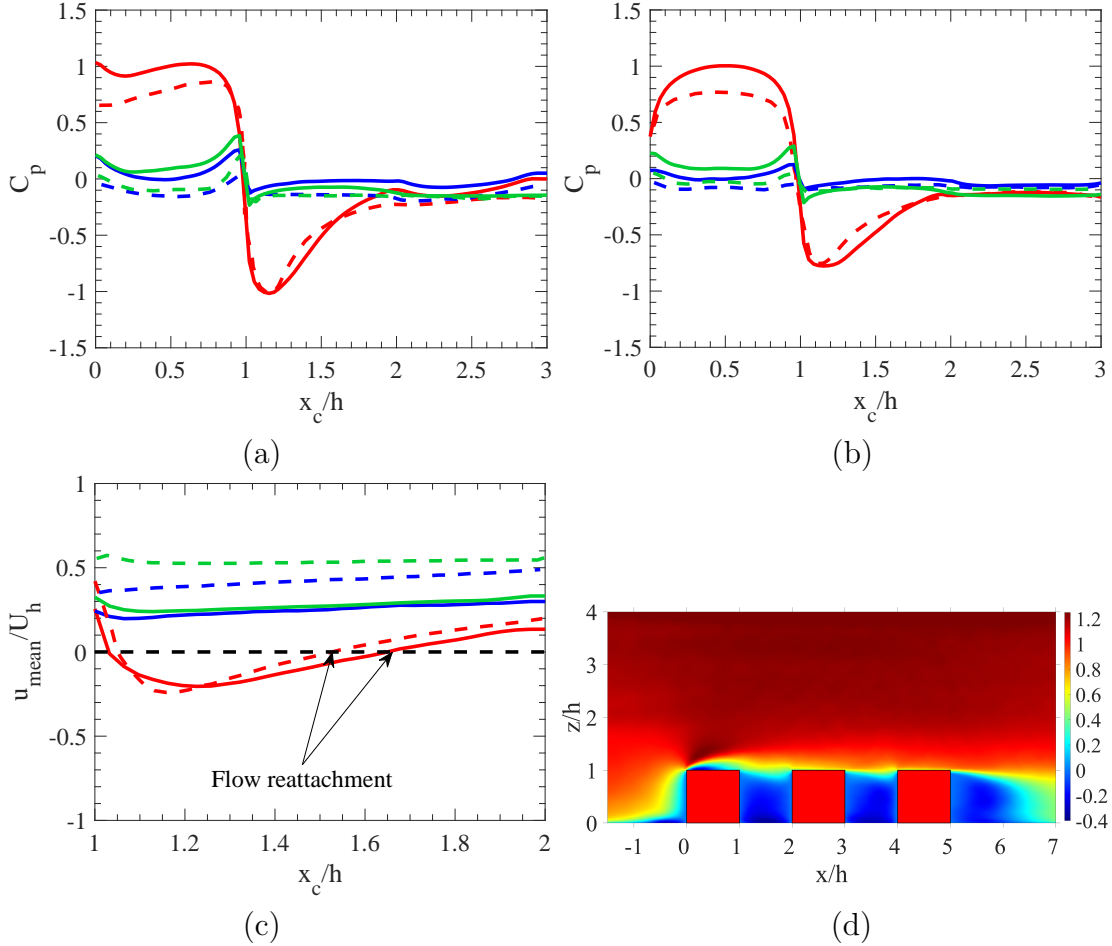


**Figure 4.4:** Tandem arrangement results in the wind scale tunnel flow; (a) pressure coefficient at the axial centerline  $y/h = 0$  on the windward face ( $0 \leq x_c/h \leq 1$ ), the top face ( $1 \leq x_c/h \leq 2$ ) and the leeward face ( $2 \leq x_c/h \leq 3$ ), and (b) pressure coefficient at the horizontal centerline  $z/h = 0.5$  on the windward face ( $0 \leq x_c/h \leq 1$ ), the lateral face ( $1 \leq x_c/h \leq 2$ ) and the leeward face ( $2 \leq x_c/h \leq 3$ ); and (c) mean streamwise velocity non-dimensionalized by  $U_h$  on the top face at the axial centerline; for previous simulation by Lim and Ohba [33] for block 1 (---), block 2 (- - -) and block 3 (- - -); and current simulation for block 1 (—), block 2 (—) and block 3 (—); along with (d) contourplot for mean streamwise velocity non-dimensionalized by  $U_h$  on  $y/h = 0$ .

as a validation exercise. Pressure coefficient and the mean velocity for block 1 in fig. 4.4 display trends similar to that in the single block as could be seen in fig.

4.3. However, the pressure coefficients over blocks 2 & 3 have similar values to each other but differ from the value over block 1. On top of blocks 2 & 3, the pressure coefficients are significantly lower than that on top of block 1 (fig. 4.4 a,b). Moreover, the mean velocity in the streamwise direction is almost constant and positive on top of blocks 2 & 3 (fig. 4.4 c,d). As such, the flow separation and re-circulation over these blocks are lacking. It is seen in this figure that pressure coefficients on the windward face of the blocks in the current simulation are  $\sim 17\%$  higher than their counterparts in the previous simulations [33]. Accordingly, the flow reattachment occurs at  $x_c \sim 1.66h$  a similar location as the single block case, but still further downstream as compared to the previous numerical data [33].

Figure 4.5(a,b) shows the  $C_p$  on the surface of block 2 (middle block) in a parallel arrangement with a separation distance  $S = h$  on the axial and horizontal centerlines. The mean streamwise velocity on top faces of the block and the contour plot for the same quantity at  $y/h = 0$  is also shown here in panels c and d, respectively. Lim and Ohba [33] only reported numerical and experimental data for the middle block. The coefficient of pressure follows the same trends as previously seen for single block and blocks in the tandem arrangement, but is over-predicted compared to the previous numerical and experimental data. The mean velocity over the top of the middle block as seen in fig. 4.5(c) is in better agreement with the previous numerical data [33] with the flow reattachment occurring at  $x_c \sim 1.72h$ . The wake on the leeward side of the block is considerably larger and the flow re-attachment also occurs further downstream when compared to the single block case, as seen in fig. 4.3(c,d). In comparison to the experimental

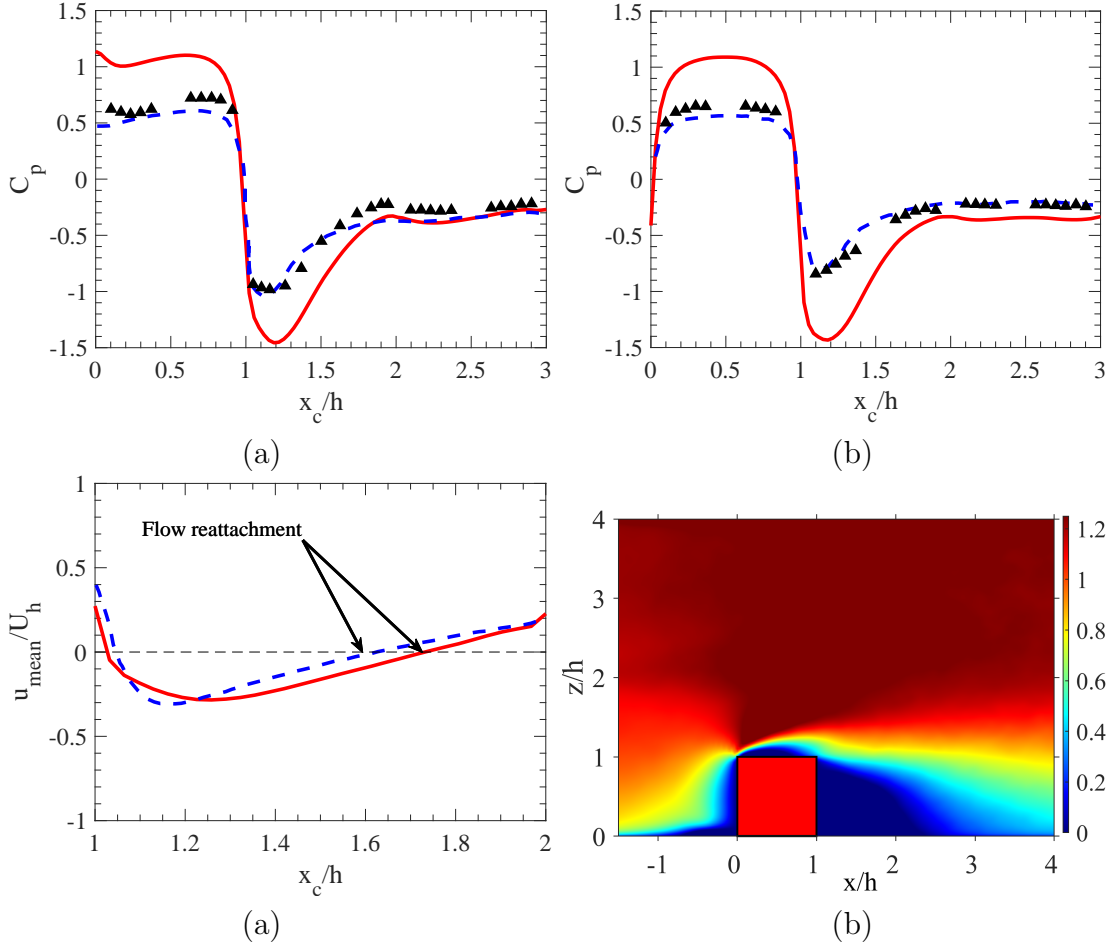


**Figure 4.5:** Parallel arrangement results in the wind tunnel flow; (a) pressure coefficient at the axial centerline  $y/h = 0$  on the windward face ( $0 \leq x_c/h \leq 1$ ), the top face ( $1 \leq x_c/h \leq 2$ ) and the leeward face ( $2 \leq x_c/h \leq 3$ ), and (b) pressure coefficient at the horizontal centerline  $z/h = 0.5$  on the windward face ( $0 \leq x_c/h \leq 1$ ), the lateral face ( $1 \leq x_c/h \leq 2$ ) and the leeward face ( $2 \leq x_c/h \leq 3$ ); and (c) mean velocity in the streamwise direction normalized by  $U_h$  on the top face at the axial centerline; for previous experiments ( $\blacktriangle$ ) and simulations (- - -) by Lim and Ohba [33], over the surface of the middle block; along with (d) contourplot for mean streamwise velocity non-dimensionalized by  $U_h$  on  $y/h = 0$ .

data, the simulations by Lim and Ohba [33] display a better performance than the present simulations for  $C_p$  in figs. 4.3 and 4.5. This is likely due to a more

advanced approach used by Lim and Ohba [33] in representing the near wall effects in the turbulent flow. Lim and Ohba [33] applied a DES approach based on a hybrid LES / Reynolds Averaged Navier-Stokes (RANS) model where LES calculated the core unsteady turbulent flows while RANS calculated the near wall region. The RANS calculations solved two additional transport equations for turbulent kinetic energy  $k$  and its dissipation rate  $\varepsilon$ . On the other hand, the present simulations utilizes a simpler approach of wall damping of the turbulent viscosity, where the turbulent viscosity of the first off-wall cell is calculated from the WALE, for wall modeling [46].

### 4.3.2 Field-Scale Flow with Firebrands

#### 4.3.2.1 Tandem Arrangement

Figure 4.6(a) shows the mean velocity in the streamwise direction vs  $z$  for the case with  $S/h = 1$  and  $U_h = 12$  m/s at two locations on the top face of T1 near the leading edge and the center of the top face at  $y = 0$ . The velocity profiles at these two locations vary as a result of flow separation at the leading edge which cause re-circulation further downstream. This is indicated by the negative velocity closer to the top face at the center. The error bars indicate the grid convergence index (GCI) calculated though a procedure proposed by Celik *et al.* [12]. For this grid convergence study the error bars are based on the data obtained from the simulations using three different grid sizes indicated by  $\Delta_1$ ,  $\Delta_2$

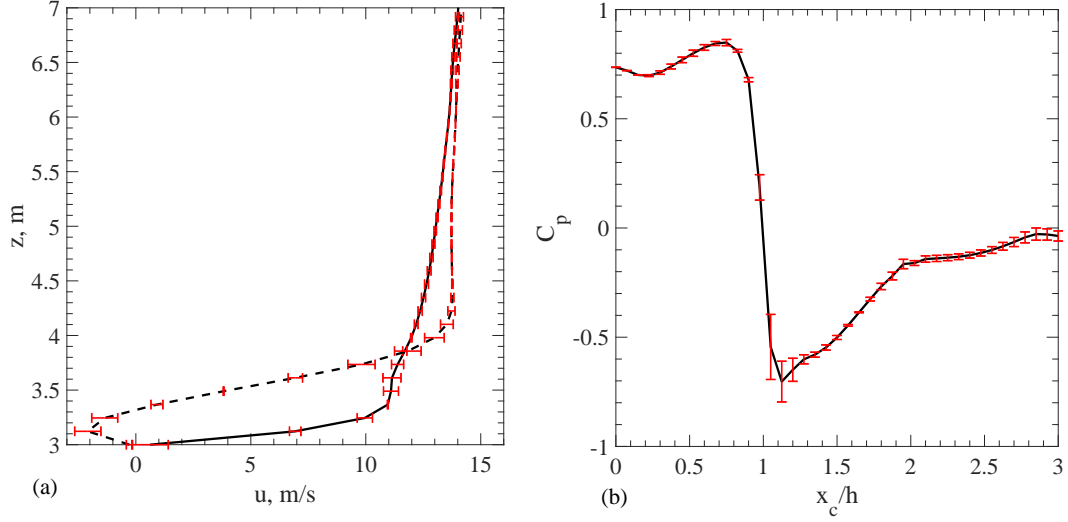


**Figure 4.6:** (a) Profile of the streamwise mean velocity at the center of the leading edge (—) and the center of the top face (- - -) of block T1; (b) pressure coefficient on axial centerline of block T1 on the windward face ( $0 \leq x_c/h \leq 1$ ), the top face ( $1 \leq x_c/h \leq 2$ ) and the leeward face ( $2 \leq x_c/h \leq 3$ ) for  $S = h$  and  $\Delta = h/16$  with error bars indicating GCI.

and  $\Delta_3$  in the corresponding sequence from the finest to the coarsest grid:

$$\text{GCI}^{21} = \frac{1.25e_a^{21}}{r_{21}^p - 1}, \quad (4.1)$$

where  $r_{21} = \Delta_2/\Delta_1$  the grid refinement factor and  $e_a^{21}$  is the approximate relative error calculated by

$$e_a^{21} = \left| \frac{\phi_1 - \phi_2}{\phi_1} \right|, \quad (4.2)$$

where  $\phi$  is the solution of the quantity of interest. In the current study, the solutions obtained for the pressure coefficient and velocity are used for this quantity. In eq. (4.2),  $\phi_1$  and  $\phi_2$  indicate the solutions obtained for grid sizes  $\Delta_1$  and  $\Delta_2$ ,

respectively, and  $p$  is the apparent order determined by solving

$$p = \frac{1}{\ln(r_{21})} \left| \ln \left| \frac{\epsilon_{32}}{\epsilon_{21}} \right| + \ln \left( \frac{r_{21}^p - \text{sign}(\epsilon_{32}/\epsilon_{21})}{r_{32}^p - \text{sign}(\epsilon_{32}/\epsilon_{21})} \right) \right|, \quad (4.3)$$

where  $r_{32} = \Delta_3/\Delta_2$ ,  $\epsilon_{21} = \phi_2 - \phi_1$  and  $\epsilon_{32} = \phi_3 - \phi_2$  where  $\phi_3$  indicates the solution obtained for  $\Delta_3$ . Eq. (4.3) is a nonlinear equation for  $p$ , solved by a fixed-point iteration method here.

A similar approach was used for the grid convergence study in LES by others [27]. It is noted that this index also include the effects of sub-grid scale and wall models since these models are also dependent on the grid size. Some attempts were made by introducing additional indices to separate subgrid-scale and numerical discretization contributions in LES [11, 10]. However, their application is limited to situations with no wall models and hence they are not calculated here. The grid sizes used here for calculation of GCI here are  $\Delta_3 = h/8$ ,  $\Delta_2 = h/10$  and  $\Delta_1 = h/16$ .

In fig. 4.6(a), the average GCI for the velocity profile at the leading edge was 2.23% and a maximum uncertainty of  $\pm 0.79$  m/s near the top face of T1. The average GCI for the profile at the center was 2.5%, with a maximum of  $\pm 0.593$  m/s also near the top face of T1. Fig. 4.6(b) shows the pressure coefficient on the surface of T1 at the axial centerline  $y/h = 0$ . The trend of  $C_p$  here is similar to the one shown in fig. 4.4(a) for the tandem arrangement in the wind tunnel flow. With the average GCI of 14.18%, the uncertainty is relatively small everywhere except around the sharp leading edge ( $0.9 \leq x_c/h \leq 1.2$ ) where it is at the range of  $\pm 0.053$  and  $\pm 0.149$ . This edge causes the flow to separate so a higher uncertainty

is expected around it. Considering the analysis above, a grid size of  $\Delta = h/10$  is used for simulations of field scale flows for firebrand deposition.

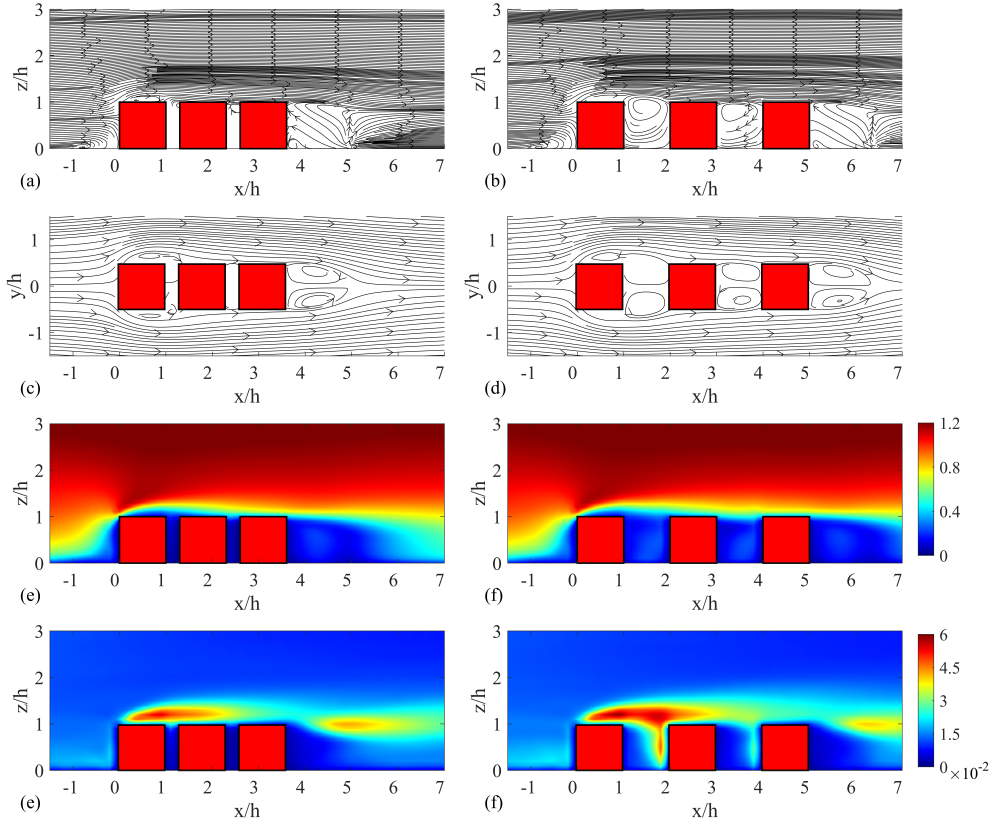


**Figure 4.7:** Mean flow characteristics for blocks in tandem arrangement with  $S/h = 0.3$  (left panels) and  $S/h = 1$  (right panels) for a  $U_h = 12$  m/s. (a,b) Mean streamlines at  $y/h = 0$ ; (c,d) mean streamlines at  $z/h = 0.5$ ; (e-f) contourplots of the mean velocity magnitude non-dimensionalized by  $U_h$  at  $y/h = 0$ ; and (g-h) contourplots of TKE non-dimensionalized by  $U_h^2$  at  $y/h = 0$ .

Figure 4.7 shows the mean streamlines, and contours of the mean velocity magnitude and the turbulence kinetic energy for  $U_h = 12$  m/s, and separation distances of  $S/h = 0.3$  (left panels) and  $S/h = 1$  (right panels). The mean streamlines in fig. 4.7(a,b) suggests that the position of the center of the horseshoe

vortex is at  $x/h \approx -0.8$  and  $y/h \approx 0.1$  on the windward side of block T1. Here, the center of the horseshoe is defined as the point inside the rotating flow where the spanwise and vertical velocity components approaches zero [70]. Flow separation takes place on the top and lateral faces of block T1, as could be seen in figure 4.7(a-d). Seen in these panels are flow re-circulations in leeward of T3 for both separation distances. These are also seen leeward of T1 and T2 for  $S/h = 1$  (panels b and d) but not for  $S/h = 0.3$  (panels a and c). For both separation distances, the velocity magnitude peaks near the top face of block T1, as could be seen in 4.7(e,f). Higher TKE values could be seen over top faces of blocks T1, T2 and approximately a block length leeward of T3 at a block height. For  $S/h = 1$ , a high value of TKE is also seen on the windward face of block T2.

To quantify the spatial distribution of the deposited firebrands, a criterion proposed by [5] based on normalized number density (NND) defined by:

$$\hat{f}(x, y) = \frac{1}{nB^2} \sum_{i=1}^n \kappa \left( \frac{x - x_i}{B}, \frac{y - y_i}{B} \right), \quad (4.4)$$

was used. Here,  $\hat{f}$  is the probability density function normalized by the total number of particles  $n$  deposited over an area of  $B^2$  where  $B$  is the bandwidth set to 0.1 m. Thus, the number density is equivalent to the number of firebrands deposited per unit area. The units of the  $\hat{f}$  is  $1/\text{m}^2$ .  $x_i$  and  $y_i$  are the landing coordinates of the  $i^{\text{th}}$  firebrand. A Gaussian function was selected as the kernel function [43] here. Once a firebrand was deposited on a surface, its position and temperature were saved and it was eliminated from the simulation.

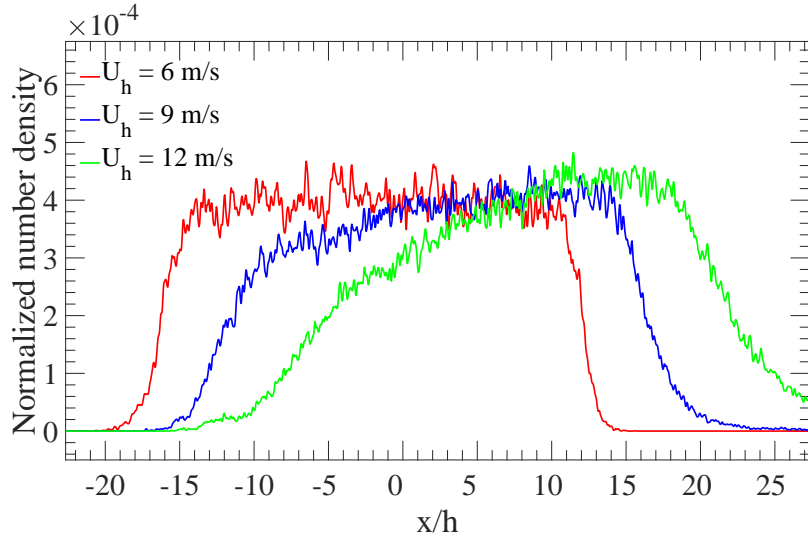


**Figure 4.8:** Normalized number density ( $NND_o$ ) with no blocks of the firebrands deposited on the ground vs  $x/h$  at  $y/h = 0$  in simulations with no blocks for  $U_h = 6, 9$  and  $12$  m/s.

To help with the evaluation of the impact of the blocks in firebrand deposition, additional simulations were conducted and the NND of the deposited firebrands were calculated for the configuration displayed in fig. 4.2 without any blocks (open field). The NND calculated from the no block simulations are indicated by  $NND_o$ . Figure 4.8 shows  $NND_o$  against  $x$  for the three different values of  $U_h$ .  $NND_o$  displayed an inappreciable variation in the spanwise  $y$  direction. It could be seen in fig. 4.8 that at lower values of  $x/h$  which is the region close to the inlet,  $NND_o$  vanishes indicating that no firebrands are deposited in this region. As  $U_h$  increases, this region further expands in the streamwise direction. The reason is that overall the drag force is larger at higher wind speeds and as a result the descending firebrands travel for longer distances. For  $U_h = 6$  m/s,  $NND_o$  in-

creases rapidly vs  $x/h$ , reaching an almost constant value and then rapidly drops. On the other hand, for  $U_h = 12$  m/s,  $NND_o$  rather gradually increases, reaching a peak value and then gradually decreases. This gradual behavior is somewhat attributed to turbulent diffusion in transport of firebrands [5], which is a more significant effect at a higher speed of wind mainly because firebrands stay longer at the flying state. Additionally, since the turbulent fluctuation is stronger for the flow at higher wind speeds, this effect is more pronounced. It is recalled that at the inlet the turbulence intensity which is a dimensionless parameter is the same in all simulations, and therefore the turbulent fluctuation is stronger at higher wind speeds at the inlet.

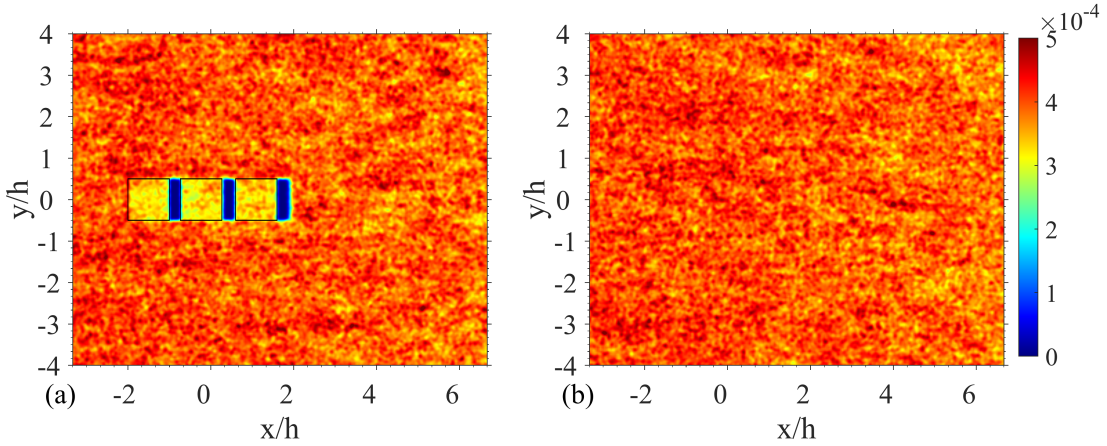


**Figure 4.9:** Contour plots for (a) Normalized number density ( $NND_s$ ) with blocks in tandem arrangement with  $S = 0.3h$ , and (b) Normalized number density ( $NND_o$ ) with no blocks at  $U_h = 6$  m/s.

To quantify the deposition of firebrands in the simulations with the blocks relative to the ones without the blocks, the relative normalized number density is

defined and calculated

$$\text{NND}_{\text{rel}} = \text{NND}_{\text{s}} - \text{NND}_{\text{o}}, \quad (4.5)$$

where  $\text{NND}_{\text{s}}$  denotes the NND of the simulation with the blocks corresponding

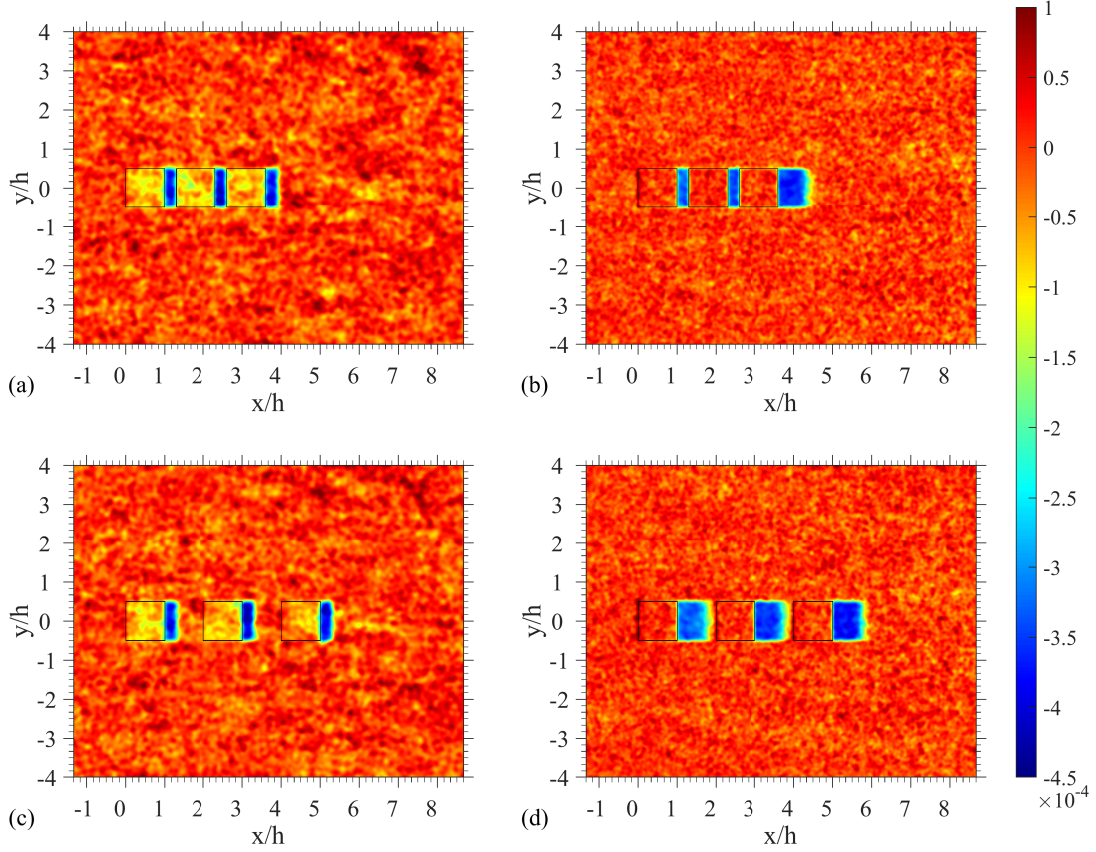


**Figure 4.10:** Contour plots of relative normalized number density ( $\text{NND}_{\text{rel}}$ ) for blocks in tandem arrangements with (a)  $S/h = 0.3$  and  $U_h = 6$  m/s; (b)  $S/h = 0.3$  and  $U_h = 12$  m/s; (c)  $S/h = 1$  and  $U_h = 6$  m/s; and (d)  $S/h = 0.3$  and  $U_h = 12$  m/s.

to the  $\text{NND}_{\text{o}}$  at the same  $U_h$ . For clarification of this definition, as an example, consider figs. 4.9(a,b) and 4.10(a) all corresponding to  $U_h = 6$  m/s. Fig. 4.9(a) shows the contourplot of the  $\text{NND}_{\text{s}}$  for the simulation with the tandem blocks and

fig. 4.9(b) shows  $\text{NND}_o$  obtained from the corresponding simulation without the blocks. The  $\text{NND}_{\text{rel}}$  is calculated from these simulations as shown in fig. 4.10(a). An area with positive (or negative) values of  $\text{NND}_{\text{rel}}$  in this panel indicates that it has more (or less) deposited firebrands as compared to the same area in the corresponding no block simulation. It could be seen in fig. 4.10 with panels for two different wind speeds and two different separation distance,  $\text{NND}_{\text{rel}}$  are the least ( $-4.5 \times 10^{-4}$ ) on the leeward areas of the blocks. These are the areas that receive no firebrand, which is predominantly because of the blocks shielding some firebrands from landing on their leeward. This shielding mechanism was also effective in the single block simulations seen in §3.3.3, where the leeward region with no deposited firebrands was referred to as the safe zone. It could be also seen in this figure that top faces of the blocks in  $U_h = 6$  m/s have significant negative values, which is discussed next.

In fig. 4.11,  $\text{NND}_{\text{rel}}$  is plotted versus  $x/h$  for firebrands deposited on the ground and the top faces of the blocks. The positions of the blocks are indicated by the horizontal bars with a length identical to  $h$  in this figure. The troughs in the curves are associated with the safe zones in leeward of the blocks. Moreover, at a wind speed of  $U_h = 6$  m/s,  $\text{NND}_{\text{rel}}$  appreciably drops below zero on the top faces of the blocks, *e.g.*,  $0 < x < 1$  in panel (a). Considering the definition of  $\text{NND}_{\text{rel}}$ , this drop indicates that overall, the number of firebrands deposited on the top face of the block is less than the number of firebrands deposited on an area that is the projection of the top face on the ground in the associated no block simulation. The overall area where particles are deposited is greater

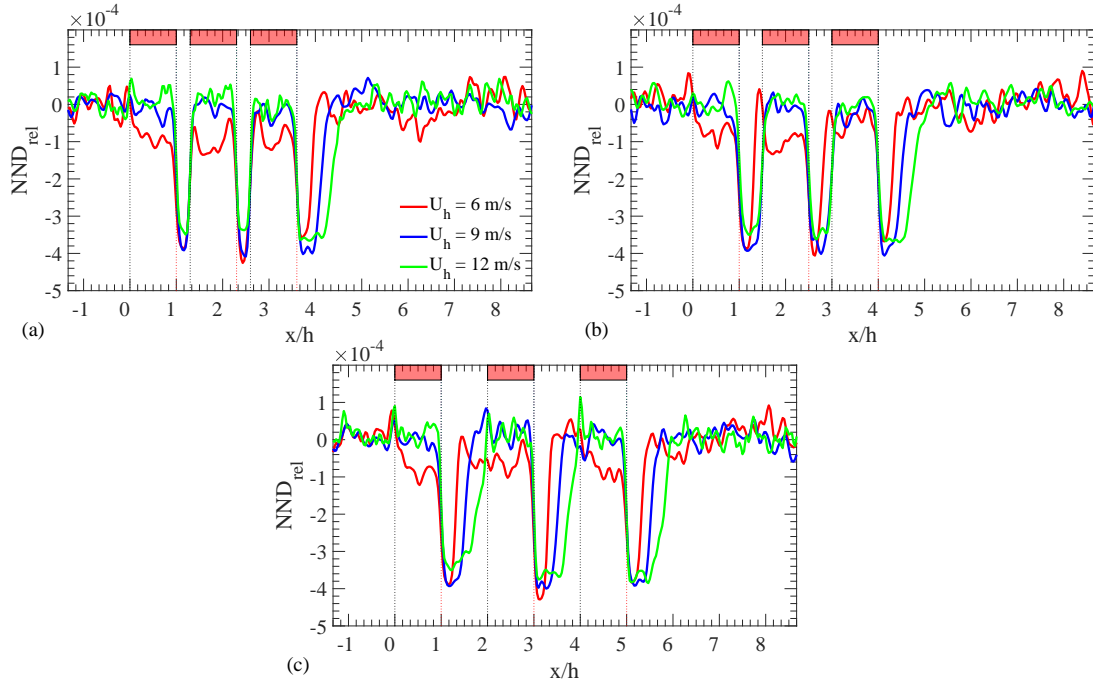


**Figure 4.11:** Relative normalized number density ( $NND_{rel}$ ) vs  $x/h$  for blocks in tandem arrangements at  $y/h = 0$  for  $S/h$  of (a) 0.3; (b) 0.5; and (c) 1. The streamwise location of the blocks are indicated by the horizontal bars seen at the top of the sub-figures.

in the simulations with blocks than the associated simulations with no blocks. The added area is equivalent to the lateral faces of the blocks. On the other hand, since firebrands are released with the same flux in both of the simulations with blocks and with no blocks, the number of particles deposited per unit area will reduce where the deposition area is increased. This effect manifests itself in an overall negative  $NND_{rel}$  on top faces of the blocks in wind speeds of 6 m/s. However,  $NND_{rel}$  plotted in Fig. 4.11 does not suggest this for higher wind speeds. The reason is that this effect is in competition with the effect of blocks shielding

firebrands from deposition in leeward area. The latter effect is more pronounced with an increasing wind speed and it manifests itself in longer safe zone areas at higher speeds, as could be seen in fig. 4.12. The expansion of these areas is the result of more firebrands shielded by the block from deposition in the block leeward. In the simulations with  $U_h = 6$  m/s and  $S/h = 0.3$  and  $0.5$ , blocks T2 and T3 are placed sufficiently close to each other to be in the wake of blocks T1 and T2, respectively. This leads to a flow separation at the leading edge of block T1 followed by reattachment over block T2 (as seen in fig. 4.7(a) for  $S/h = 0.3$ ). This in turn leads to a drop in  $NND_{rel} \approx -1 \times 10^{-4}$  from the leading edge to the trailing edge over the top face of block T1. For  $S/h = 0.3$ ,  $NND_{rel}$  remains around  $-1 \times 10^{-4}$  over the top face of blocks T2 & T3. On the other hand, for  $S/h = 0.5$ ,  $NND_{rel}$  increases close to 0 over block T3. This effect is similar to the drop and rise in NND over the top face of a single block with longer lengths seen in previous §3.3.3. Compared to this wind speed, the variation of  $NND_{rel}$  on the top faces of the blocks is not significant at higher wind speeds.

To gain more insight into the size and shape of the safe zones, fig. 4.12 is plotted with the scattered dots indicating the centers of mass of the deposited firebrands, on the leeward of block T3 for  $U_h = 12$  m/s and  $S/h = 1$ . The lines shown in this figure are the borderlines separating the safe zones with no firebrands from the surrounding area with deposited firebrands. They are plotted for three different wind speeds. The lines are drawn by first dividing the leeward area into narrow stripes oriented in the streamwise direction and identifying the firebrand deposited closest to the block on each strip, and then connecting the

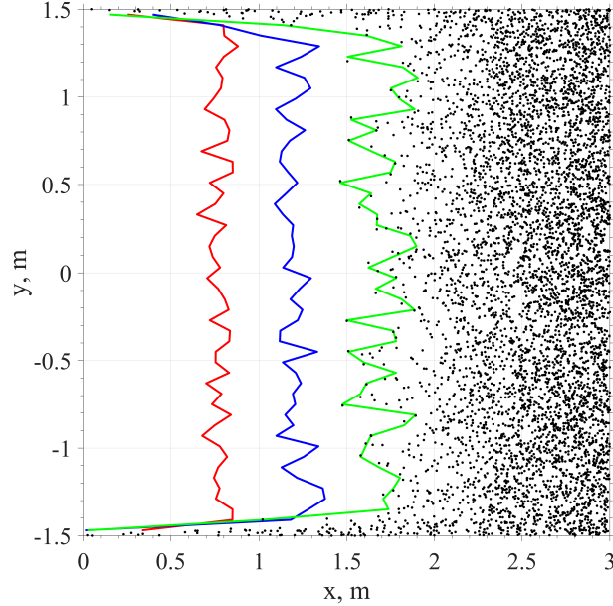


**Figure 4.12:** Scatter plot of the firebrands deposited on the leeward side of block T3 in tandem arrangement with  $S/h = 1$  at  $U_h = 12$  m/s. The lines indicate the interface between the safe zone and the area with deposited firebrands for  $U_h = 6$  (—),  $9$  (—) and  $12$  m/s (—).

identified firebrands on all stripes. The safe zones shown with the borderlines in fig. 4.12 are nearly an isosceles trapezoid in shape. The reason to the particular orientation of the trapezoid legs seen in this figure is most likely the turbulent diffusion of flying firebrands. One of the bases of the trapezoid is the lower side of the rectangular leeward face of the block. The other downwind base is shorter and has some roughness. The height of the trapezoid is referred to as the safe zone length  $l_r$ , which is longer for a higher wind speed as evident in fig. 4.12. The trajectories of firebrands flying at higher wind speeds overall make smaller angles with the horizontal and when they are shielded by the blocks, the outcome is a longer safe zone in the wind direction.

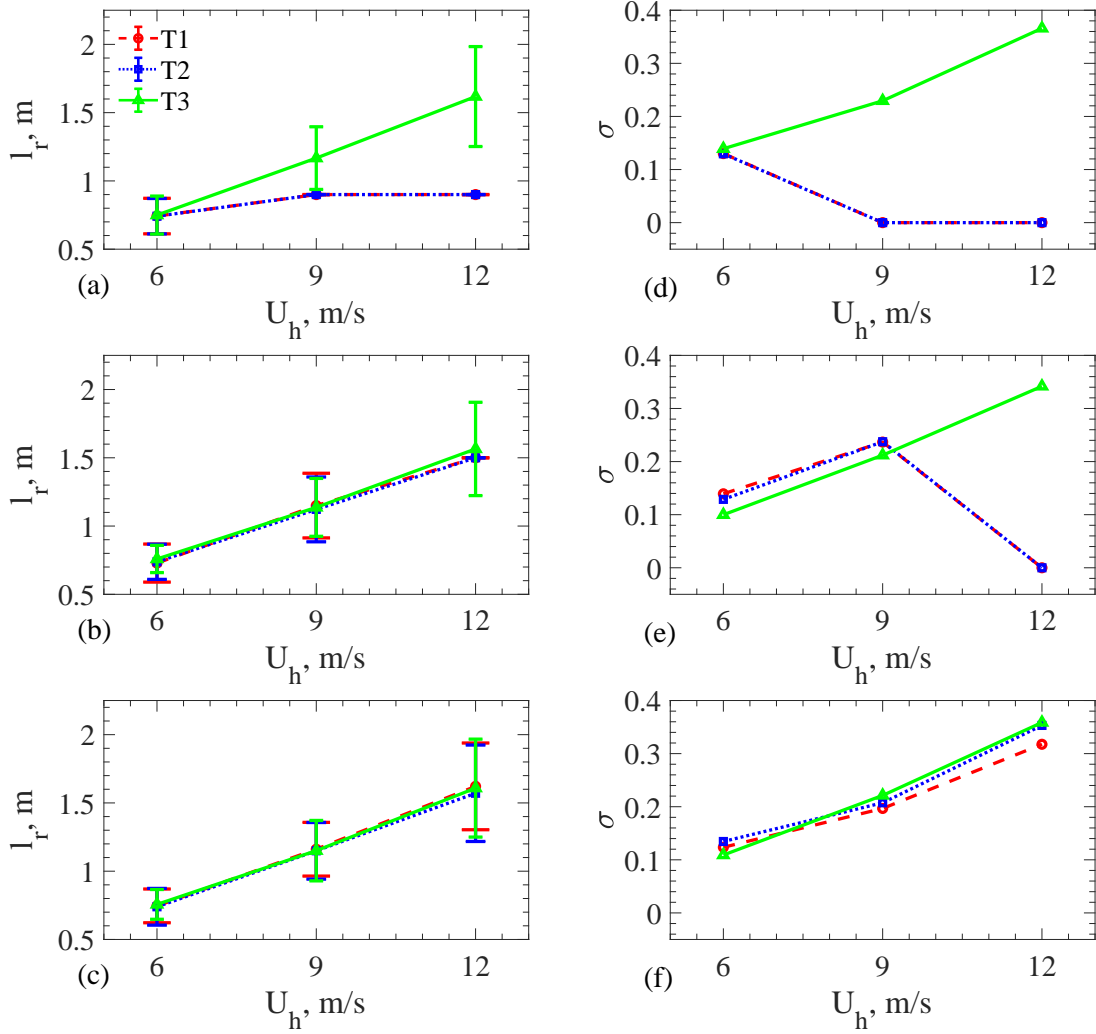


**Figure 4.13:** Mean safe zone length  $l_r$ , panels (a-c) and standard deviation of safe zone length  $\sigma$ , panels (d-f) on the surface of the ground beyond the leeward face of blocks T1-3 in tandem arrangements versus  $U_h$  for  $S/h$  of (a,d) 0.3; (b,e) 0.5; and (c,f) 1.

The safe zone length is plotted versus the wind speed for blocks in fig. 4.13(a-c) where the error bars indicate the standard deviation  $\sigma$  of the safe zone length (the roughness of the downwind base of the trapezoid as could be

seen in fig. 4.12). Standard deviation is also plotted separately in figure 4.13(d-f). For T3, both safe zone length and standard deviation increase approximately linearly with the wind speed. However, for a given wind speed, they do not appear sensitive to the separation distance or the position of the block in the tandem arrangement. For cases with  $S/h = 0.3$ ,  $U_h = 9$ ;  $S/h = 0.3$ ,  $U_h = 12$ ; and  $S/h = 0.5$ ,  $U_h = 12$ ; the safe zone created by blocks T1 and T2 encroaches on the windward faces of the downstream blocks T2 and T3, respectively. As a result, the safe zone length in these cases is identical to the separation distance with zero standard deviation.

Figure 4.14 shows the scatter plot of firebrands (indicated by dots) deposited on the faces of the blocks for  $U_h = 12$  m/s and  $S/h = 0.3$ . Here, the dot colour indicates the firebrand temperature at the time of deposition. It is noted that since no firebrands were deposited on the leeward faces of any of the blocks in the current simulations, these faces are not shown in this figure. On the other hand, the windward face in each panel is shown by the square in the middle of the first column of squares. A roughly rectangular area could be seen on the bottom half of windward faces of T2 and T3 without any deposited firebrands in figure 4.14(b,c). This could be considered the vertical extension of the safe zone created by the shielding effect of the upwind block encroaching on the windward faces of the downward blocks. Relatively higher temperature firebrands are deposited on the interface between encroached area and the area where firebrands were deposited on the windward faces of these blocks. It is suspected that due to turbulent wind certain firebrands have a shorter distance to travel compared to

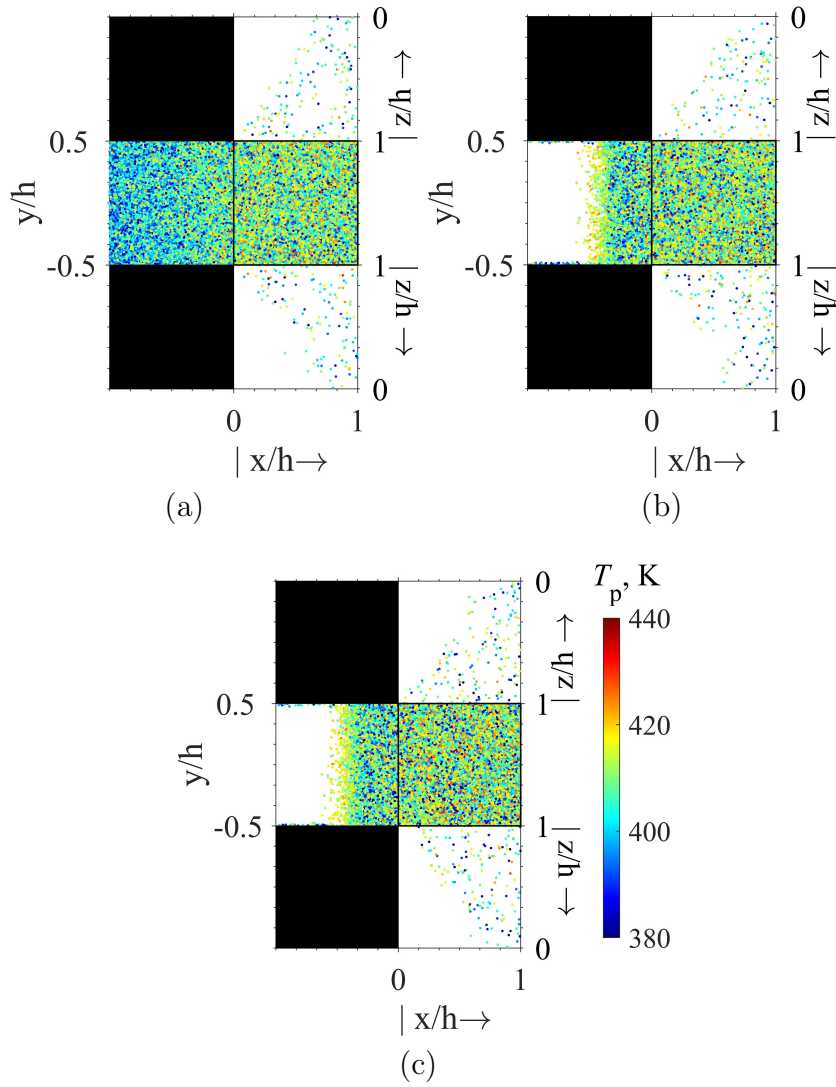


**Figure 4.14:** Scatter plots of the centers of mass of the firebrands deposited on the faces of blocks T1-3 the tandem arrangement with  $S/h = 0.3$  and  $U_h = 12$  m/s. Color indicates the firebrand temperature at the deposition instant. In each sub-figure, the first and second squares on the second row indicate the windward and top faces of the block, respectively. The first and third squares on the second column indicate the left and right lateral faces of the block, respectively, in the direction of the flow.

others, thus having less time to lose heat and mass leading to a relatively higher temperature and higher mass of firebrands at the time of deposition. Thus these

firebrands with higher mass tend to deposit closer to the bottom of the windward faces. The interface becomes closer to the bottom of the windward faces and eventually meets the ground at larger separation distances or lower wind speeds. On the lateral faces, the firebrand deposited area has triangular shapes for all three blocks shown in fig. 4.14. Similar triangular shapes were reported for single block simulations in §3.3.3. Reviewing the same data for lower wind speeds, revealed that the base of this triangular region decreased with a decrease in wind speed.

#### 4.3.2.2 Parallel Arrangement

Figure 4.15 shows the mean streamlines on planes  $y/h = 0$  and  $z/h = 0.5$ , and contour plots of mean velocity magnitude normalized by  $U_h$  and TKE normalized by  $U_h^2$  on plane  $y/h = 0$  for the parallel arrangement at  $U_h = 12$  m/s and two separation distances  $S/h = 0.3$  and 1. An obvious difference in the flow features between the two separation distances is a significantly greater size of the re-circulation region of middle blocks (A2) compared to side blocks for the smaller separation distance (panel c). For the larger separation distance (panel d), the circulation regions of all three block have a similar size but the wakes of the side blocks appear asymmetric. This lacking symmetry could be also seen in the case of a smaller separation distance (panel c). The asymmetric feature manifest itself in a flow separation which is more significant on the outer face of the side blocks (A1 & A3) compared to their inner face. Examining streamlines in figure 4.15(a,b) reveals that for  $S/h = 1$ , the center of the horse shoe vortex is

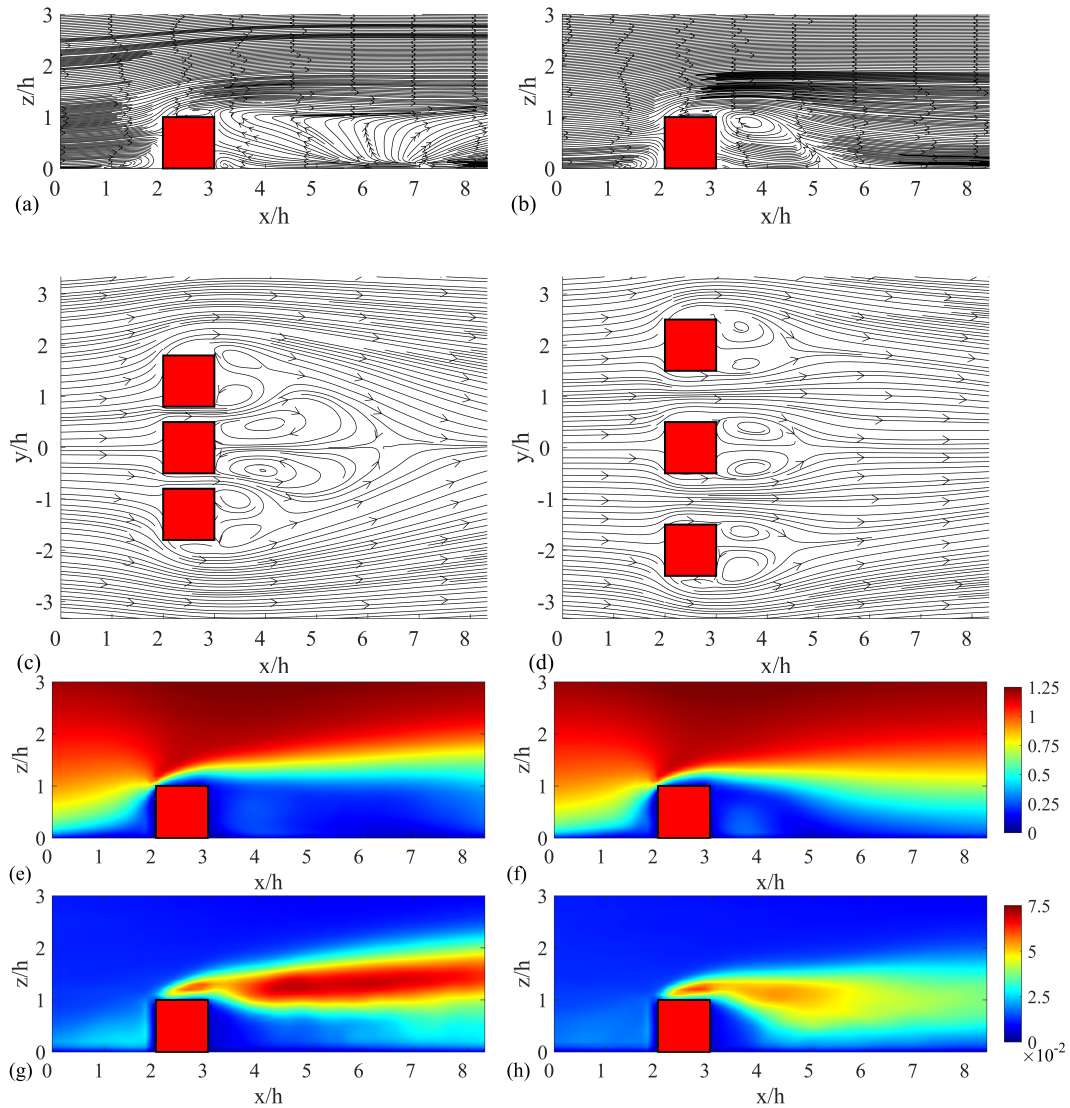


**Figure 4.15:** Mean flow characteristics for block in parallel arrangement at  $U_h = 12$  m/s with  $S/h = 0.3$  (left panels) and  $S/h = 1$  (right panels); mean streamlines at (a,b)  $y/h = 0$  and (c,d)  $z/h = 0.5$ ; (e-f) contour plots of mean velocity magnitude normalized by  $U_h$  at  $y/h = 0$ ; and (g-h) TKE normalized by  $U_h^2$  at  $y/h = 0$ .

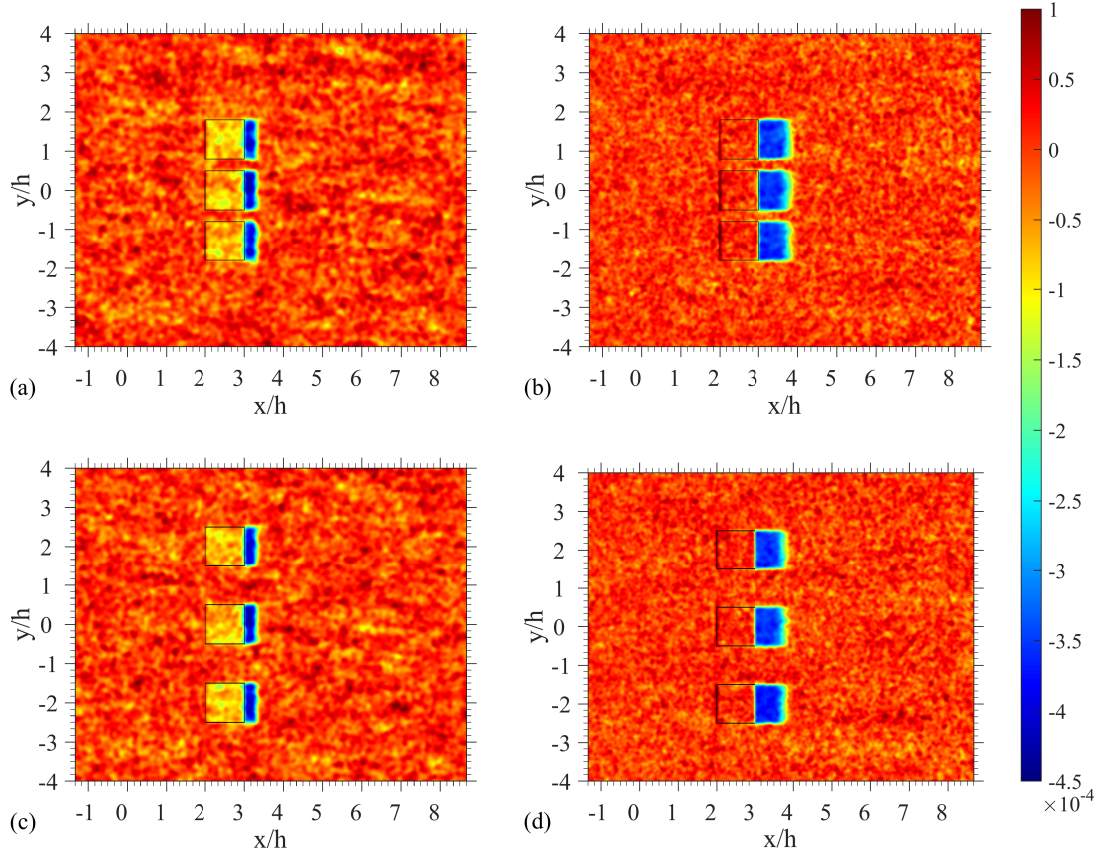
at  $x/h \approx 1.3$  (panel b) but for  $S/h = 0.3$ , is slightly further upwind at  $x/h \approx 1.2$ .

A reason to this difference is that a close proximity of the blocks impedes the

flow more than when they are placed further apart. Accordingly, a longer and wider re-circulation region is formed in the wake of the middle block for a smaller separation distance. The contours of mean velocity magnitude and TKE in figure 4.15(e-h) are another indication of the wake being further stretched out downwind in  $S/h = 0.3$ , as compared to  $S/h = 1$ . Overall, the TKE in the wake of the middle block is higher for the small separation distance, as compared in panel (g) versus panel (h).

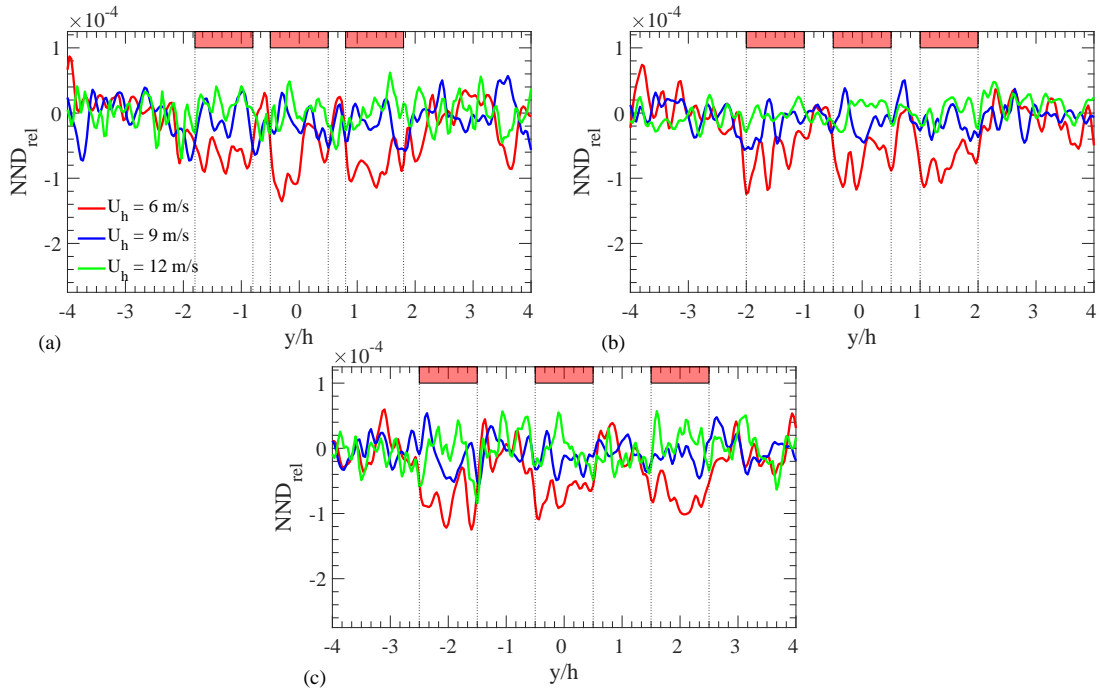
Figure 4.16 shows contour plots of  $NND_{rel}$  for  $U_h = 6$  and 12 m/s, and  $S/h = 0.3$  and 1. It could be seen that  $NND_{rel}$  on top faces of the blocks in the low wind speed cases (panels a and c) is lower than that on the ground excluding the leeward regions. On the other hand, the higher wind speed panels (b and d) do not display such a difference. Therefore, as for the overall difference between the  $NND_{rel}$  values on the top faces and the ground, the parallel arrangement is similar to the tandem arrangement. A detailed analysis of the safe zones revealed that they are nearly isosceles trapezoids, as in the tandem arrangement.

To further evaluate the distribution of  $NND_{rel}$  in the parallel arrangement,  $NND_{rel}$  is plotted vs  $y/h$  at  $x/h = 2.5$  in fig. 4.17. For  $U_h = 6$  m/s and  $S/h = 0.3$ ,  $NND_{rel}$  overall seems to be the lowest on the top faces of the middle block. More specifically, it tends to increase on average with the increase of  $|y|/h$  for the side blocks. The case with  $S/h = 0.5$  or 1 does not display such propensity. Therefore, the proximity of the blocks in a parallel arrangement appears to affect  $NND_{rel}$  on the top faces only for the smallest separation distance and wind speed.



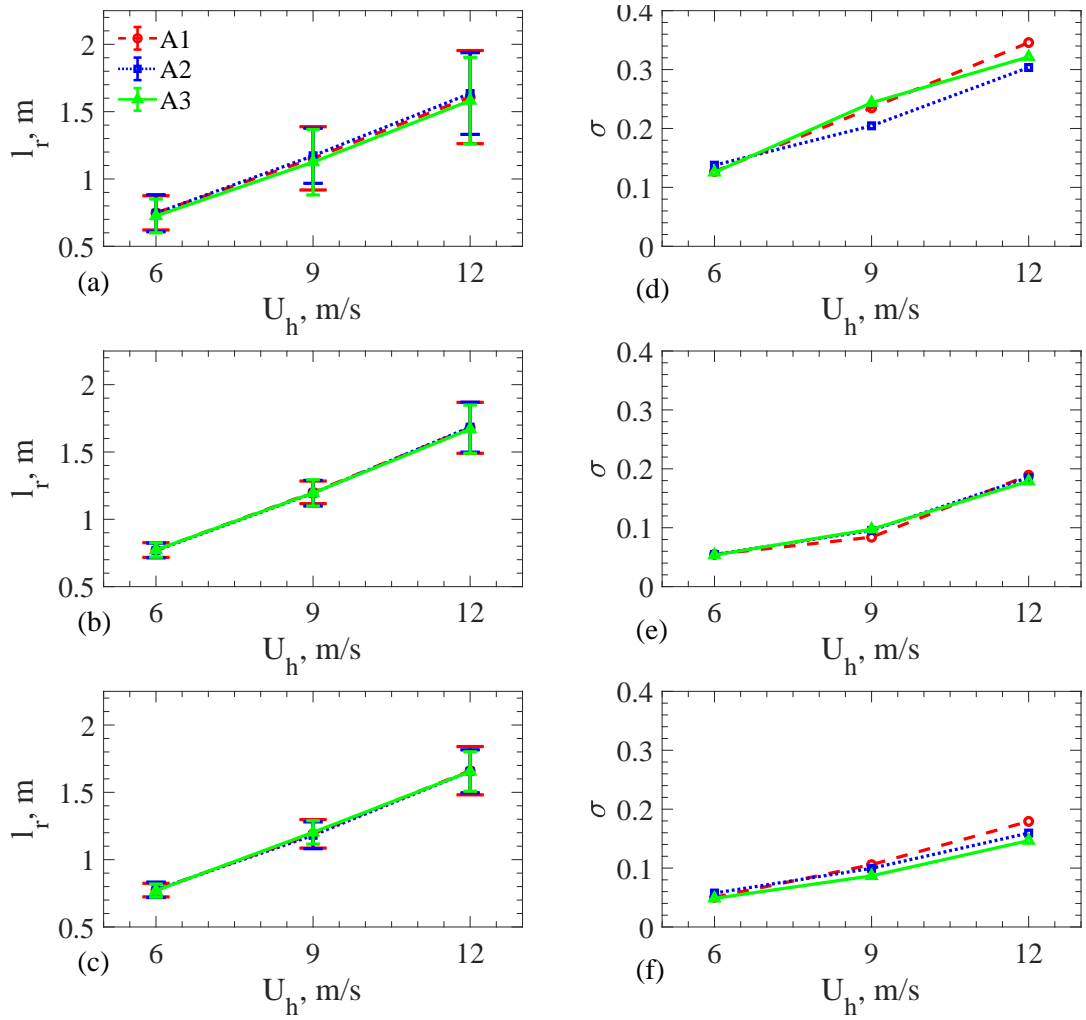
**Figure 4.16:** Contour plots for relative normalized number density ( $NND_{rel}$ ) for blocks in parallel arrangement with separation distance with (a)  $S/h = 0.3$ ,  $U_h = 6$  m/s; (b)  $S/h = 0.3$ ,  $U_h = 12$  m/s; (c)  $S/h = 1$ ,  $U_h = 6$  m/s; and (d)  $S/h = 0.3$ ,  $U_h = 12$  m/s.

Figure 4.18(a-c) shows the safe zone length vs  $U_h$  for the blocks in the parallel arrangement with the error bar indicating its standard deviation, which is also plotted separately vs  $U_h$  in fig. 4.18(d-f). It could be seen that both  $l_r$  and  $\sigma$  increase roughly linearly with the wind speed for a given  $S/h$ . This figure does not suggest that  $l_r$  is significantly sensitive to the position of the block in the arrangement. At  $U_h = 12$  m/s,  $l_r$  for  $S/h = 0.3$  (panel a) is slightly smaller



**Figure 4.17:** Relative normalized number density ( $NND_{rel}$ ) vs  $y/h$  at  $x/h = 2.5$  for blocks in parallel arrangement for  $U_h = 6, 9$  and  $12$  m/s and  $S/h$  of (a) 0.3; (b) 0.5; and (c) 1.

than that for larger separation distances (panel b and c) while for the rest of wind speeds,  $l_r$  does not seem sensitive to the separation distance at a fixed wind speed. It could be seen in fig. 4.18 that the standard deviation of the safe zone length for  $S/h = 0.3$  (panel d) is significantly larger than that for  $S/h = 0.5$  and 1 (panels e and f) at all wind speeds. This decrease suggest that a closer proximity of the blocks creates more roughness interface between the safe zone and deposited firebrands. The standard deviation does not appear very sensitivity to where the block is located in the array except for perhaps  $S/h = 0.3$  (panel d) at  $U_h = 9$  and  $12$  m/s.



**Figure 4.18:** Mean safe zone length  $l_r$ , panels (a-c) and standard deviation of safe zone length  $\sigma$ , panels (d-f) on the surface of the ground beyond the leeward face of blocks A1-3 in parallel arrangement vs  $U_h$  for  $S/h$  of (a,d) 0.3, (b,e) 0.5 and (c,f) 1.

#### 4.4 Chapter Summary

The wind-tunnel measurement and modeling data of flows over cubic blocks by Lim and Ohba [33] were used to validate FDS [45] utilized here to model the flow. The calculated pressure coefficients in the single block simulations were overall in reasonable agreement with previously measured and simulated data. The current simulations displayed a higher value for this variable on the windward face and a lower value over the top face. They also displayed a slower pressure recovery with the flow reattachment taking place slightly further downstream. The mean velocity profile on the top face of the block calculated here for single-structure simulations was in reasonable agreement with that in the previous study [33]. For multiple structures in the tandem arrangement, the pressure coefficients on the faces of the blocks were in reasonable agreement with the previous simulation data. Further, the mean velocity profile on top of the leading block in the current simulations was in very good agreement with that in the previous simulation. However, there was a notable difference between the mean velocity profiles of the current and previous simulations for the second and third blocks while the trends of these profiles were correctly captured here. In the parallel arrangement, the difference between current simulated pressure coefficients and their measured counterparts was notable but the agreement between current simulated and previous measured velocities was reasonable. Overall, for all studied arrangements, the model by Lim and Ohba [33] displayed a better performance than the model here, as their associated pressure coefficients were

compared against the previous measured pressure coefficients. This superior performance was likely attributed to the use of DES by Lim and Ohba [33], a model which is more consistent with representing the near wall effects in turbulence than how FDS takes these effects into account.

Next, simulations were performed to study the deposition of wind-carrying cylindrical firebrands over three-meter high cubic blocks in tandem and parallel arrangements. With varying separation distance and wind speeds relevant to neighbouring structures in a WUI community. This study was performed using the firebrand model mentioned in chapter 2 in the FDS computational framework. Additional simulations were performed with no blocks to help with determining the influence of blocks in firebrand deposition. It was found that the blocks shielded their immediate leeward areas on the ground from deposition of firebrands. Referred to as the safe zones, these areas were distinguished with no deposited firebrands and displayed an isosceles trapezoid shape. The longer base of the trapezoid was identical to the leeward edge of the block and the shorter base was a result of the interface created between the deposited firebrands and the safe zone. The shorter base had some roughness as a result of turbulence dispersion of flying firebrands [5]. The calculated height of the trapezoid was calculated to be the mean distance from the leeward face of the block to the interface between safe zone and the deposited firebrands. The safe zone length and its standard deviation (representing the mean roughness of the shorter base) increased linearly in both arrangements with the wind speeds. Neither the safe zone length nor the

standard deviation exhibited significant sensitivity to the position of the block in the parallel arrangement.

For blocks in the tandem arrangement with a smaller separation distance and/or higher wind speeds, the safe zone encroaches on to the windward face of the downward block. As a result, the upwind block also shielded the lower part of the windward face of the downward block from firebrand deposition in these cases. In both arrangements at low wind speeds, the number of firebrands deposited on the top face of the block was less than the number of firebrands deposited on an area that was the projection of the top face on the ground in the associated no block simulation. This was attributed to the fact that the overall area where particles were deposited was greater in the simulations with blocks than the associated simulations with no blocks, considering the added area of the lateral faces of the blocks. However, this effect was in competition with another effect of blocks shielding firebrands from deposition in leeward area. At higher wind speeds, more firebrands were shielded by the block and made up for the decreased number of firebrands per unit area as the outcome of the first effect. In none of the simulations, firebrands were deposited on the leeward faces. In all simulations, the number of firebrands deposited on the lateral faces parallel to the wind direct was much smaller than that on the windward faces.

## Chapter 5. Cuboidal Firebrand Deposition Between Two Adjacent Blocks

### 5.1 Introduction

In this chapter, a model was developed in the FDS framework to track cuboidal firebrands in flight and then sliding on the ground. The mathematical and computational description of this model can be found in Chapter 2. This firebrand model was utilized to replicate and further understand firebrand deposition and accumulation seen in the previous experiments by Suzuki and Manzello [75]. The computational setup details and results are shown in §5.2 and §5.3, respectively.

### 5.2 Computational Setup

A computational domain with dimensions of  $16 \times 5 \times 13.5$  m (streamwise  $\times$  spanwise  $\times$  vertical) resembling the wind tunnel setup in the measurements of Suzuki and Manzello [75] was constructed in FDS, as seen in fig. 5.1. The domain was divided into a coarser and a finer grid resolutions. This was done to implement grid stretching in the vertical in the lower part of the domain without overstretching the rest of the domain. As over stretching the grid would lead to

inaccuracies in the flow simulation. The coarser grid was uniform with a resolution

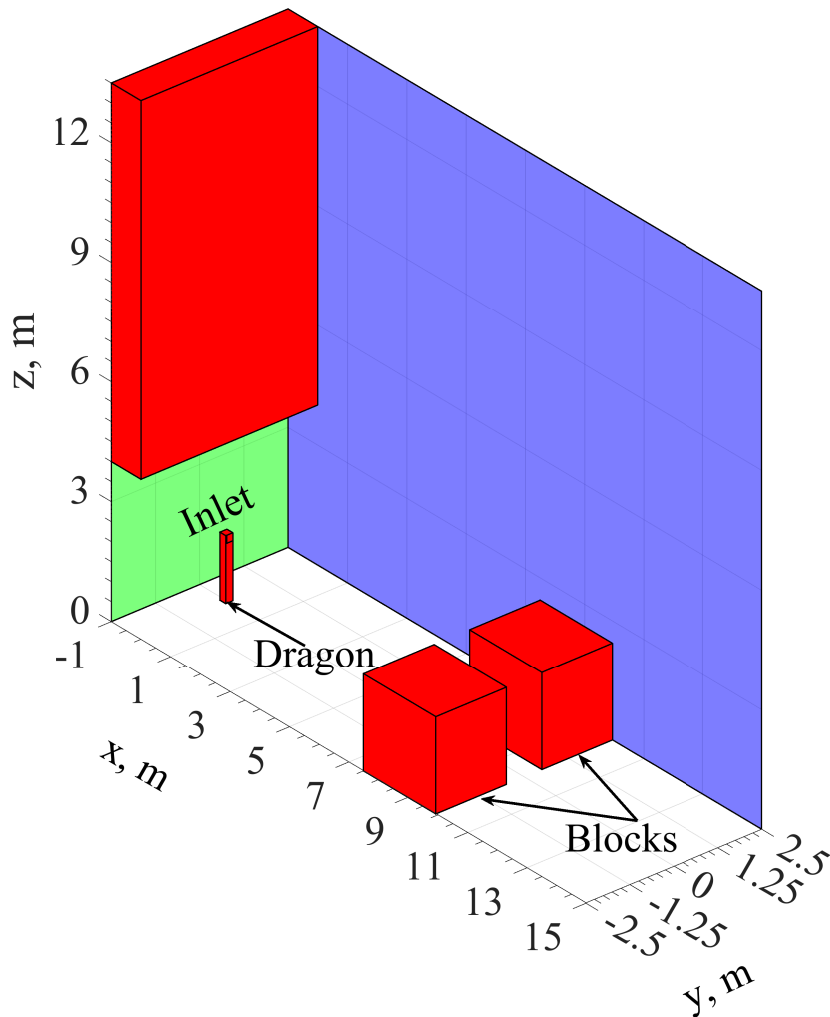


**Figure 5.1:** The computational configuration resembling the experimental setup of Suzuki and Manzello [75].

of  $160 \times 50 \times 59$  (streamwise\timesspanwise\timesvertical) and was implemented for the top part of the domain *i.e.*, from  $z = 1.7$  to  $13.5$  m. The finer grid with the resolution of  $320 \times 100 \times 34$  (streamwise\timesspanwise\timesvertical) was implemented

for the bottom part of the domain *i.e.*,  $z = 0$  to 1.7 m. The finer grid was vertically stretched in the direction normal to the ground.

The NIST dragon was represented by a rectangular block with dimensions of  $0.3 \times 0.3 \times 1.7$  m (length $\times$ width $\times$ height) placed one meter from the inlet and two blocks of  $2.44 \times 2 \times 2.44$  m (length $\times$ width $\times$ height) were placed 7.5 m downstream of the dragon mounted to the ground and stuck to the lateral walls of the tunnel. The inlet condition of the domain was set to a uniform wind speed with different values  $U_w = 4, 6, 8$  and 10 m/s for the analysis of the sensitivity of the results to the wind speed. This set of wind speeds is identical to the one used in the previous experiments [75]. The lateral boundaries are set to be walls. The outlet and top boundaries of the domain are set to be open. Represented in the simulations was the outflow of gases from the mouth of the dragon, reported by Suzuki and Manzello [75] to have a velocity 3 m/s.

After the flow reached a statistically stationary state, firebrands were released from the mouth of the dragon at a rate of 1,000 per second in the time interval of  $t = 10$  and 30 s. It was verified that turbulence was reached a statistically stationary state before the onset of this time interval. The velocities of the firebrands were not measured in the experiments so in the simulations they were assumed to exit the dragon with a velocity identical to the velocity of exiting gas from the mouth of dragon, *viz.* 3 m/s. The firebrands had the dimensions of  $7.9 \times 7.9 \times 12.5$  mm (length $\times$ width $\times$ height) and a fixed mass of 0.05g consistent with the previous measurements. The frictional coefficient between the firebrand and the ground (gypsum board in the experiments) was varied  $\mu = 0.5, 0.6$  and

0.7 to investigate the sensitivity of the results to this parameter. A value for the frictional coefficient between a gypsum board and smoldering wood was not found so this range of frictional coefficients reported for the friction between wood and stone were chosen [2, 3]. The simulations were run for a physical time interval of 150 s.

### 5.3 Results and Discussion

Figure 5.2 shows the contour plots and the streamlines of the mean velocity on the planes  $y = 0$  m and  $z = 0$  m, respectively, for a wind speed of  $U_w = 10$  m/s. The latter plane corresponds to the ground and as expected, the velocities do not vanish on this plane because of the wall model. It could be seen in fig. 5.2 that on the leeward side of the dragon block, a small re-circulation region (from  $x \approx 0$  m to 1.6 m) is formed with lower velocity magnitudes on the ground. The flow separated by the dragon reattaches at  $x \approx 1.6$  m on the ground. From there, the flow on the ground seems to diverge but is hindered from diverging further downstream due to the flow re-circulations on the windward sides of the blocks. As the flow re-circulates in this regions, it is funneled towards the gap between the blocks. Streamlines emerge off the windward face of either block, but meet each other at  $y = 0$  m between  $x \approx 6.7$  m to  $x \approx 7.5$  m resulting in a cross flow in this region (crossflow region). It could be seen in fig. 5.2(a) that from  $x \approx 6.6$  m, the flow tends to move over a flow structure created by this crossflow on the surface. This prevents the mean flow to stay parallel to the ground between  $x \approx 6.7$  m to  $x \approx 7.5$  m. The crossflow region potentially acts in opposition to the flow

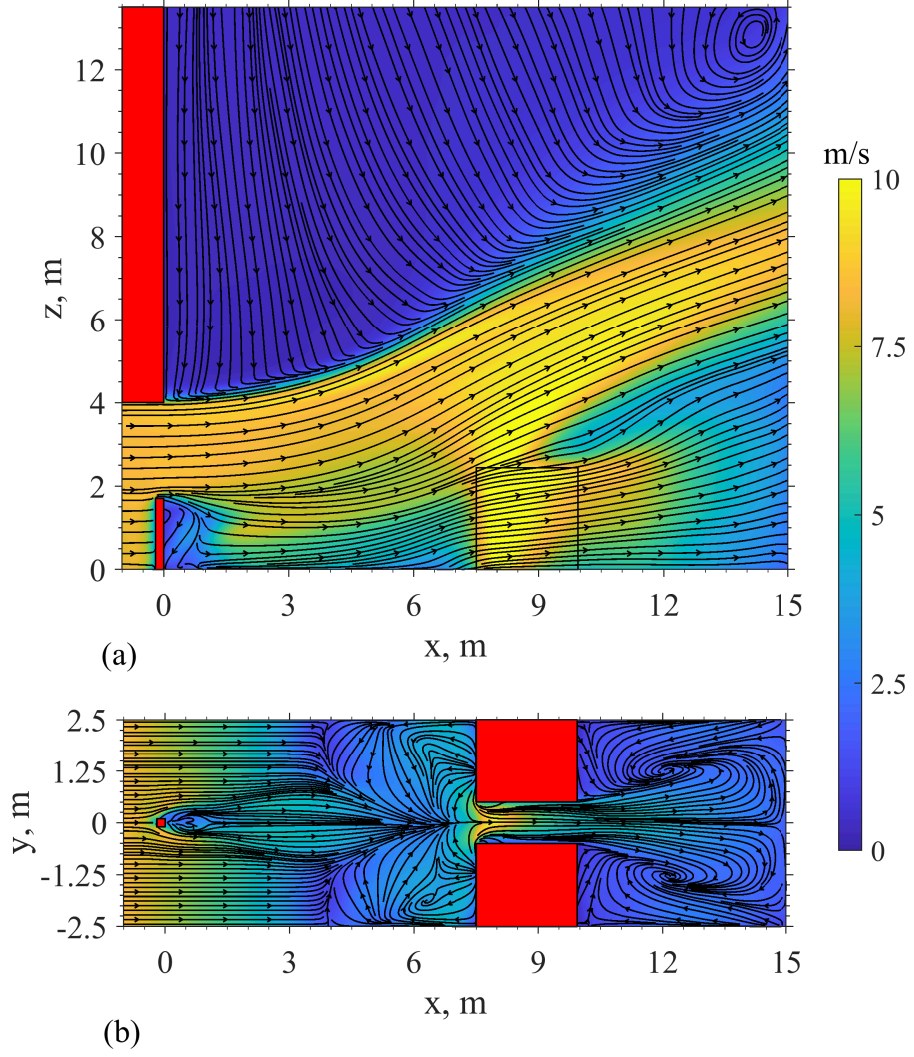


**Figure 5.2:** Mean streamline superimposed on the contour plots of mean flow velocity at (a)  $y = 0$  m; and (b)  $z = 0$  m for wind speed of 10 m/s.

moving through. As the flow advances from the crossflow region, it accelerates, as indicated by the higher mean velocity in the gap between blocks. After exiting the gap, the flow bifurcates to forms two re-circulating regions on the leeward of the blocks. The flow patterns in other considered wind speeds ( $U_w = 4, 6$  and

8 m/s) were overall similar to the ones discussed above for the wind speed of 10 m/s.

In order to determine the significance of the blocks on the flow pattern formed behind the dragon, an additional set of simulations was performed in the same computational configuration where the blocks were removed. The results revealed that the presence of the blocks did not significantly influence the recirculating region or the flow reattachment on the leeward side of the dragon. However, in the simulations without the blocks, the mean streamlines on the ground surface continued to diverge up to  $x \approx 7$  m and were roughly parallel to the lateral wall from the point to the end of the domain whereas the mean streamlines on the plane  $y = 0$  were parallel to the surface away from the dragon's wake.

Plotted in Fig. 5.3 are the flow mean velocity and the dimensionless root mean square of the velocity components  $u_x^{\text{rms}}/U_w$  and  $u_y^{\text{rms}}/U_w$  vs  $x$ . Here,  $u_x^{\text{rms}} = \sqrt{R_{xx}}$ ,  $u_y^{\text{rms}} = \sqrt{R_{yy}}$ , and  $R_{xx}$  and  $R_{yy}$  are the normal components of the Reynolds stress tensor in the  $x$  and  $y$  directions, respectively. The mean velocity drops on the leeward side of the dragon because of the wake behind the dragon and then peaks at  $x \approx 2.8$  m, as shown in fig. 5.3(a). This peak is a result of the reattached flow having been separated by the dragon located upstream. The velocity magnitude of the flow drops once more ahead of the blocks at  $x \approx 6$  m. Then, it rapidly increases because the flow accelerates at the entrance of the gap between the blocks, where the flow starts converging into the gap (fig. 5.2, b). Then, the velocity magnitude decreases as the flow decelerates in the  $x$  direction.

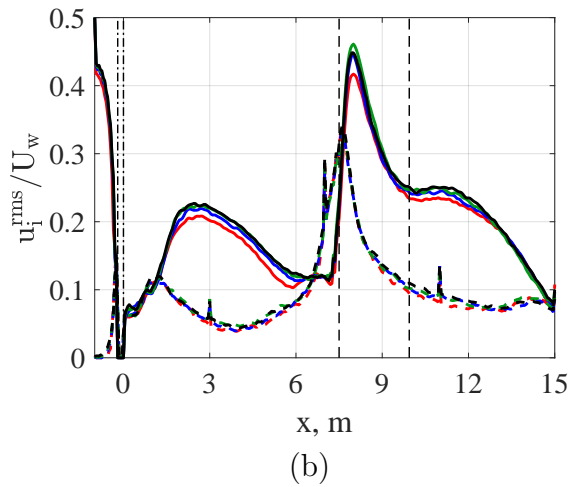
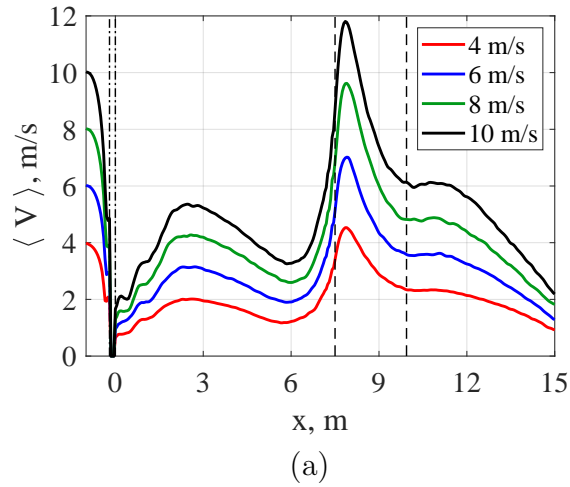


**Figure 5.3:** (a) Mean flow velocity magnitude; and (b) rms of the flow velocity components non-dimensionalized by the wind speed in the streamwise (solid lines) and spanwise (dashed lines) directions at  $z = 0$  m and  $y = 0$  m for varying wind speeds. The streamwise location of the dragon and the blocks represented by dashed and dot-dashed lines, respectively.

Fig. 5.3(b) shows that the the rms of the flow velocity in the streamwise direction (solid lines) is higher than that in the spanwise direction (dashed lines) downwind of the dragon except for  $x \approx 6.6$  to  $x \approx 7.5$  m which corresponds to the crossflow

region noted above. This shows that the spanwise component of velocity has likely more influence in the crossflow region. It is important to note that, the small peaks seen in fig. 5.2(b) at  $x = 3, 7, 11$  m for the rms of the flow velocity in the spanwise direction are an artifact of how the data are stored in FDS as a consequence of domain partitions. These discontinuities do not appear in the instantaneous flow velocities at these locations seen in figs. 5.5 and 5.6 nor do they affect the mean and variance of the firebrand trajectories, seen later in figs. 5.9, 5.10 and 5.11, thus is deemed to be acceptable.

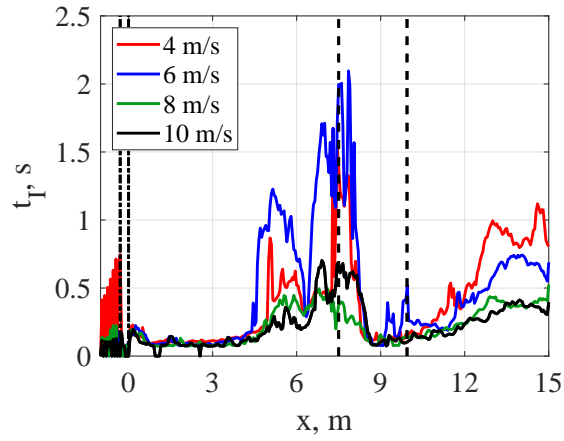
In order to determine the time scale of the flow affecting the firebrand motion is used which is defined as follows:

$$t_I(\vec{x}) = \int_0^{\infty} R_{u'_i u'_i}(\vec{x}, \tau) d\tau, \quad (5.1)$$

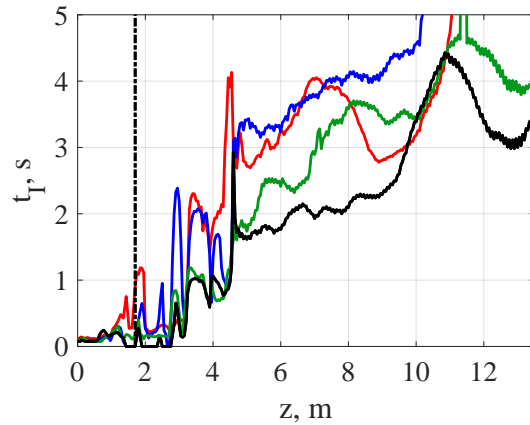
where  $R_{u'_i u'_i}(\vec{x}, \tau)$  represents the auto-correlation of the fluctuation of the velocity component  $u'_i$  and is calculated as follows:

$$R_{u'_i u'_i}(\vec{x}, \tau) = \frac{\overline{u'_i(\vec{x}, t) u'_i(\vec{x}, t + \tau)}}{\overline{u'_i(\vec{x}, t)^2}}, \quad (5.2)$$

where  $\vec{x}$  is the vector of the coordinates,  $\tau$  is the lag,  $t$  is the time, and the overbar indicates the averaging over time. Fig. 5.4 shows the integral time scale along the streamwise direction at  $z = 0$  m and  $y = 0$  m and along the vertical direction at  $x = 2$  m and  $y = 0$  m. In fig. 5.4(a), the vertical dashed line and the dot-dashed lines show the streamwise position of the blocks and the dragon, respectively. Additionally, in fig. 5.4(b) the vertical dot-dashed lines represents the height of



(a)



(b)

**Figure 5.4:** The integral time scale in the (a) streamwise direction at  $z = 0$  m and  $y = 0$  m; and (b) vertical direction at  $x = 2$  m and  $y = 0$  m for wind speed of 4, 6, 8 and 10 m/s. In sub-figure (a) the location of the dragon and the blocks represented by dashed and dot-dashed lines, respectively, whereas in sub-figure (b) the height of the dragon is given by dot-dashed line.

the dragon. The simulations revealed that the firebrands under the influence of the drag and gravitational forces, travelled from the mouth of the dragon and on an average deposited on the ground before  $x = 2$  m after which they stayed on

the ground for the rest of the simulation. Thus, looking at the fig. 5.4 it can be seen that the the max integral time scale an average firebrand encounters in transit is  $\leq 2$  s. Taking this into account in these simulations the firebrands were released at a rate of 10 firebrands per 0.01 s *i.e.*,  $1000 \text{ s}^{-1}$  from the mouth of the dragon for a total duration 20 s after the flow reached steady state.

Figure 5.5 displays top views of the firebrands sliding on the ground under a wind speed of 6 m/s at four different times. Shown in this figure are also the contours of the instantaneous flow velocity magnitude at  $z = 0$  m. As could be seen in this figure, firebrands are dispersed much more in the streamwise ( $x$ ) direction compared to the spanwise ( $y$ ) direction. The reason is for this difference is that the drag force component driving firebrands in the streamwise direction is overall greater than that in the cross-stream direction. This is because the streamwise component of the mean flow velocity at the firebrands locations is significantly greater than its spanwise component, as evident from the streamlines shown in fig. 5.2(b). Fig. 5.5 indicates that over time, as the cluster of firebrands slides toward the blocks, the cluster shrinks in the streamwise direction while firebrands converge further to the centerline  $y = 0$  m. A similar behavior was also reported in the previous experiments [75]. The impact of the vortices formed leeward of the dragon on firebrands manifests itself in a slight thickness of the firebrand cluster in the spanwise direction, as could be seen in fig. 5.5(a). However, it could be seen in the following subfigures that this thickness diminishes as the cluster slides away from the dragon vortices. Towards the end of the simulations, all the firebrands settle in a small area on the windward side of the blocks right

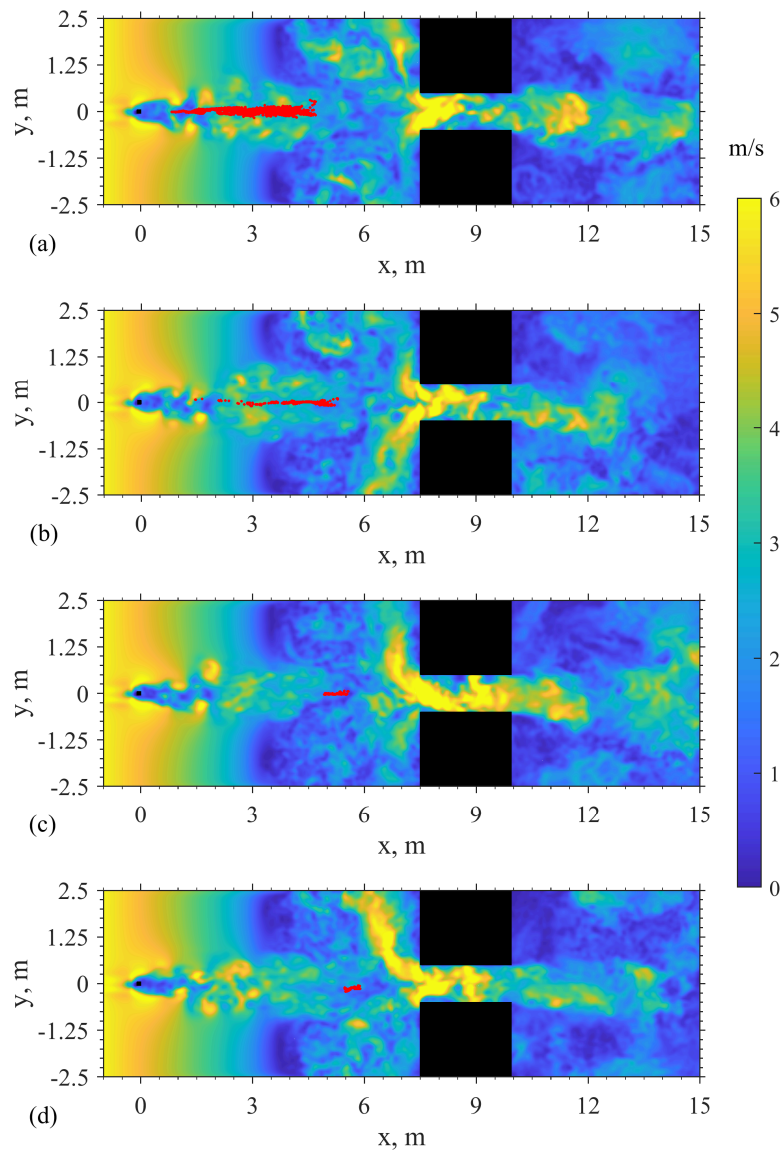


**Figure 5.5:** Scatter plot of firebrands overlaid on contour plot of instantaneous flow velocity magnitude at  $z = 0$  m, for  $U_w = 6$  m/s and  $\mu = 0.6$  at times (a) 40; (b) 70; (c) 110; and (d) 150 s.

before the crossflow region, as could be seen in fig. 5.5(d). The behavior of the firebrands in fig. 5.5 during the simulations at a wind speed of 4 m/s exhibited a

comparable pattern to that discussed above for the wind speed of 6 m/s, albeit with firebrands settling at a greater distance from the blocks in the lower wind speed.

Figure 5.6 displays the snapshots of the deposited firebrands overlaid on the contour plots of the instantaneous flow velocity magnitudes for the wind speed of 10 m/s at the same four different time instants displayed in Fig. 5.5, which is for a lower wind speed of 6 m/s. The firebrand distributions in fig. 5.6 exhibit a stark contrast to those in fig. 5.5. In all panels in fig. 5.6, almost all firebrands have passed through the gap between the blocks and largely distributed on the leeward of the blocks whereas in fig. 5.5, all firebrands are located in the windward of the blocks way ahead of the gap. At this higher wind speed, the flow is characterized by greater values of both average and variance of flow velocities, as could be seen in fig. 5.3. Hence, the overall drag force on the firebrands is sufficiently high to drive them toward and through the gap. More specifically, firebrands after deposition tend to follow the mean streamlines between the dragon and the blocks while momentarily accumulating on the windward side of the blocks similar to the previous experiments [75]. However, the firebrands do not settle in this region but rapidly move through the gap. Some firebrands exit the domain as reported in previous experiments [75], while some others end up bifurcating as a result of the re-circulating regions on the leeward side of the blocks. These firebrands later accumulate towards the leeward edge of the blocks. These simulations also reveal that a small number of firebrands are momentarily trapped in the wake of the

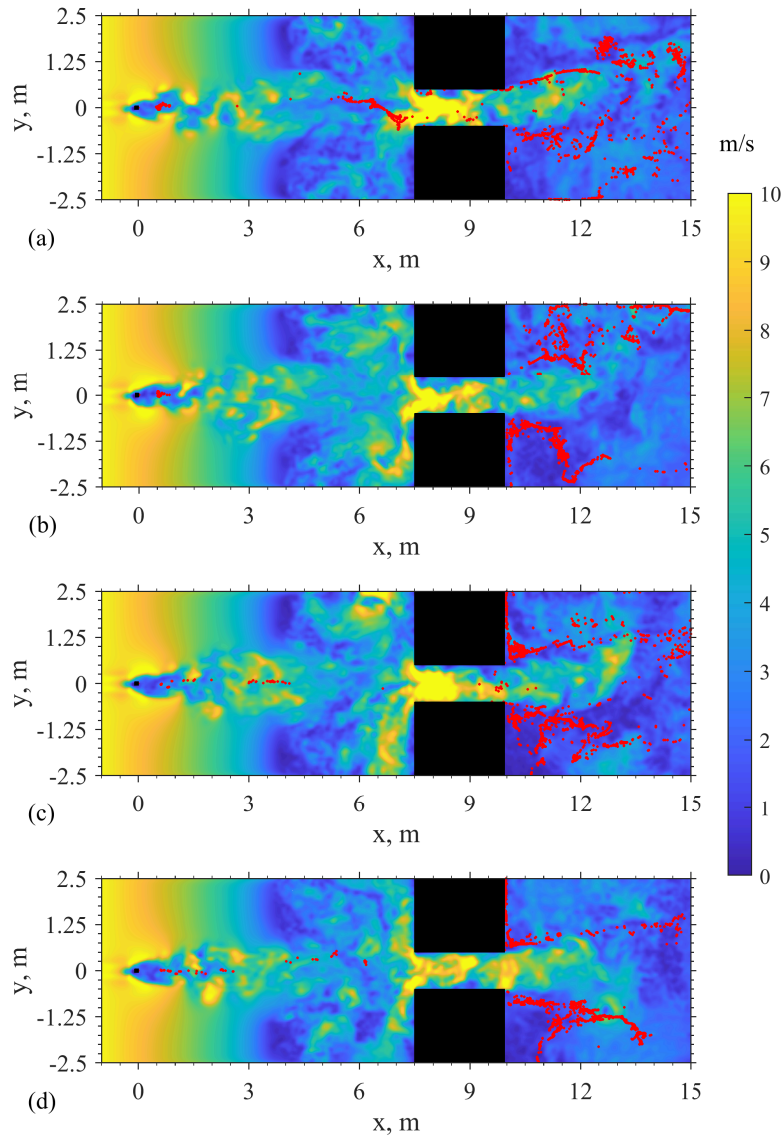


**Figure 5.6:** Scatter plot of firebrands overlaid on contour plot of instantaneous velocity magnitude at  $z = 0$  m, for  $U_w = 10$  m/s and  $\mu = 0.6$  at times (a) 40; (b) 70; (c) 110; and (d) 150 s.

dragon before sliding toward the blocks. Similar behaviours are observed for a wind speed of  $U_w = 8$  m/s.

Figure 5.7 shows the range of  $x$  coordinates of the settled firebrand clusters in the streamwise direction for two wind speeds of 4 and 6 m/s. This includes the data from the previous experiments and the current simulations for various friction coefficients. The triangles and circles indicate the mean streamwise position of the firebrand cluster for the modified and unmodified interpolation models, respectively. Such clusters are not formed at higher wind speeds, *e.g.*,

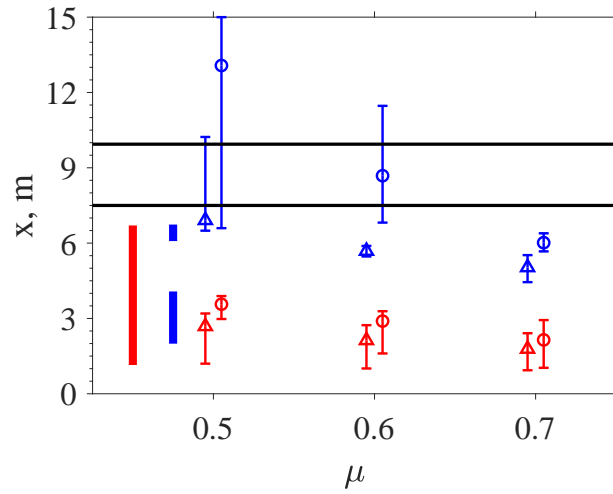


**Figure 5.7:** The mean streamwise position of the firebrand in accumulation zone at the end of the simulation using modified (triangles) and unmodified (circles) interpolation model at various frictional coefficients for  $U_w = 4$  (red) ,6 (blue) m/s. The limits of accumulations zone seen in the present work indicated by error-bar and are compared with previous experiment work [75] (thick lines on the left).

fig. 5.6. In order to evaluate the impact of the modification of the near-the-wall interpolation scheme on firebrands, the results of the simulations without this modification are also plotted in this figure for comparison. The  $x$  coordinates of the windward and leeward faces of the blocks are indicated by solid black lines. The thick red and blues lines are for the cluster in the previous experimental

work [75] at wind speeds of  $U_w = 4$  and  $U_w = 6$  m/s, respectively. In the present simulations at  $U_w = 4$  m/s, the accumulation zones of firebrands are within the accumulation zone seen in the experiments, regardless of whether the interpolation model is used or not. Whereas, for wind speed  $U_w = 6$  m/s the velocity seen by the firebrands for the sliding model without interpolation is higher, this results in the firebrands not accumulating and moving past the blocks at  $\mu = 0.5$  and  $0.6$ . Implementing the interpolation model firebrand accumulation is observed at  $\mu = 0.6$  and  $0.7$ . It is important to note that, in the experiments there were two accumulation zones observed one closer to the blocks and the other one further away. The accumulation zone seen closer to the blocks forms a considerably big pile of firebrands caused by particle-particle interaction. It is speculated that this pile would have also affect the fluid flow around itself and would result in the creations of a separate accumulation zone further upwind. In the absence of the particle-particle interaction and motion in the vertical direction the two separate accumulations zone could not be replicated in the by the current model. Taking this into consideration, the mean streamwise position of the firebrands at the end of the simulation lies in between the two accumulation zones seen in previous experiments.

Figure 5.8 shows the velocity magnitude and streamwise position averaged over all firebrands versus  $\hat{t} = t - t_r$ , where  $t_r$  indicates the release time of the firebrand from the dragon. These simulations were run with (right column) and without (left column) an interpolation model. These averaged values are shown for different wind speeds and a frictional coefficient of  $\mu = 0.5$ . The horizontal

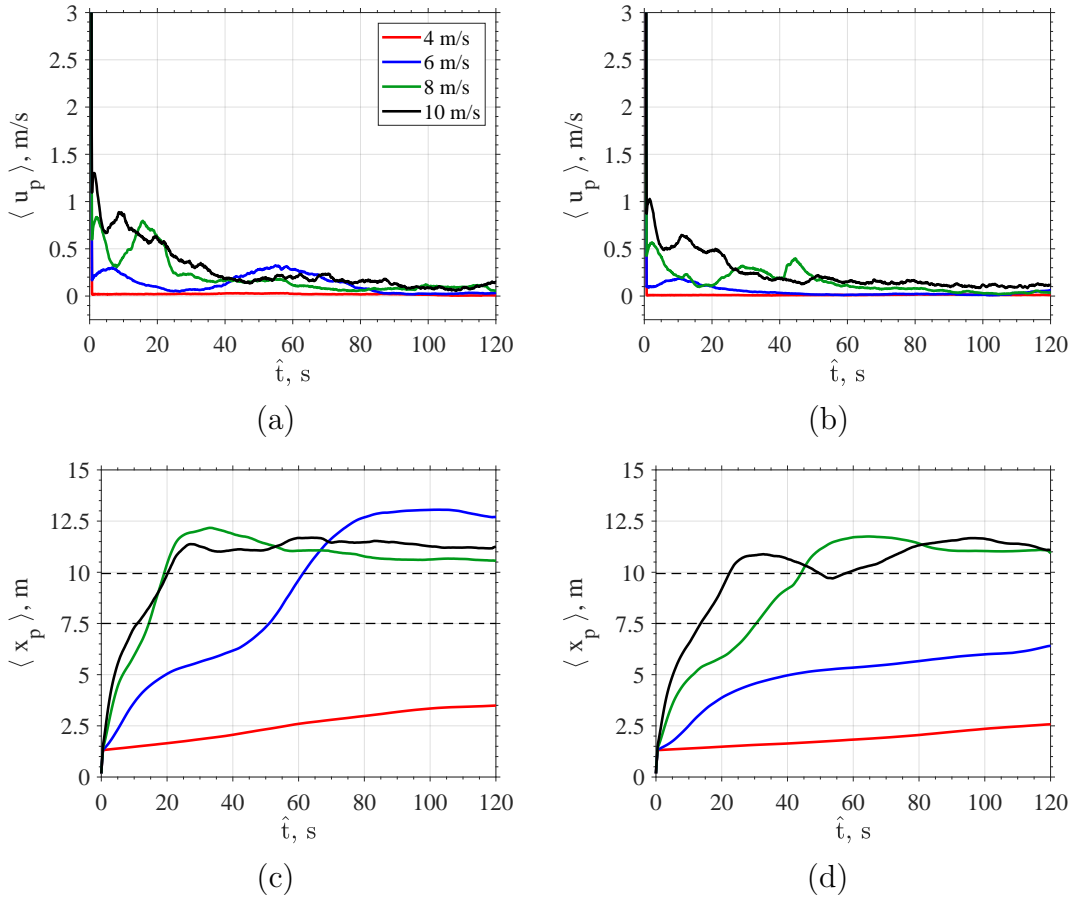


**Figure 5.8:** Mean streamwise firebrand velocity (top row) and mean streamwise firebrand position (bottom row) vs time for varying wind speeds for  $\mu = 0.5$  with streamwise position of the blocks indicated by the dashed-lines. The right and left columns shows results for unmodified and modified interpolation model. The dashed lines in panels (c,d) shows the streamwise position of the blocks.

dashed lines in figs 5.8 (c,d), show the streamwise position of the blocks. For all wind speeds, firebrands on an average deposit in the dragon's wake between  $x \approx 1.2$  m and  $x \approx 1.5$  m as could be seen in fig. 5.2. As firebrands move out of the dragon's wake at  $x \approx 1.6$  m, they experience higher flow velocity as the

flow separated by the dragon reattaches. This results in an increase in the average firebrand velocity which peaks at  $x \approx 2.7$  m corresponding to the peak in the flow velocity as could be seen in fig. 5.3(a). The occurrence of this peak happens at a later time for lower wind speeds and is not observed at  $U_w = 4$  m/s. At higher wind speeds  $U_w = 8, 10$  m/s, most of the firebrands slow down at  $x \approx 5.5$  m as they approach the blocks. This location roughly corresponds to troughs in the flow velocity magnitude displayed in fig. 5.3(a). For higher wind speeds, the drag forces are considerably higher than the frictional forces in this region which lead the firebrands to move past the crossflow region and accelerate through the gap, as indicated by the second peak in fig. 5.8(a). However, for lower wind speeds of  $U_w = 4$  m/s the firebrands tend to slow down and settle on the windward side of the blocks. The reason for this settlement is the dominance of the frictional forces over the drag forces in this regions. For higher wind speeds of  $U_w = 8, 10$  m/s, the modification in the interpolation model causes the firebrands to experience a lower fluid velocity causing the firebrands to reach the gap later and consequently accelerating later. This delays the second peak seen in the averaged velocity seen for higher wind speeds. In case of  $U_w = 6$  m/s prevent most of the firebrands from moving past the gap as evident from fig. 5.7. Also the average streamwise position of the firebrands at  $U_w = 4$  m/s is lower when the interpolation model is modified as compared to the same speed without the interpolation modification.

Figure 5.9 shows the mean of the absolute value of the spanwise firebrand position as they move downstream after being released from the dragon for a frictional coefficient of  $\mu = 0.5, 0.6$  and  $0.7$ . Since the domain is symmetric along

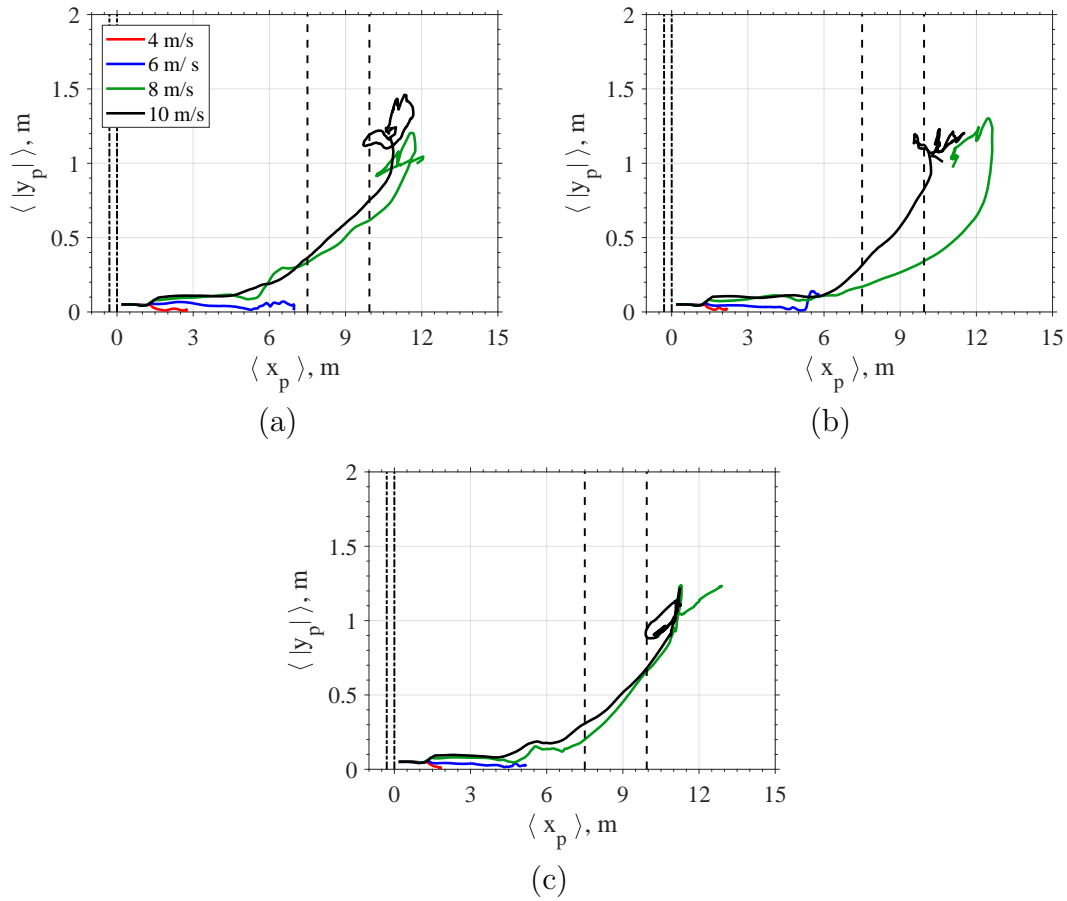


**Figure 5.9:** The mean of the absolute value of the spanwise firebrand position  $\langle |y_p| \rangle$  vs the mean streamwise firebrand position  $\langle x_p \rangle$  for a frictional coefficient of (a)  $\mu = 0.5$ ; (b)  $\mu = 0.6$ ; and (c)  $\mu = 0.7$ . The vertical dashed and dot-dashed lines indicate the streamwise location of the blocks and the dragon, respectively.

the streamwise direction the mean of the absolute value of the spanwise position  $\langle |y_p| \rangle$  can be used to evaluate the mean spanwise motion of the firebrands. At lower wind speeds ( $U_w = 4, 6$  m/s) the  $\langle |y_p| \rangle$  tends to remain constant or approach zero as the firebrands move downstream and accumulate. On the other hand, at higher wind speeds ( $U_w = 8, 10$  m/s)  $\langle |y_p| \rangle$  is marginally higher than the value

at lower wind speeds. This is a consequence of higher drag force in the spanwise direction. As these firebrands approach the crossflow region the value of  $\langle |y_p| \rangle$  increases as results of the flow in this region. Indicating the firebrand's motion in the spanwise direction as they move towards the gap. As these firebrands into and pass the gap  $\langle |y_p| \rangle$  increases considerably more, indicating firebrands moving towards the lateral walls aided by the re-circulation regions on the leeward side of either blocks. The interaction of the firebrands with the re-circulating region is indicated by the "swirls" seen in this figure towards the leeward side of the blocks. The value of  $\langle |y_p| \rangle$  does not seem to significantly affected by the change in the frictional coefficient.

Plotted in figs. 5.10 and 5.11 are the variances of the firebrand positions in the streamwise and spanwise directions, respectively, versus  $\langle x_p \rangle$ . These variances are the indicator of the dispersion of firebrands in the streamwise and spanwise directions. Comparing fig. 5.10 vs fig. 5.11 reveals that at a given wind speed, the variance of the firebrand position in the streamwise is overall greater than that in the spanwise direction. This means that firebrands are dispersed in the streamwise direction more than they are in the spanwise direction. This difference is attributed to fact that the rms of the flow velocity component in the streamwise direction is greater than that in the spanwise direction, as could be seen in fig. 5.3(b). Furthermore, in figs. 5.10 and 5.11, the comparison of the set of curves for the wind speeds of 4 and 6 m/s and that for the wind speeds of 8 and 10 m/s that the variances of the firebrand position at higher wind speeds become orders of magnitude greater than those at lower wind speeds in both directions as firebrands

move further downstream. Figs. 5.10 and 5.11 also suggest that the variance of firebrand positions in the streamwise and spanwise directions follow similar trends in all considered frictional coefficient values.

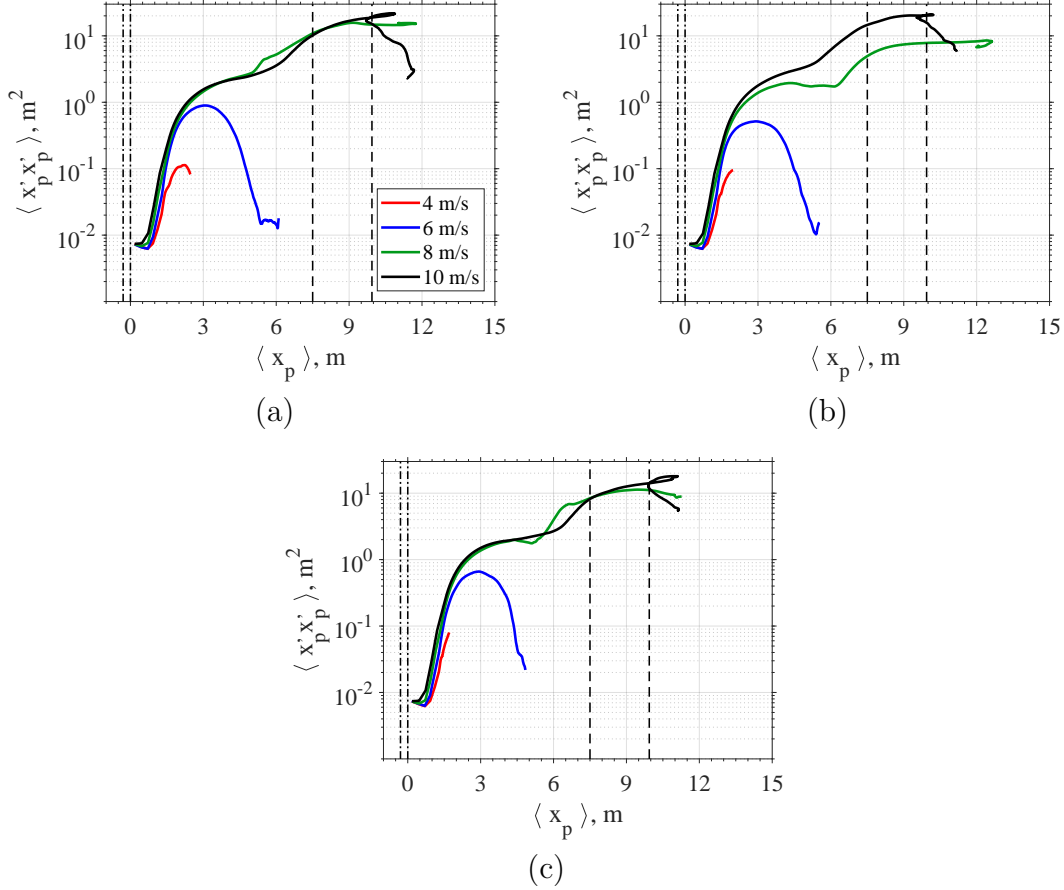


**Figure 5.10:** The variance of the firebrand position in the streamwise direction  $\langle x'_p x'_p \rangle$  vs the mean firebrand streamwise position  $\langle x_p \rangle$  for friction coefficients (a)  $\mu = 0.5$ ; (b)  $\mu = 0.6$ ; and (c)  $\mu = 0.7$ . The vertical dashed and dot-dashed lines indicate the streamwise location of the blocks and the dragon, respectively.

In figure 5.10, it can be observed that at lower wind speeds of  $U_w = 4, 6$  m/s, the value of  $\langle x'_p x'_p \rangle$  experiences a drop at  $x_p \approx 1$  m after being released

from the dragon. This phenomenon is attributed to the interaction between the background flow in the dragon's wake (seen in fig. 5.2, a) and the firebrands, which exhibit lower turbulent kinetic energy at these speeds, resulting in reduced dispersion of the firebrands. Conversely, at higher wind speeds of  $U_w = 8, 10$  m/s, the turbulent kinetic energy is higher in the same region, leading to the growth of  $\langle x'_p x'_p \rangle$  from the release point until landing indicating higher dispersion. On average, the firebrands at all wind speeds land within the dragon's wake ( $x_p \approx 1.2$  to  $1.5$  m). Here the firebrands experience flow reattachment behind the dragon which cause the higher flow velocity magnitude and increasing rms of the streamwise flow velocity, as depicted in fig. 5.3 (b). This results in the increase of  $\langle x'_p x'_p \rangle$  between  $1.2 \leq x \leq 2.8$  m. For the case with a wind speed of  $U_w = 6$  m/s, the value of  $\langle x'_p x'_p \rangle$  reaches a peak around  $x_p \approx 2.8$  m. This corresponds to the peak in rms of the streamwise flow velocity (as shown in fig. 5.3 (b) indicating the firebrands are the most dispersed at this location. Subsequently, there is a significant decrease in  $\langle x'_p x'_p \rangle$ , indicating the accumulation of firebrands in a tight area by the end of the simulation, as illustrated in fig. 5.5. At  $U_w = 4$  m/s,  $\langle x'_p x'_p \rangle$  exhibits almost monotonic growth, with firebrands coming to rest at  $x_p \approx 2.4$  m as a result of lower drag forces acting on the firebrands compared to frictional forces. For higher wind speeds of  $U_w = 8, 10$  m/s,  $\langle x'_p x'_p \rangle$  increases by two order of magnitude from firebrands landing to moving pass the gap. This growth occurs in two steps, with each step increasing it roughly by an order of magnitude. The first step is attributed to an increasing rms of the streamwise flow velocity direction from the point of landing to  $x_p \approx 2.8$  m, as seen in fig. 5.3

(b). The second step is observed around the crossflow region is a result of the flow funneling the firebrands into the gap and the higher rms of the streamwise flow velocity between the gap. Exiting the gap at these wind speeds the firebrands "swirl" as a result of the re-circulating regions (fig. 5.2 b) on the leeward side of the blocks and accumulate on the leeward edge of the block. The firebrand accumulation on the leeward edge of the block is tighter at  $U_w = 10$  m/s as seen by the lower value of  $\langle x'_p x'_p \rangle$  towards the end of the simulation when compared to  $U_w = 8$  m/s.

It could be seen in fig. 5.11 that for all wind speeds,  $\langle y'_p y'_p \rangle$  remains fairly constant from the point of release until landing on the ground. After firebrands land,  $\langle y'_p y'_p \rangle$  rapidly drops for the wind speed of 4 m/s, as the firebrands move out of the wake regions of the dragon on the ground and enter the region  $1.5 \leq x \leq 6$  m where the rms of the flow velocity in the spanwise direction is the lowest as could be seen in fig. 5.3(b). For the wind speed of 6 m/s,  $\langle y'_p y'_p \rangle$  remains relatively steady till  $x_p \approx 3$  m and then drops with some oscillations in the end as the firebrands accumulate on the windward side of the blocks. These oscillations are a result of lateral motion of firebrand cluster while interacting with the crossflow before accumulation. For higher wind speeds of  $U_w = 8$  and 10 m/s,  $\langle y'_p y'_p \rangle$  increases rapidly as the firebrands move out of the dragon's wake and encounters the reattached flow separated by the dragon. This is in contrast to  $U_w = 4, 6$  m/s as the rms of the spanwise flow velocity is higher at  $U_w = 8, 10$  m/s. At higher wind speeds  $\langle y'_p y'_p \rangle$  relatively unchanged approaching the crossflow region *i.e.*, between  $\langle x_p \rangle \approx 2$  to 5 m. Also, as the firebrands approach the crossflow region,

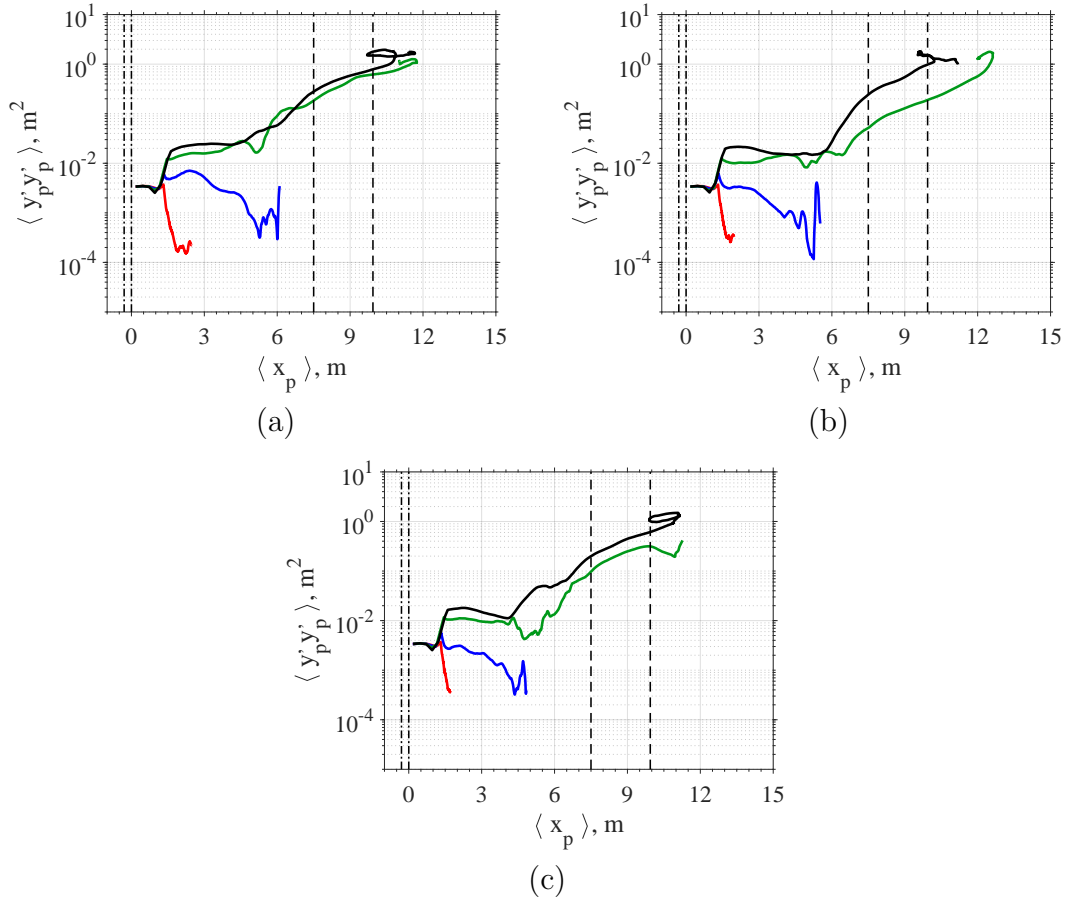


**Figure 5.11:** The variance of the firebrand position in the spanwise  $\langle y'_p y'_p \rangle$  vs the mean firebrand streamwise position  $\langle x_p \rangle$  for friction coefficients (a)  $\mu = 0.5$ ; (b)  $\mu = 0.6$ ; and (c)  $\mu = 0.7$ . The vertical dashed and dot-dashed lines indicate the streamwise location of the blocks and the dragon, respectively.

$\langle y'_p y'_p \rangle$  drops slightly indicating the firebrands getting close to together. This is a result of crossflow in funneling the firebrands into the gap indicated by the streamlines in fig. 5.6. As the firebrands moves from the crossflow region to the gap,  $\langle y'_p y'_p \rangle$  increases by couple of order of magnitudes before they accumulate on the leeward side of the blocks. This rapid growth is a result of the higher rms of

the spanwise flow velocity in the crossflow region and the firebrands bifurcating on the leewards side of the block as a consequence of the re-circulating regions present in this area.

#### 5.4 Chapter Summary

A firebrand model was developed and integrated in FDS to track cuboidal firebrands in the Lagrangian framework in both airborne and sliding on the surface. The sliding motion of firebrands was constrained to the horizontal plane and no particle-particle interaction was modelled. The velocity seen by the firebrands while sliding was modelled in two ways: the first using fluid velocity at the first grid-point off the ground, and the second interpolating fluid velocity based on firebrand and grid point heights. Interpolated velocities were lower, yielding more realistic, slower movement, and increased accumulation tendency compared to the alternative model.

A computational setup mirroring previous experiments [75] was employed to investigate firebrand motion using the developed numerical model. The simulations unveiled notable flow structures, including re-circulation zones on the dragon's, windward, and leeward sides of the blocks. The re-circulation region on the windward side of the blocks directed flow into gaps between the blocks, while the re-circulation region on the leeward side directed flow toward the leeward edge. Additionally, a crossflow region, was identified, acting in opposition to the flow entering the gap between the blocks onto the surface. These simulations indicated a higher mean velocity of the flow as it traversed this gap.

Similar to previous experiments, firebrands accumulation was observed on the windward side of the blocks at lower wind speeds using the interpolation model for higher frictional coefficients. The current model does not account for the vertical motion of firebrands and the particle-particle interaction the accumulation zone was smaller compared to the experiments. On the other hand, at higher wind speeds the firebrands momentarily accumulated/slowed down on the windward side of the blocks, accelerated through the gap and accumulated on the leeward side of the blocks after interacting with the re-circulating region there. The average deposition position of firebrands at low and high wind speeds was in the wake of the dragon. The firebrands experienced an increase in the variance of the streamwise position of the firebrands  $\langle x'_p x'_p \rangle$  as they move out of the dragon's wake at low and high wind speeds. At lower wind speeds the peak value of  $\langle x'_p x'_p \rangle$  corresponded to the peak seen rms of the streamwise flow velocity after which the firebrands accumulated on the windward side of the block. Whereas at higher wind speeds the value of  $\langle x'_p x'_p \rangle$  increases in two steps due to the peak seen rms of the streamwise flow velocity and the crossflow region. On the other hand, the variance of the spanwise position of the firebrands  $\langle y'_p y'_p \rangle$  from the moment of release is similar for lower and higher wind speeds. As the firebrands land and move out of the wake the value of  $\langle y'_p y'_p \rangle$  drops at lower wind speeds but increases roughly by couple of orders of magnitude at higher wind speeds. Overall the variance of the firebrand in the streamwise direction is greater than the spanwise direction as result of significantly higher rms flow velocity in the streamwise as compared to the spanwise direction.

## Chapter 6. Summary and Conclusions

In this study, a framework was devised to gain improved understanding of the dispersion and deposition of firebrands in the areas with structures with relevance to the spread of WUI fires by the spotting mechanism. This approach involved development of firebrand model in the FDS framework to simulate and characterize key aspects observed in the firebrand deposition on and around single and neighboring structures subject to the wind condition. Since in reality structures significantly vary from one to another in shape and hence considering all possible combinations becomes impractical, simplistic geometry of a rectangular blocks was chosen to represent structure vulnerable to spotting in the WUI community. Keeping these aspects in mind, three scenarios were simulated.

The first scenario included an isolated rectangular block. The dimensions of the block ranged from three to nine meters which are within the range of overall dimensions of realistic small WUI structures. The firebrands' cylindrical shape and dimensions considered here were guided by the measurements of Manzello *et al.* [38], The simulations here revealed multiple places where the no firebrands were deposited, viz., the leeward side of the block (*i.e.*, safe zone), the leeward face of the block and a roughly triangular region on the lateral faces of the block. It was determined that the safe zone was a result of the block shielding this area

from firebrands, resulting in a roughly rectangular shape with a width equal to that of the block and a length proportional to the block's height. For blocks with longer lengths, a higher concentration of firebrands was deposited towards the trailing edge after gaining momentum from higher flow velocity around the leading edge. The temperature of the firebrands was found to be higher for those deposited higher on the block.

In the second scenario, cylindrical firebrands that were identical to those in the previous scenario were released onto three cubic blocks arranged in tandem and parallel. This scenario is relevant to multiple adjacent structures in a WUI community. A parametric study was conducted by varying the separation distance between the blocks and the wind speeds. The simulations here revealed the existence of the safe zone on the leewards side of all the blocks for all cases. Upon closer examination of the deposited firebrands around the safe zone, it was observed that the shape of the safe zone was more trapezoidal rather than rectangular. The shorter base of the trapezoid exhibited a roughness as a result of the turbulent dispersion. The length of the safe zone was found to be directly proportional to the wind speed. At interface of the safe zone and the deposited firebrands, the temperature of the firebrands is relatively higher. Interestingly, the positioning of the blocks in either a tandem or parallel arrangement did not significantly affect the dimensions of the safe zones. However, in cases with higher wind speeds and smaller separation distances, the safe zone encroached onto the windward face of the trailing block when the blocks were arranged in a tandem arrangement. Additionally, the close proximity of the blocks in a parallel arrange-

ment increased the roughness observed at the interface between the safe zone and the deposited firebrands.

The third scenario simulated the firebrand dispersion and deposition previously investigated experimentally by Suzuki and Manzello [75]. In these experiments the firebrands were released from a firebrand generating apparatus onto two adjacent block in a wind tunnel. A model was developed and integrated in FDS to track cuboidal firebrands similar to the ones studied in the experiments of Suzuki and Manzello [75]. Here, the sliding motion of firebrands after landing on the ground was also modeled in contrast to the model in the first and second scenarios where this effect was neglected and firebrands were assumed to stay where they landed. The simulations here revealed accumulation zone at lower wind speeds similar to that in the previous experiments [75]. On the other hand, at higher wind speeds, the simulations showed although firebrands slowed down in front of the blocks, they eventually moved through the gap and accumulated on the leeward side of the blocks. More specifically, some firebrand were temporarily trapped in the wake of the dragon. These simulations also brought some insight to the firebrand motion on the surface in other scenarios similar to the one considered here.

The current work has made significant progress in understanding the dispersion, deposition, and accumulation of firebrands on and around individual and multiple blocks that emulate neighboring structures in the WUI. Nevertheless, there are still unexplored avenues for future research in this field. In subsequent research, particularly in the first two scenarios, One might also consider flows

not orthogonal to the structures, various structure shapes, etc.; and more detailed shapes for structures along with different arrangement of structures. This could also encompass the examination of heat flux transferred from the deposited firebrands because of its consequence on ignition of the recipient fuel. However, calculations of this flux require additional models to represent this phenomenon. Future work could also involve, improving the firebrand model by accounting for other forces which could significantly affect the firebrands trajectories, e.g. lift force due to the rotation of cylinder along the major axis, Virtual mass, Basset history forces, etc.

A direct application of this research could be implementing the firebrand tracking models, developed in this work, into a mesoscale numerical weather prediction system such as the WRF-Fire Model. This model is capable of modelling the spread of wildland fires in different terrains while accounting for a two-way coupling between the fire and the atmosphere around it. More recently, WRF-Fire has expanded its capabilities to account for spotting by predicting the transport and landing of burning spherical firebrands. Adding a non-spherical firebrand tracking model such as, the one developed in this work, into WRF-Fire could greatly improve its ability to predict the spread of Wildland and WUI fires. This can in turn be used can also be used to guide preventative actions needed to be taken in a WUI area or before a prescribed burn depending on the predicted weather in the said area.

## References

- [1] Iftekhhar Ahmed and Kylie Ledger. Lessons from the 2019/2020 ‘black summer bushfires’ in australia. *International journal of disaster risk reduction*, 96:103947, 2023.
- [2] JR Aira, F Arriaga, G Íñiguez-González, and J Crespo. Static and kinetic friction coefficients of scots pine (*pinus sylvestris* l.), parallel and perpendicular to grain direction. *Materiales de Construcción*, 64(315):e030–e030, 2014.
- [3] Husam Al Qablan, Shaher Rababeh, Hasan Katkhuda, and Tamara Al-Qablan. On the use of wooden beams as an anti-seismic device in stone masonry in qasr el-bint, petra, jordan. *Journal of Building Engineering*, 21:82–96, 2019.
- [4] Chandana Anand. *Computational investigations of ignition characteristics of live fuels and deposition of firebrands in a turbulent boundary layer*. PhD thesis, The University of Alabama in Huntsville, 2018.
- [5] Chandana Anand, Babak Shotorban, and Shankar Mahalingam. Dispersion and deposition of firebrands in a turbulent boundary layer. *International Journal of Multiphase Flow*, 109:98–113, 2018.
- [6] Marco Atzori, Sergio Chibbaro, Christophe Duwig, and Luca Brandt. LES and RANS calculations of particle dispersion behind a wall-mounted cubic obstacle. *International Journal of Multiphase Flow*, 151:104037, 2022.
- [7] Gholamhossein Bagheri and Costanza Bonadonna. On the drag of freely falling non spherical particles. *Powder Technology*, 301:526–544, 2016.
- [8] Nicolas Bouvet and Minhyeng Kim. Firebrands generated during wui fires: A novel framework for 3d morphology characterization. *Fire Technology*, pages 1–40, 2024.
- [9] Nicolas Bouvet, Savannah S Wessies, Eric D Link, and Stephen A Fink. A framework to characterize wui firebrand shower exposure using an integrated

- approach combining 3d particle tracking and machine learning. *International Journal of Multiphase Flow*, 170:104651, 2024.
- [10] I Celik, M Klein, and J Janicka. Assessment measures for engineering LES applications. *Journal of fluids engineering*, 131(3), 2009.
- [11] IB Celik, ZN Cehreli, and I Yavuz. Index of resolution quality for large eddy simulations. *Journal of Fluids Engineering*, 127(5):949–958, 2005.
- [12] Ishmail B Celik, Urmila Ghia, Patrick J Roache, and Christopher J Freitas. Procedure for estimation and reporting of uncertainty due to discretization in cfd applications. *Journal of fluids Engineering-Transactions of the ASME*, 130(7), 2008.
- [13] National Interagency Fire Center. National interagency fire center fire statistics. 2023. , URL: <https://www.nifc.gov/fire-information/statistics>.
- [14] National Interagency Fire Center. National interagency fire center fire statistics. 2023. , URL: <https://www.nifc.gov/fire-information/statistics>.
- [15] James W Deardorff. Stratocumulus-capped mixed layers derived from a three-dimensional model. *Boundary-Layer Meteorology*, 18(4):495–527, 1980.
- [16] M Farhadi and K Sedighi. Flow over two tandem wall-mounted cubes using large eddy simulation. *Proceedings of the Institution of Mechanical Engineers, Part C: Journal of Mechanical Engineering Science*, 222(8):1465–1475, 2008.
- [17] A Carlos Fernandez-Pello. Wildland fire spot ignition by sparks and firebrands. *Fire Safety Journal*, 91:2–10, 2017.
- [18] Maria Frediani, Timothy W Juliano, Amy DeCastro, Branko Kosovic, and Jason Knievel. A fire-spotting parameterization coupled with the wrf-fire model. *Authorea Preprints*, 2022.
- [19] Maria Frediani, Kasra Shamsaei, Timothy W Juliano, Branko Kosovic, Jason Knievel, Sarah A Tessendorf, and Hamed Ebrahimian. Modeling firebrand spotting in wrf-fire for coupled fire-weather prediction. *Authorea Preprints*, 2024.

- [20] Massimo Germano, Ugo Piomelli, Parviz Moin, and William H Cabot. A dynamic subgrid-scale eddy viscosity model. *Physics of Fluids A: Fluid Dynamics*, 3(7):1760–1765, 1991.
- [21] Anatoliĭ Mikhaĭlovich Grishin. *Mathematical modeling of forest fires and new methods of fighting them*. Publishing house of the Tomsk state university, 1997.
- [22] Andreas Hölzer and Martin Sommerfeld. New simple correlation formula for the drag coefficient of non-spherical particles. *Powder Technology*, 184(3):361–365, 2008.
- [23] Katie Hoover and Laura A Hanson. *Wildfires statistics*, 2023.
- [24] Gustaaf B Jacobs and HS Udaykumar. Uncertainty quantification in Eulerian–Lagrangian simulations of (point-) particle-laden flows with data-driven and empirical forcing models. *International Journal of Multiphase Flow*, 121:103114, 2019.
- [25] Nicolas Jarrin. *Synthetic inflow boundary conditions for the numerical simulation of turbulence*. PhD thesis, university of Manchester, 2008.
- [26] Perry L Johnson, Maxime Bassenne, and Parviz Moin. Turbophoresis of small inertial particles: theoretical considerations and application to wall-modelled large-eddy simulations. *Journal of Fluid Mechanics*, 883, 2020.
- [27] Mohsen Karimi, G Akdogan, KH Dellimore, and SM Bradshaw. Quantification of numerical uncertainty in computational fluid dynamics modelling of hydrocyclones. *Computers & chemical engineering*, 43:45–54, 2012.
- [28] GI Kelbaliyev. Drag coefficients of variously shaped solid particles, drops, and bubbles. *Theoretical Foundations of Chemical Engineering*, 45(3):248–266, 2011.
- [29] Eunmo Koo, Patrick J Pagni, David R Weise, and John P Woycheese. Firebrands and spotting ignition in large-scale fires. *International Journal of Wildland Fire*, 19(7):818–843, 2010.

- [30] JGM Kuerten. Point-particle DNS and LES of particle-laden turbulent flow—a state-of-the-art review. *Flow, turbulence and combustion*, 97(3):689–713, 2016.
- [31] A Liakopoulos. Explicit representations of the complete velocity profile in a turbulent boundary layer. *AIAA journal*, 22(6):844–846, 1984.
- [32] Hee Chang Lim, Ian P Castro, and Roger P Hoxey. Bluff bodies in deep turbulent boundary layers: Reynolds-number issues. *Journal of Fluid Mechanics*, 571:97–118, 2007.
- [33] Hee Chang Lim and Masaaki Ohba. Interference effects of three consecutive wall-mounted cubes placed in deep turbulent boundary layer. *Journal of fluid mechanics*, 756:165, 2014.
- [34] Hee Chang Lim, TG Thomas, and Ian P Castro. Flow around a cube in a turbulent boundary layer: LES and experiment. *Journal of Wind Engineering and Industrial Aerodynamics*, 97(2):96–109, 2009.
- [35] Zheyuan Liu, Bingbing Chen, Chen Lang, Lunxiang Zhang, Lei Yang, and Xianwei Guo. An improved model for predicting the critical velocity in the removal of hydrate particles from solid surfaces. *Chemical Physics Letters*, 779:138832, 2021.
- [36] Salvatore Lovecchio, Francesco Zonta, Cristian Marchioli, and Alfredo Soldati. Thermal stratification hinders gyrotactic micro-organism rising in free-surface turbulence. *Physics of Fluids*, 29(5):053302, 2017.
- [37] Hussam Mahmoud and Akshat Chulahwat. Unraveling the complexity of wildland urban interface fires. *Scientific Reports*, 8(1):1–12, 2018.
- [38] Samuel L Manzello, Alexander Maranghides, and William E Mell. Firebrand generation from burning vegetation. *International Journal of Wildland Fire*, 16(4):458–462, 2007.
- [39] Samuel L Manzello, John R Shields, Thomas G Cleary, Alexander Maranghides, William E Mell, Jiann C Yang, Yoshihiko Hayashi, Daisaku Nii, and Tsuyoshi Kurita. On the development and characterization of a firebrand generator. *Fire Safety Journal*, 43(4):258–268, 2008.

- [40] Samuel L Manzello and Sayaka Suzuki. Exposing decking assemblies to continuous wind-driven firebrand showers. *Fire Safety Science*, 11:1339–1352, 2014.
- [41] EK Marchildon, A Clamen, and WH Gauvin. Drag and oscillatory motion of freely falling cylindrical particles. *The Canadian Journal of Chemical Engineering*, 42(4):178–182, 1964.
- [42] Robert J Martinuzzi and Brian Havel. Turbulent flow around two interfering surface-mounted cubic obstacles in tandem arrangement. *J. Fluids Eng.*, 122(1):24–31, 2000.
- [43] MathWorks. Multivariate kernel smoothing density. 2019a. , URL: [https://www.mathworks.com/help/stats/mvksdensity.html#mw\\_fa4a9f09-c01e-4651-96a1-0bb5ee54637b](https://www.mathworks.com/help/stats/mvksdensity.html#mw_fa4a9f09-c01e-4651-96a1-0bb5ee54637b).
- [44] Cristin E McArdle. Asthma-associated emergency department visits during the canadian wildfire smoke episodes—united states, april–august 2023. *MMWR. Morbidity and Mortality Weekly Report*, 72, 2023.
- [45] Kevin McGrattan, Simo Hostikka, Jason Floyd, Randall McDermott, and Marcos Vanella. Fire Dynamics Simulator technical reference guide Volume 1: Mathematical model. NIST Special Publication - Sixth Edition 1018-1, U.S. Department of Commerce, National Institute of Standards and Technology, 2018a.
- [46] Kevin McGrattan, Simo Hostikka, Randall McDermott, Jason Floyd, and Marcos Vanella. Fire Dynamics Simulator user’s guide. NIST Special Publication - Sixth Edition 1019, U.S. Department of Commerce, National Institute of Standards and Technology, 2018b.
- [47] William Mell, Alexander Maranghides, Randall McDermott, and Samuel L Manzello. Numerical simulation and experiments of burning douglas fir trees. *Combustion and Flame*, 156(10):2023–2041, 2009.
- [48] Barbara Milici, Mauro De Marchis, and Enrico Napoli. Large eddy simulation of inertial particles dispersion in a turbulent gas-particle channel flow bounded by rough walls. *Acta Mechanica*, 231(9):3925–3946, 2020.

- [49] Parviz Moin, Kyle Squires, W Cabot, and Sangsan Lee. A dynamic subgrid-scale model for compressible turbulence and scalar transport. *Physics of Fluids A: Fluid Dynamics*, 3(11):2746–2757, 1991.
- [50] E Abbaszadeh Molaei, AB Yu, and ZY Zhou. Particle scale modelling of mixing of ellipsoids and spheres in gas-fluidized beds by a modified drag correlation. *Powder technology*, 343:619–628, 2019.
- [51] D Morvan and JL Dupuy. Modeling the propagation of a wildfire through a mediterranean shrub using a multiphase formulation. *Combustion and flame*, 138(3):199–210, 2004.
- [52] S Murakami, A Mochida, Y Hayashi, and S Sakamoto. Numerical study on velocity-pressure field and wind forces for bluff bodies by  $\kappa$ - $\epsilon$ , ASM and LES. *Journal of Wind Engineering and Industrial Aerodynamics*, 44(1-3):2841–2852, 1992.
- [53] Dac Nguyen and Nigel B Kaye. Quantification of ember accumulation on the rooftops of isolated buildings in an ember storm. *Fire Safety Journal*, 128:103525, 2022.
- [54] Dac Nguyen and Nigel B Kaye. The role of surrounding buildings on the accumulation of embers on rooftops during an ember storm. *Fire Safety Journal*, page 103624, 2022.
- [55] Franck Nicoud and Frédéric Ducros. Subgrid-scale stress modelling based on the square of the velocity gradient tensor. *Flow, turbulence and Combustion*, 62(3):183–200, 1999.
- [56] Valifornia Department of Forestry and Fire Protection. Benefits of fires. 2023. , URL: <https://www.cifffc.ca/>.
- [57] Luis A Oliveira, António G Lopes, Bantwal R Baliga, Miguel Almeida, and Domingos X Viegas. Numerical prediction of size, mass, temperature and trajectory of cylindrical wind-driven firebrands. *International journal of wild-land fire*, 23(5):698–708, 2014.
- [58] Pedram Pakseresht and Sourabh V Apte. Volumetric displacement effects in Euler–Lagrange LES of particle-laden jet flows. *International Journal of Multiphase Flow*, 113:16–32, 2019.

- [59] B Porterie, JL Consalvi, Ahmed Kaiss, and JC Loraud. Predicting wildland fire behavior and emissions using a fine-scale physical model. *Numerical Heat Transfer, Part A: Applications*, 47(6):571–591, 2005.
- [60] Md M Rahman, Ming Zhao, Mohammad S Islam, Kejun Dong, and Suvash C Saha. Numerical study of nanoscale and microscale particle transport in realistic lung models with and without stenosis. *International Journal of Multiphase Flow*, 145:103842, 2021.
- [61] Lord Rayleigh. LIII. on the resistance of fluids. *The London, Edinburgh, and Dublin Philosophical Magazine and Journal of Science*, 2(13):430–441, 1876.
- [62] PJ Richards, RP Hoxey, BD Connell, and DP Lander. Wind-tunnel modelling of the silsoe cube. *Journal of Wind Engineering and Industrial Aerodynamics*, 95(9-11):1384–1399, 2007.
- [63] PJ Richards, RP Hoxey, and LJ Short. Wind pressures on a 6 m cube. *Journal of Wind Engineering and Industrial Aerodynamics*, 89(14-15):1553–1564, 2001.
- [64] Anne A. Riddle. Wildfires statistics, 2023.
- [65] Wolfgang Rodi. Large-eddy simulations of the flow past bluff bodies: state-of-the art. *JSME International Journal Series B Fluids and Thermal Engineering*, 41(2):361–374, 1998.
- [66] Lasse Rosendahl. Using a multi-parameter particle shape description to predict the motion of non-spherical particle shapes in swirling flow. *Applied Mathematical Modelling*, 24(1):11–25, 2000.
- [67] N Sardoy, JL Consalvi, A Kaiss, AC Fernandez-Pello, and B Porterie. Numerical study of ground-level distribution of firebrands generated by line fires. *Combustion and Flame*, 154(3):478–488, 2008.
- [68] Nicolas Sardoy, Jean-Louis Consalvi, Bernard Porterie, and A Carlos Fernandez-Pello. Modeling transport and combustion of firebrands from burning trees. *Combustion and Flame*, 150(3):151–169, 2007.

- [69] British Columbia Wildfire Service. 2023. , URL: <https://www2.gov.bc.ca/gov/content/safety/wildfire-status/wildfire-response/what-causes-wildfire>.
- [70] Takaaki Shizawa, Shinji Honami, and Masahiko Yamamoto. Experimental study of horseshoe vortex at wing/body junction with attack angle by triple hot-wire. page 323, 1996.
- [71] CC Simpson, JJ Sharples, and JP Evans. Resolving vorticity-driven lateral fire spread using the wrf-fire coupled atmosphere–fire numerical model. *Natural Hazards and Earth System Sciences*, 14(9):2359–2371, 2014.
- [72] Joseph Smagorinsky. General circulation experiments with the primitive equations: I. the basic experiment. *Monthly weather review*, 91(3):99–164, 1963.
- [73] Frits Byron Soepyan, Selen Cremaschi, Brenton S McLaury, Cem Sarica, Hariprasad J Subramani, Gene E Kouba, and Haijing Gao. Threshold velocity to initiate particle motion in horizontal and near-horizontal conduits. *Powder Technology*, 292:272–289, 2016.
- [74] Jiayun Song, Xinyan Huang, Naian Liu, Han Li, and Linhe Zhang. The wind effect on the transport and burning of firebrands. *Fire technology*, 53:1555–1568, 2017.
- [75] S Suzuki and SL Manzello. Investigating the effect of structure to structure separation distance on firebrand accumulation. front. *Frontiers in Mechanical Engineering*, 6:628510, 2021.
- [76] C S Tarifa, P P del Notario, F G Moreno, and A R Villa. Transport and combustion of firebrands. Final report of grants fg-sp 114 and fg-sp 146, Instituto Nacional de Tecnica Aeroespacial, “Esteban Terradas”, 1967.
- [77] Bernard Teague, Susan Pascoe, and Ronald McLeod. The 2009 victorian bushfires royal commission final report: summary. 2010.
- [78] Ali Tohidi and Nigel B Kaye. Stochastic modeling of firebrand shower scenarios. *Fire Safety Journal*, 91:91–102, 2017.

- [79] Ali Tohidi and Nigel Berkeley Kaye. Comprehensive wind tunnel experiments of lofting and downwind transport of non-combusting rod-like model firebrands during firebrand shower scenarios. *Fire safety journal*, 90:95–111, 2017.
- [80] Andrea Trucchia, Vera Egorova, Anton Butenko, Inderpreet Kaur, and Gianni Pagnini. Randomfront 2.3: a physical parameterisation of fire spotting for operational fire spread models—implementation in wrf-sfire and response analysis with lsfire+. *Geoscientific Model Development*, 12(1):69–87, 2019.
- [81] William T Vetterling and William H Press. *Numerical recipes: example book C*. Cambridge University Press, 1992.
- [82] AW Vreman. An eddy-viscosity subgrid-scale model for turbulent shear flow: Algebraic theory and applications. *Physics of fluids*, 16(10):3670–3681, 2004.
- [83] Rahul Wadhvani, Catherine Sullivan, Amila Wickramasinghe, Matthew Kyng, Nazmul Khan, and Khalid Moinuddin. A review of firebrand studies on generation and transport. *Fire safety journal*, page 103674, 2022.
- [84] H Werner and H Wengle. Large-eddy simulation of turbulent flow over and around a cube in a plate channel. In *Turbulent shear flows 8*, pages 155–168. Springer, 1993.
- [85] A Yakhot, Steven A Orszag, V Yakhot, and M Israeli. Renormalization group formulation of large-eddy simulations. *Journal of Scientific Computing*, 4(2):139–158, 1989.
- [86] Chungeng Yin, Lasse Rosendahl, Søren Knudsen Kær, and Henrik Sørensen. Modelling the motion of cylindrical particles in a nonuniform flow. *Chemical Engineering Science*, 58(15):3489–3498, 2003.